AD NUMBER

AD360873

NEW LIMITATION CHANGE

TO

Approved for public release, distribution unlimited

FROM

Distribution authorized to U.S. Gov't. agencies only; Administrative/Operational Use; 25 JUL 1960. Other requests shall be referred to Director, Defense Atomic Support Agency, Washington, DC 20301.

AUTHORITY

DNA ltr dtd 7 Nov 1980

AD NUMBER

AD360873

CLASSIFICATION CHANGES

TO

unclassified

FROM

confidential

AUTHORITY

DNA ltr dtd 7 Nov 1980

AD 360873 L

CONFIDENTIAL

WT-1430

This document consists of 88 pages.

No. 147 of 175 copies, Series A

OPERATION

PLUMBBOB

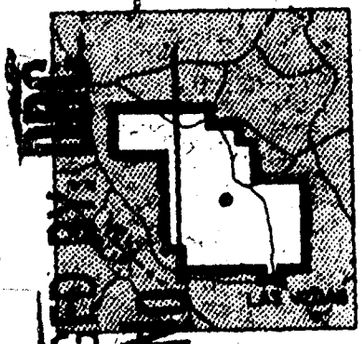

NEVADA TEST SITE

MAY-OCTOBER 1957

Project 5.1

IN-FLIGHT STRUCTURAL RESPONSE of an HSS-1 HELICOPTER to a NUCLEAR DETONATION (U)

Issuance Date: July 25, 1960

HEADQUARTERS FIELD COMMAND
DEFENSE ATOMIC SUPPORT AGENCY
SANDIA BASE, ALBUQUERQUE, NEW MEXICO

CONFIDENTIAL

Inquiries relative to this report may be made to

Chief, Defense Atomic Support Agency
Washington 25, D. C.

When no longer required, this document may be destroyed in accordance with applicable security regulations.

DO NOT RETURN THIS DOCUMENT

AEC Technical Information Service Extension
Oak Ridge, Tennessee

WT-1430

OPERATION PLUMBBOB—PROJECT 5.1

IN-FLIGHT STRUCTURAL RESPONSE of an HSS-1 HELICOPTER to a NUCLEAR DETONATION (U)

J. H. Walls
Bureau of Aeronautics
Department of the Navy
Washington 25, D. C.

N. C. Heslin
Sikorsky Aircraft Division
United Aircraft Corporation
Stratford, Connecticut

FOREWORD

This report presents the final results of one of the 46 projects comprising the Military Effects Program of Operation Plumbbob, which included 24 test detonations at the Nevada Test Site in 1957.

For overall Plumbbob military-effects information, the reader is referred to the "Summary Report of the Director, DOD Test Group (Programs 1–9)," ITR–1445, which includes: (1) a description of each detonation, including yield, zero-point location and environment, type of device, ambient atmospheric conditions, etc.; (2) a discussion of project results; (3) a summary of the objectives and results of each project; and (4) a listing of project reports for the Military Effects Program.

ABSTRACT

An instrumented HSS-1 helicopter was flown in the vicinity of nuclear detonations to measure helicopter response to overpressure and gust and to determine the delivery capabilities of the HSS-1 for antisubmarine warfare as limited by blast effects. Measurements of overpressure and resulting stresses were obtained with the helicopter doors and windows opened and with and without tail-cone reinforcements. Partial coverage of the range of shock front incident angles expected from the detonation of underwater nuclear devices was obtained.

Comparisons are shown of experimental gust response data obtained during these HSS-1 tests with prediction of helicopter gust response made possible by employing a six-degrees-of-freedom analysis of helicopter stability and control characteristics and maneuvering loads. Favorable correlation provides confidence that the analytical methods may be employed to predict the helicopter flying qualities as well as applied aerodynamic loads throughout the range of actual delivery conditions.

Comparison of experimental fuselage stresses with analytical predictions are presented to show the accuracy of the stress analysis methods employed for determination of fuselage response to overpressure. Confirmation of analysis methods for structure most critical for overpressure effects permits establishment of the HSS-1 structural limitations due to blast. These limitations were determined by analysis to be the helicopter design limit maneuvering load factor of 2.67 g and a limit overpressure of 0.71 psi.

The primary objective of the project was achieved to the extent that the critical blast limits of the HSS-1 helicopter were adequately defined for application to the problem of safe escape from underwater nuclear bursts.

PREFACE

Grateful acknowledgment is given for contribution to the project success provided by LCDR A. R. Henson, Project Officer during the field test phase, and by other members of the Naval Air Special Weapons Facility who ably conducted the operational phases of the project. The combined efforts of Naval Air Special Weapons Facility and Sikorsky Aircraft personnel facilitated the preparation of this report.

CONTENTS

FIGURES

TABLES

Chapter 1
INTRODUCTION

1.1 OBJECTIVES

The major effects on aircraft flying in the vicinity of a nuclear detonation are shock overpressure, gust loading, and thermal radiation. These effects are of primary significance in the design of aircraft and in the establishment of techniques and procedures to be utilized in the delivery of atomic weapons.

The primary objective of this project was to measure the overpressure and gust response of the HSS-1 helicopter (Figure 1.1) and to determine the delivery capabilities of the HSS-1 helicopter for antisubmarine warfare (ASW) weapons as limited by blast effects.

The secondary objectives of this project were to obtain experimental data for the Departments of the Army and Navy related to helicopter response to nuclear blast for correlation with analytical techniques and for extension to the general problem of helicopter response to nuclear effects. The interest in general data of this type varied from considerations of helicopter safe delivery and standoff criteria for Navy use to lethal damage criteria applicable to helicopter employment by the Department of the Army.

1.2 BACKGROUND

The HSS-1 helicopter was the first instrumented helicopter participating in a nuclear test series specifically to obtain experimental results. It was one of five aircraft which participated in Program 5, which was concerned with effects from kiloton-yield-class nuclear devices. Since no instrumented helicopter had previously participated in a nuclear test, neither experimental nor actual effects-response data were available for substantiation of predicted response. Participation of the HSS-1 helicopter in Operation Plumbbob provided the necessary experimental data for this correlation.

The HSS-1 is expected to have the capability for delivering an antisubmarine warfare (ASW) special weapon. Therefore, there was urgent need for information relating to the helicopter delivery problems. Emphasis was given during Operation Plumbbob to response measurements of the main- and tail-rotor systems to gust effects and the fuselage structure to overpressure. It was expected that air blast and initial nuclear radiation input data for shallow- and intermediate-depth underwater explosions would be obtained during Operation Hardtack. Thus, the free-air effects as well as helicopter response data would be available, from which the delivery capability could be defined.

1.3 THEORY

1.3.1 Applied Aerodynamic Loads. The aerodynamic loads that originate from the rotors and fuselage of the helicopter in response to a blast input were calculated using equations of motion which made possible an analysis of dynamic maneuvering load, stability, and control for the helicopter in six degrees of freedom. This included not only motions of the helicopter in space, but also determination of angle of attack at the tip of the retreating rotor blade and rotor blade flap-

ping angle relative to the shaft when the blade was over the tail cone. These later parameters served as the basic means of monitoring development of stall in the rotor, and rotor blade clearance over the tail cone, respectively.

The general equations of motion, which are subject to the limitations of linear assumptions, are presented in detail in Appendix B, together with expressions for the helicopter derivatives. The helicopter derivatives were broken down into the contributions of the main rotor, the tail rotor, and the fuselage-wing-tail combination. Baily Twisted Rotor Theory (References 1 and

Figure 1.1 HSS-1 helicopter instrumented for Operation Plumbbob.

2) was used for the calculation of rotor derivatives. Wind tunnel data for lift, drag, pitching moment, yawing moment, and side force were used to evaluate the fuselage-wing-tail derivatives.

Since the predicted gust-load factor for all events was less than the design load factor for the helicopter, it was considered that the gust-load factor would not be a direct structural limitation but could become critical because of its influence on blade stall. It has been determined experimentally that blade stall is accompanied by an abrupt increase in control forces. Therefore, as a means of determining the severity of blade stall, stationary-star control forces were measured during all flight conditions. Since the severity of blade stall is a function of the retreating-blade indicated tip speed, which is affected by aircraft airspeed, blade rotational velocity, density altitude, aircraft gross weight, and flight load factor (Table 4.1), these factors were considered for each event and a retreating-blade indicated tip speed was calculated. The stationary-star vibratory load was then determined from Figure 1.3, which is the experimentally determined plot of stationary-star vibratory load versus retreating-blade indicated tip speed. This plot was based on the accumulation of test data obtained by flight test prior to Operation Plumbbob. This correlation is included in Figure 1.3.

1.3.2 Overpressure. Overpressure predictions were made from Figure 1.2 by use of modified Sach's scaling. Equation 1.1 was used in scaling the actual slant range (R^1) to a reduced

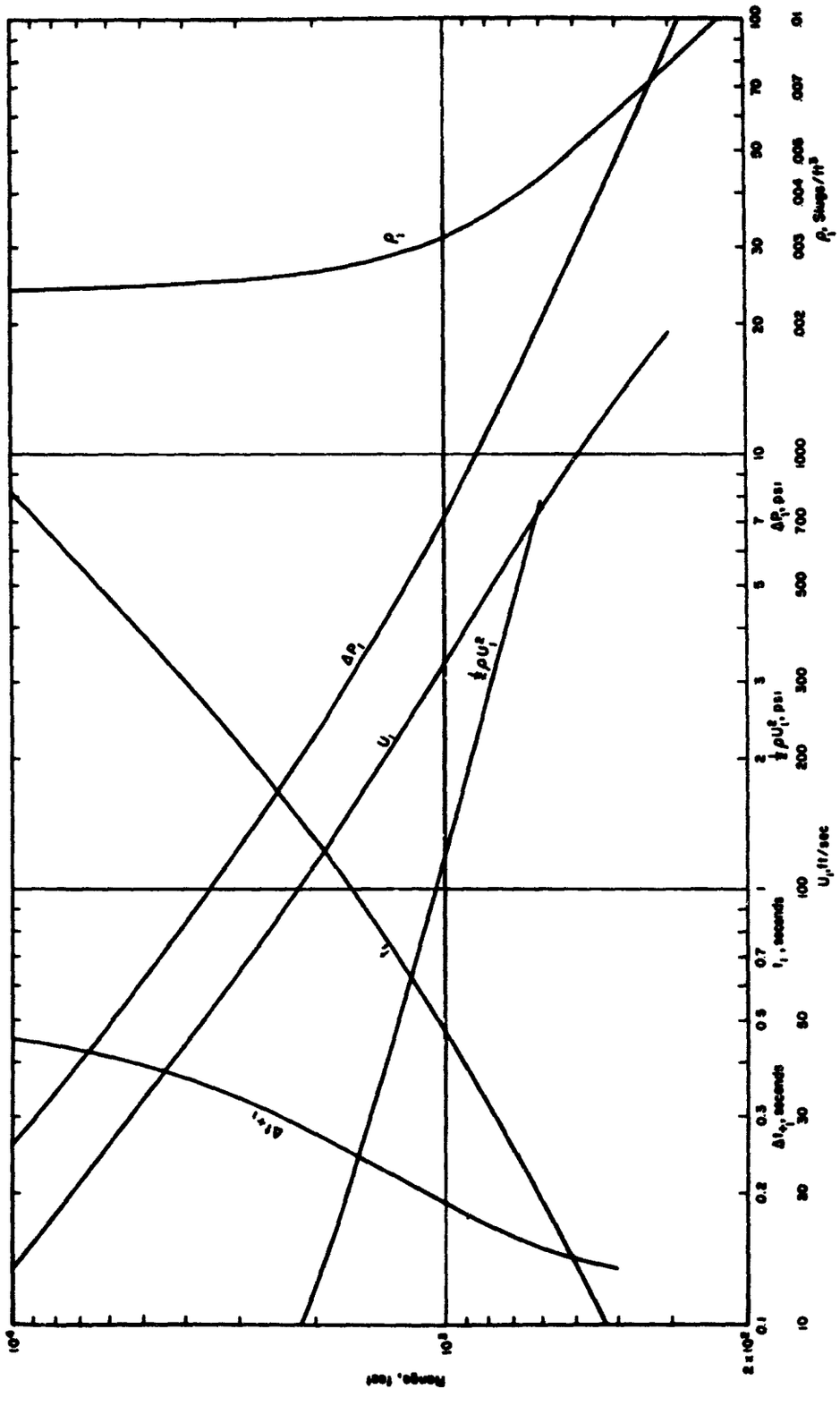

Figure 1.2 Weapons effects parameters.

slant range (R_1) for use in Figure 1.2 to obtain parameters for a 1-kt burst in a sea-level homogeneous atmosphere.

$$R_1 = R^1 \left(\frac{W_1}{W^1}\right)^{1/3} \left(\frac{P_0^1}{P_0}\right)^{1/3} \tag{1.1}$$

Where: R^1 = actual slant range, feet
R_1 = (range for unit yield under standard conditions) reduced slant range for entry into Figure 1.2, feet
W^1 = radiochemical or fireball yield, kilotons; (2 W^1 was used to calculate scaled ranges outside triple point path)
W_1 = 1 kt
P_0 = ambient pressure at sea level (NACA standard day), psi
P_0^1 = ambient pressure at aircraft altitude, psi

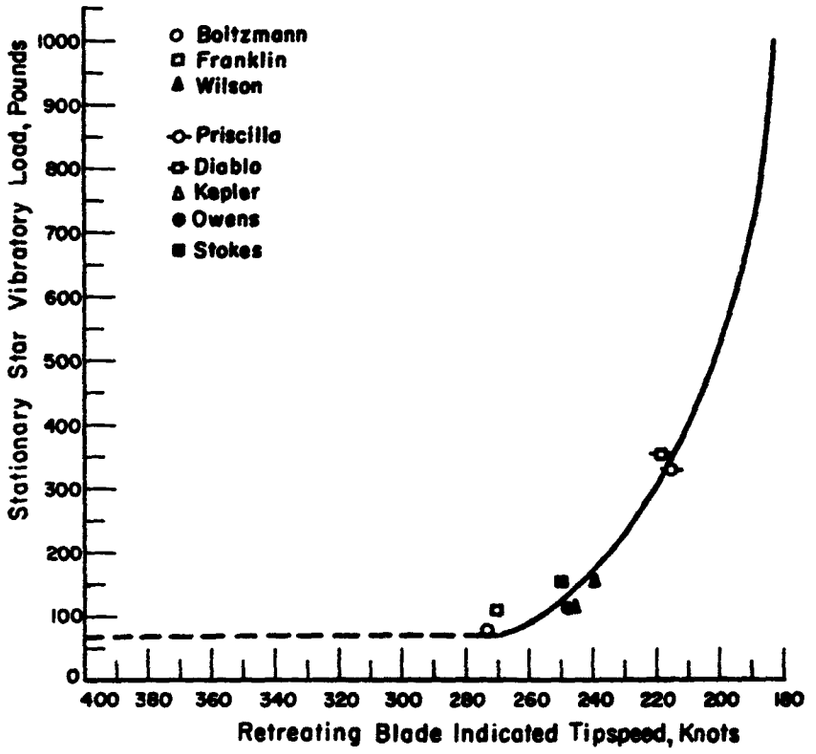

Figure 1.3 Stationary-star load versus retreating-blade indicated tip speed.

The overpressure obtained from Figure 1.2 was scaled by use of:

$$\Delta P^1 = \Delta P_1 \left(\frac{P_0^1}{P_0}\right) \tag{1.2}$$

Where: P_1 = overpressure obtained from Figure 1.2 for slant range R_1, psi
P^1 = predicted overpressure for actual position and yield, psi

1.3.3 Time of Shock Arrival. The time of shock arrival obtained from Figure 1.2 at the reduced slant range was scaled by use of:

$$t^1 = t_1\left(\frac{C_0}{C_0^1}\right)\left(\frac{W^1}{W_1}\right)^{1/3}\left(\frac{P_0}{P_0^1}\right)^{1/3} \tag{1.3}$$

Where: t_1 = time of shock arrival obtained from Figure 1.2 for slant range R_1, sec

t^1 = time of shock arrival at desired altitude and actual yield, sec

C_0 = speed of sound at sea level for NACA standard day, ft/sec

C_0^1 = speed of sound at aircraft altitude, ft/sec

1.3.4 Additional Gust Parameters. Density and gust velocity behind the shock front and the duration of positive phase were obtained from Figure 1.2 at the reduced slant range and scaled by Equations 1.4 through 1.6.

$$\rho^1 = \rho_1\left(\frac{\rho_0^1}{\rho_0}\right) \tag{1.4}$$

Where: ρ^1 = density behind the shock front for actual altitude and yield, $lb\text{-}sec^2/ft^4$

ρ_1 = density from Figure 1.2 at slant range R_1, $lb\text{-}sec^2/ft^4$

ρ_0^1 = ambient density at receiver altitude, $lb^0\text{-}sec^2/ft^4$

$$U^1 = U_1\left(\frac{C_0^1}{C_0}\right) \tag{1.5}$$

Where: U^1 = gust velocity behind the shock front for actual altitude and yield, ft/sec

U_1 = gust velocity from Figure 1.2 at slant range R_1, ft/sec

$$t_+^1 = t_{+_1}\left(\frac{C_0}{C_0^1}\right)\left(\frac{W^1}{W_1}\right)^{1/3}\left(\frac{P_0}{P_0^1}\right)^{1/3} \tag{1.6}$$

Where: t_+^1 = time duration of the positive phase for actual altitude and yield, sec

t_{+_1} = time duration of the positive phase obtained from Figure 1.2 at slant range R_1, sec

1.3.5 Overpressure Response. Preliminary calculations had indicated that a crushing of the fuselage, caused by overpressure, would be the major limitation for the helicopter. In order to minimize this effect, the windows and doors of the helicopter were opened during all participations to provide maximum differential pressure relief. During the initial phase of the tests, reinforcements consisting of horizontal crossbraces between the frames were installed in the tail cone to permit gust response data to be obtained at higher overpressure levels. A maximum overpressure limit of 1.0 psi for the reinforced helicopter was established, prior to the test, based on theoretical calculations. A few strain gages had been installed at critical fuselage stations for monitoring fuselage stresses resulting from blast effects. After the first three participations, a comparison of the measured stresses and the critical stresses for those mem-

bers indicated that the overpressure limit of 1.0 psi was conservative and on the basis of such comparison a new overpressure limit of 1.4 psi was established.

In order to obtain data on the basic aircraft during the second phase of the tests, the reinforcements were removed. Prior to this phase, a static pressure test was made on an unreinforced HSS-1 tail cone. Failure of the tail cone occurred at 0.9-psi static pressure. This value was reduced by both an assumed magnification factor of 1.5 and the allowable-to-ultimate ratio of 1.5 to establish an allowable overpressure limit of 0.4 psi for the first participation with the reinforcements removed.

1.3.6 Total Effective Radiant Exposure. The total radiant exposure normal to the receiver was computed from:

$$Q_{TN} = \frac{85.7\, W_{TH}\, e^{-KD}}{D^2} \left(\sin\beta + A\frac{Q_{RN}}{Q_I} e^{-KD/2} + \frac{Q_{SN}}{Q_I} \right) (1-F)\, K_1 \qquad (1.7)$$

Where: Q_{TN} = total radiant exposure normal to receiver, cal/cm^2

W_{TH} = thermal yield, kilotons

D = slant range, 10^3 ft

K = attenuation coefficient, per 10^3 ft

β = angle between the receiving surface and the direct radiant path, degree

A = albedo (0.4 for NTS area)

$\frac{Q_{RN}}{Q_I}$ = ratio of the normal component of reflected radiant exposure to the direct radiant exposure

$\frac{Q_{SN}}{Q_I}$ = ratio of normal components of scattered radiant exposure to the direct radiant exposure

$(1-F)$ = flyaway factor

K_1 = factor to account for fireball distortion and area seen by receiver

1.3.7 Temperature Rise. The usual expression for temperature rise in an air-borne receiver is:

$$\Delta T = Q_{TN}(1-H)\left(\frac{a}{G}\right) \qquad (1.8)$$

Where: ΔT = temperature rise, F

$(1-H)$ = cooling factor

a = absorptivity of surface

G = thermal capacity of material, cal/cm^2 F

Equations 1.7 and 1.8 were modified for the HSS-1 by disregarding the cooling and flyaway factors. This was possible due to the low speed of the helicopter and the lack of cooling over portions of the main-rotor blades. A maximum allowable temperature of 300 F was established for the rotor blades.

1.3.8 Nuclear Radiation. The nuclear radiation was calculated by the method presented in Reference 3, as modified by the Bureau of Aeronautics. These modifications included the use of a factor of 1.25 instead of 2.0 to compensate for an air-borne receiver, disregarding any reduction for flyaway and cockpit shielding. Nuclear radiation was not critical for any of the HSS-1 participations.

Chapter 2
PROCEDURE

2.1 OPERATIONS

2.1.1 Positioning System. The HSS-1 helicopter was positioned by use of a modified M-33 gun-tracking radar. This equipment utilized a plotting board with a pen recorder for tracking. The desired pattern was drawn to scale, and a controller compared aircraft position with the desired position and transmitted corrections to the pilot by UHF radio. A computer was designed for the M-33 radar which solved the positioning problem and presented the necessary corrections as time early or late and the speed change required to arrive at the desired position at time zero. This computer proved undesirable, since the helicopter's response to surface winds prevented an accurate solution. A brush-type recorder system was installed to provide azimuth, range and elevation for after-the-fact positioning data. The after-the-fact recording systems included a time-zero signal from a blue-box circuit and continuous 1-second timing marks. Time of shock arrival was determined from instrumentation in the helicopter and was used for determining the after-the-fact position at time of shock arrival. The accuracy of the after-the-fact positions was determined to be approximately ±200 feet.

2.1.2 Operation Considerations. In most of the events the helicopter was positioned for a tail-on orientation to the blast. For this orientation, an offset pattern was utilized with a 90-degree turn for a radial run-out just prior to time zero. This pattern was considered necessary for safety of crew and aircraft, since all participations were at relatively low altitudes. These offset patterns decreased the positioning accuracy due to wind effects in the final turn and the flight characteristics of the helicopter. The positioning errors varied from 0 to 5 seconds, which was small in terms of distance since a speed of 150 ft/sec was used in the pattern.

Abort criteria were not required for these offset patterns since the aircraft position errors along the intended flight path at the time of turn made little difference in the resulting distance from ground zero. Figure 2.1 shows the helicopter's desired flight pattern for Shot Priscilla with positions included for 10 seconds early or late at the H−40-second position.

Normal helicopter participation consisted of takeoff at H−54 minutes, two practice orbits around a racetrack pattern approximately 8 naut mi in length, a final run-in from H−5 minutes with a 90-degree turn at H−40 seconds, and landing at H + 30 minutes. An average of four practice flights were flown prior to each actual mission. Aircraft availability was good throughout the program.

2.2 INSTRUMENTATION

Recording instrumentation installed in the HSS-1 helicopter consisted of two 36-channel oscillographs and a photopanel recorder.

An overpressure pickup was installed on the aft section of the tail rotor pylon to provide a time history of overpressure. A differential pressure gage was installed on the tail cone skin to provide a time history of pressure difference between the inside and outside of the tail cone. Strain gages were installed on critical fuselage structural members to determine the effect of overpressure and aircraft accelerations on fuselage stresses. The pressure gages were calibrated against a manometer. Using information furnished by the strain gage manufacturer and a known calibrating resistance in the bridge circuit, a calibration of stress in terms of bridge output was obtained using the standard strain-gage formula.

Aircraft response to gust was measured by vertical, lateral, and longitudinal linear accelerometers mounted at the center of gravity, and vertical and lateral linear accelerometers mounted on the tail-rotor gear box. Additional data was obtained from aircraft attitude gyros and angular accelerometers mounted to measure pitch, roll, and yaw accelerations. Strain gages were installed on main-rotor and tail-rotor blades and controls to measure stresses and control forces. The strain gages were calibrated in the laboratory using known static loads and resistance-calibrated in the field prior to and after each participation. Potentiometers

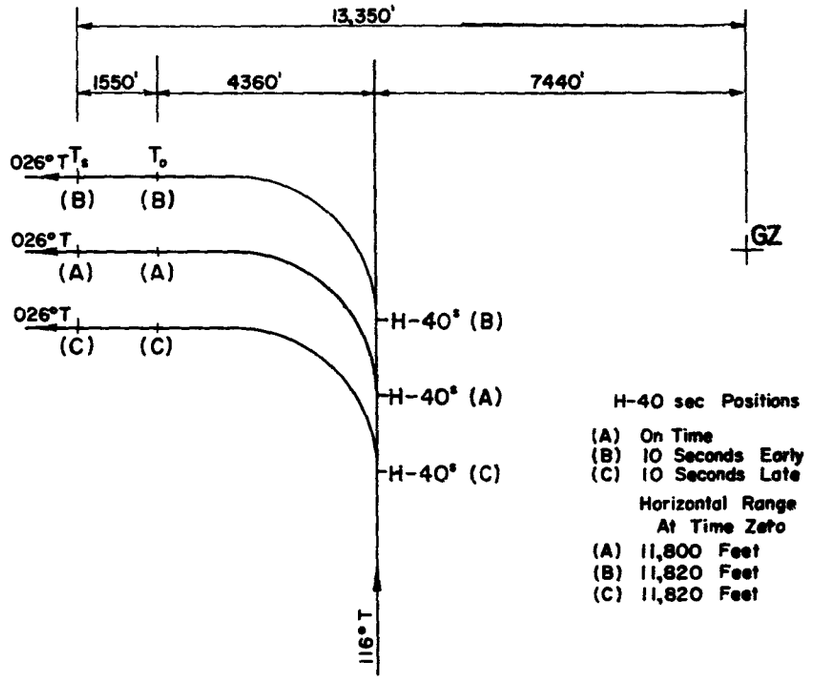

Figure 2.1 Planned and early or late flight patterns for HSS-1 helicopter for Shot Priscilla.

were installed to measure control displacements and were calibrated prior to and after each participation by deflection of the controls to their limits.

Temperature-sensitive strain gages were installed on the main-rotor blades to measure blade skin temperature at two positions on the underside of the blades. Calorimeters were installed on the tail pylon pointing downward to obtain information on indirect radiant exposure. The temperature gages were resistance-calibrated and the calorimeters were calibrated by the Naval Radiological Defense Laboratory prior to and after each participation.

Miscellaneous instrumentation was installed to measure such items as time of explosion, engine operating conditions, airspeed, altitude and amount of nuclear radiation.

Detailed information on the instrumentation of the HSS-1 is included in Appendix A.

2.3 DATA REQUIREMENTS

2.3.1 General Considerations. The HSS-1 helicopter was positioned at heights above burst point of from 1,000 to 6,000 feet and at various ranges in order to obtain gust-response data at several blast incidence angles and overpressure levels to simulate the range of effects expected for an underwater shot. During this phase of the tests, reinforcements were installed in the tail-cone section and the doors and windows were open to alleviate the crushing effects of over-

pressure. This permitted data on gust response to be obtained at higher overpressure levels than would have been possible with an unreinforced aircraft.

The second phase of the test beginning with Shot Kepler was without the reinforcements, with the doors and windows open, and at low overpressure levels to determine the effects of differential overpressure on the basic aircraft structure. In addition to these aircraft configurations, participation in one side-on orientation was included to obtain data of primary interest to the Army Transportation Corps.

Preliminary structural analysis indicated that the HSS-1 would safely withstand an overpressure of 1.0 psi with reinforcements installed and the doors and windows open. A participation

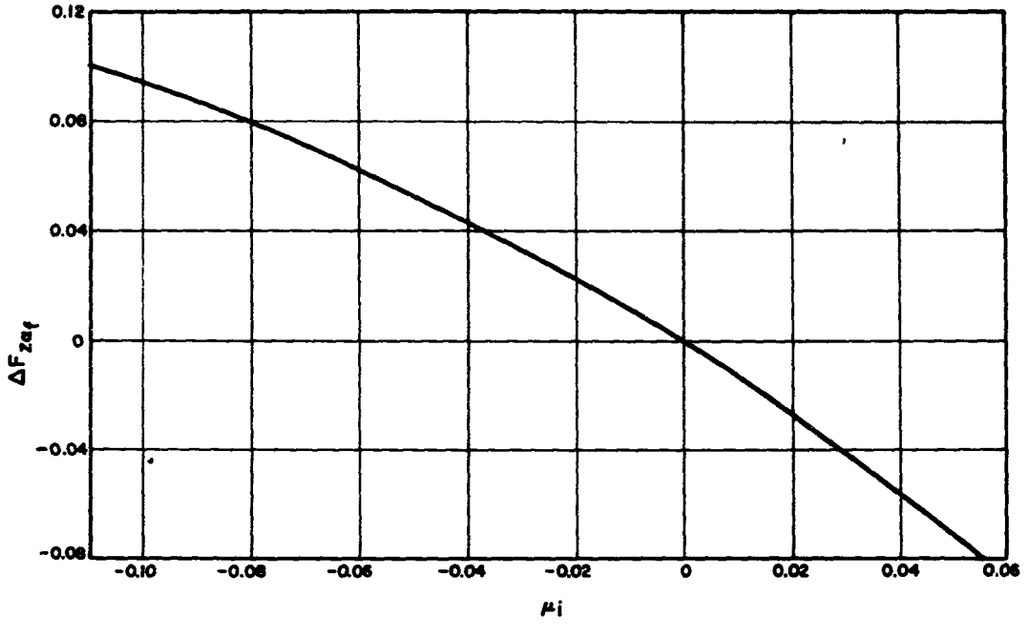

Figure 2.2 $\Delta F_{z\alpha_f}$ versus μ_i nonlinearity for Shot Priscilla.

schedule was established for 0.4- and 0.6-psi overpressure prior to positioning for the maximum value of 1.0. After obtaining 0.47 psi during Shot Boltzmann and 0.57 during Shot Wilson, data analysis indicated that the original limit of 1.0 psi was low and a new limit of 1.4 was established. This new limit permitted positioning which enabled an overpressure of 1.07 psi to be obtained during Shot Priscilla. By changing the altitude, airspeed, and rotor rpm, a build-up of stationary-star load and load factor was obtained during this phase.

2.3.2 Thermal Effects Data Correlation. Because of the low value of both predicted and measured thermal data no correlation was attempted.

2.3.3 Aerodynamic Response Data Correlation. The measured stability variables which describe the rigid-body response were compared with the corresponding values calculated by the methods discussed in Appendix B. In usual investigations of helicopter stability and control wherein deviations of major variables from their equilibrium values are relatively small, the limitation of linear assumptions assigned to the general equations of Appendix B permits satisfactory solutions to be made. For the case of the present tests, the perturbations of angle of attack, α_0, and rotor tip speed ratio, μ_i, covered such a range that it was necessary to account for nonlinearity in several of the helicopter derivatives. The numerical values for the variation in these nonlinear derivatives are shown in Figures 2.2 through 2.5. These deriva-

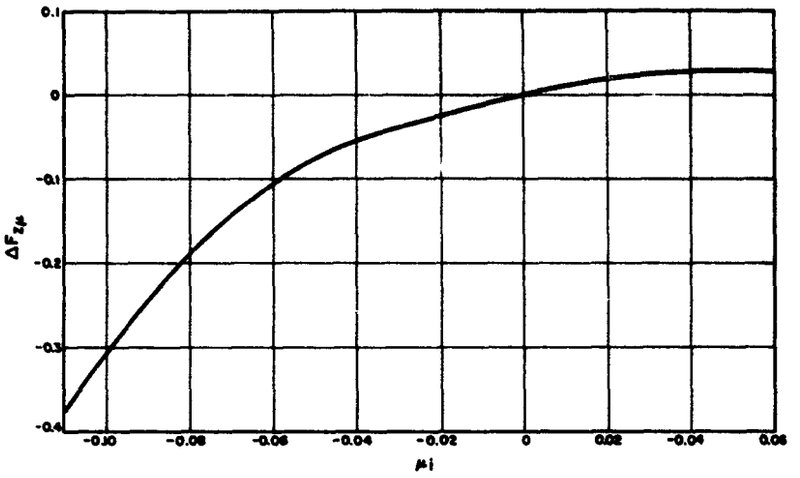

Figure 2.3 $\Delta F_{z\mu}$ versus μ_i nonlinearity for Shot Priscilla.

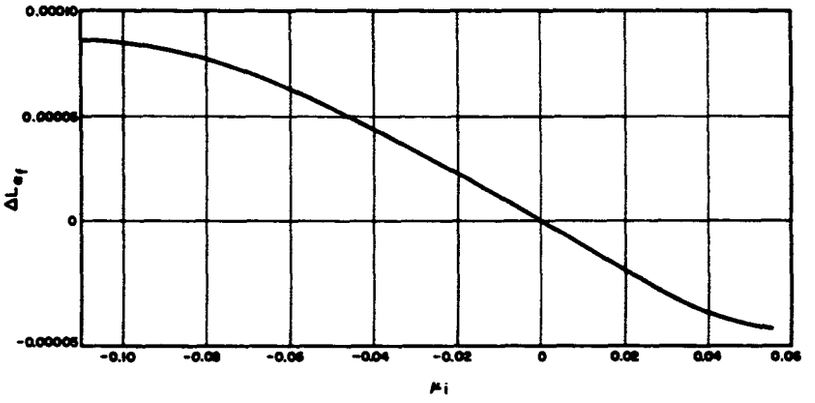

Figure 2.4 ΔL_{α_f} versus μ_i nonlinearity for Shot Priscilla.

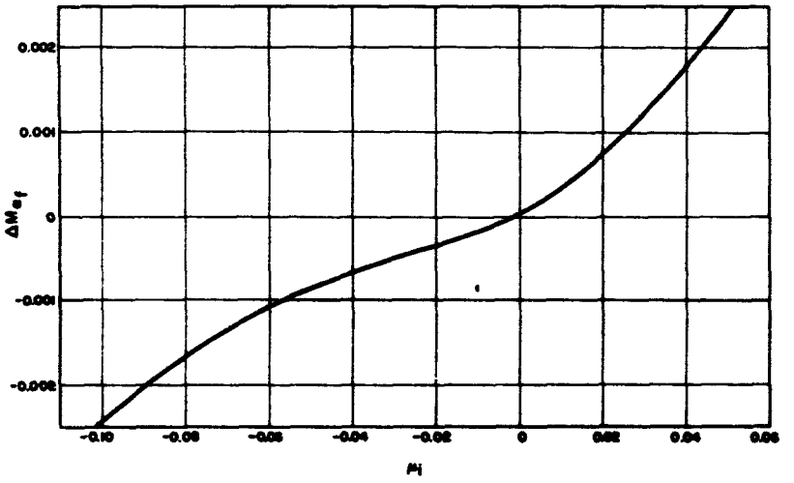

Figure 2.5 ΔM_{α_f} versus μ_i nonlinearity for Shot Priscilla.

tives were calculated from Equations 25, 27, 32, and 46 in Section B.2.6 by holding all major variables except μ constant at their trim values. An illustration of the incorporation of nonlinear derivatives into the general equations of motion is presented in Table B.2, Appendix B.

Effect of Downwash Lag. In view of the rapidly applied gust inputs to the rotor, it would be expected that a certain period of time would lapse before the steady-state downwash field could change. For lack of better information, it was assumed during the time of peak gust response that the rotor developed increased thrust as predicted by the theory of Appendix B but operated for a short period of time in the downwash field associated with the steady-state flight conditions existing before shock arrival. The assumed downwash field thus lagged that which would be theoretically associated with the calculated values of rotor thrust. A steady-state downwash field corresponding to the actual value of thrust is assumed to have developed by the time the overpressure entered its negative phase.

In this analysis the effect of downwash lag is accomplished by varying parabolically the lift slope of the rotor from that value containing no effects due to change in downwash angle at the time for peak gust response to the steady-state values of lift slope at the time when the overpressure enters the negative phase.

The equation for rotor lift slope without the effect of change in downwash angle is:

$$\frac{\partial C_T/\sigma}{\partial \alpha} = \frac{a}{2} \frac{t_{(3.1)}\mu}{\cos^2 \alpha}$$

The expression for steady-state lift slope is given by Equation 2 of Section B.2.7. The downwash lag effect is included in the appropriate nonlinear derivatives by the following relationships:

For $0>\mu_i$ only:

$$\Delta F_{z\alpha_{f(D.L.)}} = \Delta F_{z\alpha_f} + \frac{[F_{z\alpha_f\infty}(\mu_i = \min) - F_{z\alpha_f}(\mu_i = \min)]}{\mu_i^2 \min} \mu_i^2$$

$$\Delta L_{\alpha_{f(D.L.)}} = \Delta L_{\alpha_f} + \frac{[L_{\alpha_f\infty}(\mu_i = \min) - L_{\alpha_f}(\mu_i = \min)]}{\mu_i^2 \min} \mu_i^2$$

$$\Delta M_{\alpha_{f(D.L.)}} = \Delta M_{\alpha_f} + \frac{[M_{\alpha_f\infty}(\mu_i = \min) - M_{\alpha_f}(\mu_i = \min)]}{\mu_i^2 \min} \mu_i^2$$

Where the subscripts have the following connotations:

(D.L.) = derivative corrected for downwash lag
∞ = derivative calculated using rotor lift slope contained in Equation 1
$(\mu_i = \min)$ = value of derivative calculated at peak gust velocity

The curves for nonlinear derivatives shown in Figures 2.2, 2.4, and 2.5 contain these corrections for downwash lag.

Load Factor Equation. The equation for normal load factor during the first few seconds is:

$$L.F. = 1 + \frac{\Delta C_T/\sigma}{C_T/\sigma}$$

Where: C_T/σ = helicopter thrust coefficient solidity ratio for trim
$\Delta C_T/\sigma$ = change in thrust coefficient solidity ratio due to dynamic response of helicopter to gust input

In terms of helicopter derivatives:

$$\text{L.F.} = 1 - \frac{(F_{z\alpha_f} + \Delta F_{z\alpha_f})}{(C_T/\sigma)\cos^2 \alpha_i} \alpha_f$$

Where: $\Delta F_{z\alpha_f}$ is obtained from Figure 2.2 as a function of

$\alpha_i = \alpha_G - B_{i_S}(\text{Pilot}) - B_{i_S}(\text{Autopilot})$

α_f = helicopter angle of attack relative to flight path

It is of interest to note in Equation 6 that the perturbations of angle of attack, α_G, introduces nonlinearity by virtue of the $\cos^2 \alpha_i$ term. It is also of interest to note that the $\cos^2 \alpha_i$ term is not included in calculation of $F_{z\alpha_f}$ because α_i is not known when that calculation is made. The evaluation of Equation 6 for Shot Priscilla is presented as Equation 7 in Table B.2.

Autopilot Equations. Equations 8, 9, and 10 of Table B.2 are the equations of the autopilot in roll, pitch, and yaw. These equations were included because the autopilot was operative in these three channels during impingement of the blast wave. An altitude channel was not included because this autopilot channel was not operative during blast impingement.

Angle of Attack at the Tip of the Retreating Rotor Blade and Blade Flapping. Equation 11 of Table B.2 is the equation for angle of attack at the tip of the retreating rotor blade. The general equation for this stall parameter is as follows:

$$\alpha_{(1.0)(270°)} = \alpha_{(1.0)(270°)\,\text{trim}} + \Theta_0 + \frac{1}{1-\mu}\left\{\left(\frac{\partial a_i}{\partial \dot{\tau}}\right)(\dot{\alpha}_f + \dot{\tau}) + \left[\left(\frac{\partial \lambda}{\partial \alpha}\right) + \left(\frac{\partial a_i}{\partial \alpha}\right)\right]\alpha_f + \left[\left(\frac{\partial \lambda}{\partial \mu}\right) + \left(\frac{\partial a_i}{\partial \mu}\right)\right]\mu - \left[\left(\frac{\partial \lambda}{\partial \alpha}\right) + \left(\frac{\partial a_i}{\partial \alpha}\right)\right]B_{i_S}\right\}$$

The expression for the rotor derivatives $\partial a/\partial \dot{\tau}$, $\partial \lambda/\partial \alpha$, etc., are presented in Section B.2.7. It is emphasized that in Equation 7, Θ_0, α_f, μ, B_{i_S}, are not the trim values of these parameters but the time variation of these parameters from the trim values during the disturbance.

Equation 12 of Table B.2 is the equation for blade flapping relative to the shaft when the blade is passing over the tail cone. The general expression for this blade clearance parameter is as follows:

$$\beta_{B(\psi = 0)} = a_0\,\text{trim} - a_{i_S}\,\text{trim} + \left(\frac{\partial a_0}{\partial \alpha}\right)\alpha_f + \left(\frac{\partial a_0}{\partial \mu}\right)\mu - \left(\frac{\partial a_0}{\partial \alpha}\right)B_{i_S} + \left(\frac{\partial a_0}{\partial \Theta_0}\right)\Theta_0 - \left[\left(\frac{\partial a_i}{\partial \dot{\tau}}\right)(\dot{\alpha}_f + \dot{\tau}) + \left(\frac{\partial a_i}{\partial \alpha}\right)\alpha_f + \left(\frac{\partial a_i}{\partial \mu}\right)\mu + \left(\frac{\partial a_i}{\partial \Theta_0}\right)\Theta_0\right] + \left[1 + \left(\frac{\partial a_i}{\partial \alpha}\right)\right]B_{i_S}$$

The expressions for the rotor derivative $\partial a_0/\partial \alpha$, $\partial a_0/\partial \mu$, etc., are presented in Section B.2.7.

2.3.4 Stress Correlation. The unreinforced HSS-1 helicopter participated in only two shots for which stress correlation could be attempted. These were Shots Owens and Kepler, both

tail-on shots. Correlation could not be attempted for either the shots participated in by the reinforced HSS-1 or for Shot Stokes, a side-on shot, because of inadequate structural and pressure instrumentation.

Data required for the prediction of fuselage stresses due to nuclear blast effects were time histories of aircraft accelerations, tail-rotor thrust loads, and differential pressures. An examination of the loading data and the strength summary for the HSS-1 indicated that the critical structural area for these loads was the tail cone between Station 316 and Station 352.

From the intensity of the loading schedule, a first approximation of skin effectivity was made. This was substantiated by calculating the stress distribution due to aircraft flight loads at several time intervals during the shot and comparing the skin stresses with skin buckling allowances. An elastic analysis was then made of the gridwork of skin, stringers and frames in the critical tail-cone area for differential pressure loads. (Axial loads present in the system due to flight conditions were not considered here since the energy contribution of these loads to the complete system under pressure was negligible.) This elastic analysis, done in unit form, was then multiplied by the appropriate constants producing a time history of stresses due to differential pressure effects. The time histories of the stresses due to flight loads and those due to the differential pressure were then superimposed, yielding the net stress time relationship for the structure. These stresses were compared to the oscillograph traces of the appropriate test shot for correlation.

Since the frame stresses in the HSS-1 tail cone were relatively independent of flight loads, and responded to differential pressures with no appreciable time lag, agreement between the calculated and actual frame stresses was excellent. Correlation of stringer stress levels was, in general, only fair. There were several contributing factors affecting this, the most significant being the low load intensities resulting from low-yield Shots Owens and Kepler coupled with inadequacies of the instrumentation for structural strain correlation. In addition, dynamic effects, both on the accelerometer traces and the stress traces,could not be considered because of the difficulty in evaluating them. At low load levels, dynamic responses due to normal flight vibration alone had amplitudes large enough to significantly alter the trace patterns. An attempt to filter out these vibratory effects was made with limited success.

Conclusions as to the effectiveness of the stringer stress calculations cannot be reached from comparison with the available data. The only significant point that can be made is that the general stress levels were of correct magnitude.

Stress Analysis. Semimonocoque structures are composed of skin, stringers and frames. The skin distributes pressure to the stringers and frames and carries the major part of the shear stresses. The stringers are the main structural elements and carry the major part of the airframe bending moments. The frames maintain the shape of the structure and in some cases are used to introduce concentrated loads into the shell. However, this idealized distribution of function and loading, while reasonably accurate for design purposes, at design load intensities, is not correct at low load levels. The significant difference is in the effectiveness of the skin as bending material in conjunction with the stringers. Up to the point of elastic buckling of the skin panels, the entire skin is fully effective and materially affects the stress distribution. Shots Owens and Kepler produced such low load levels. Therefore, the method of determining the fuselage stresses resulting from these shots included a re-calculation of effective fuselage section properties. If the load level were above the skin-buckling criteria, a re-evaluation of the effective shell material would have again been necessary. The difference between the two conditions represents an area of proportionally greater increases in stringer stress, due to redistribution, for equal increases in shell loading.

Pressure effects, as stated above, are distributed by the skin to the gridwork composed of the stringers and frames. The frames on the HSS-1 tail cone are used primarily to maintain shape and to act as panel breaks and are therefore rather insensitive to flight loads. As a result, these light-gage channel-section frames proved to be critical for the bending stresses imposed by differential pressure on the shell. Allowable stresses were calculated for the frames under pressure and for the stringers under the combined effects of flight axial loads

and lateral bending due to pressure. The calculated allowable pressure for the frames is 0.71 psi design limit. The allowable for the critical stringer is a design envelope based on the relative intensities of differential pressure and flight loading.

Substantiation of the allowable frame crushing pressure was made by Sikorsky Aircraft by static testing two HSS-1 tail cones. The tail cones were instrumented and subjected to incremental increases in pressure until failure occurred. The static test specimens failed at 0.90 psi average.

Applied Loads. Loads affecting the HSS-1 tail-cone structure are inertia loads due to aircraft accelerations, tail-rotor loads, and differential pressures. Accelerometer traces taken during the shot were divided into suitable time increments and the inertial loads due to these accelerations were calculated for each instant of time. To these were added the loads caused by the tail rotor, yielding the net flight load distribution at the critical sections, for each instant of time.

The differential pressure for corresponding instants of time were obtained from the differential pressure trace directly.

Stress Distribution Due to Flight Loads. Cross-sectional stress distributions due to unit accelerations and unit tail-rotor loads were calculated by conventional methods programmed on an IBM 704 digital computer. The accuracy of these methods in the elastic range and where there are no structural discontinuities is well known. These unit distributions were multiplied by the appropriate coefficients determined by the time histories of the accelerometer traces and added together, yielding the net flight load distribution.

It was analytically determined that the variation of tail-rotor thrust during the time of the shot due to the effects of the blast would be less than 10 percent. The time history trace for Shot Kepler is shown in Figure 3.5. Since this change would cause an insignificant change in the stringer stress level at the critical stations, a steady tail-rotor thrust was used in calculating the stresses in Shot Owens. This thrust was equal to the balancing thrust for 1-g level flight.

Stress Distribution Due to Differential Pressure. Because of the high degree of redundancy and interaction, the differential pressure distribution on the gridwork of stringers and frames is best investigated by elastic analysis. The structure is analyzed by the method of minimum strain energy considering the tail-cone structure between Station 316 and Station 352 as an integrated stringer-frame network. The coupling of stringer axial stresses caused by flight loads is by super-position, as the strain energy due to axial loads is negligible compared with the total energy of the system.

An outline of the procedure followed in the analysis is presented below:

1. The redundant structure is made statically determinate and equilibrium equations are written for each structural element.
2. Individual element influence coefficients are written to sum up the total flexibility in the structure.
3. Steps 1 and 2 are written in matrix form and by matrix manipulation a unit load distribution is obtained for the entire structure.

The matrix operations are:

1. Unit deflections are found for the entire structure.
2. Next, the deflections based on the statically determinate structure are obtained.
3. These deflections multiplied by the internal and external loads yield the total energy in the system in terms of the applied and redundant loads.
4. The total energy is differentiated with respect to the applied loads and redundant loads to obtain the deflection equations.
5. Solution of the deflection equations produces the redundant loads, which, by matrix manipulation, yield the unit-load distribution.

In matrix notations:

1. $[\gamma_{im} \vdots \gamma_{ir}] [\alpha_i] = [\delta]$

2. $\frac{1}{2}[\gamma_{lm} | \gamma_{lr}][\delta] = [U]$

The structure considered in the analysis was between Stations 316 and 352 on the tail cone. This area included three frames (Stations 316, 334, and 352) and twenty stringers, symmetrically placed around the perimeter of the shell.

An assumption was made that the end frames at Stations 316 and 352 were rigid relative to the frames at Station 334. This assumption was substantiated by calculating the relative frame stiffness using Naval Advisory Committee for Aeronautics (NACA) TR-1097. Another assumption was that the stringers had full fixity at their ends. This assumption is valid since under a symmetrical uniform pressure load, and with equal bay lengths, the stringer slope across the frames is zero. The basic skin is not included in the idealized structure except locally as effective bending material with the stringers and frames. The reason for this is that the only function of the skin under a symmetrical pressure loading is to distribute this pressure to the supporting structure.

Because of the symmetry of both structure and loading about the vertical axis, only half of the structure needs to be considered. This structure was reduced to individual elements placed in load equilibrium, and coupled together by matrix operations.

Chapter 3
RESULTS

3.1 GENERAL

Tabulated results of pertinent recorded data at time zero and at the time of shock arrival are presented in Tables 3.4 and 3.5. Time histories of typical recorded data are presented in Appendix C. The presentation of data in tabular form has been limited to only those items of recorded data that were of major significance or were necessary for correlation at either time zero or time of shock arrival. All other pertinent data are presented as time histories. Because of the cyclic nature of the data recorded, it was considered that this was the more desirable and illustrative method of presentation. Table 3.1 is the summary for events in which the HSS-1 helicopter participated, and which were utilized for postshot correlation. Tables 3.2 and 3.3 are summaries of aircraft positions and atmospheric conditions.

3.2 GUST RESPONSE DATA

Dynamic response data measured during the test operations consisted of basic flight parameters and representative stresses in the rotor blades.

Comparisons of calculated flight parameter data with flight test data are presented in Figures 3.1 through 3.3 for Shots Priscilla, Diablo, and Kepler, respectively. These three events were chosen because Shots Priscilla and Diablo represented the most severe conditions while Shot Kepler was typical of the remaining six participations. Comparisons between calculated and measured values are shown for five parameters, i.e., pitching, rolling and yawing accelerations, normal load factor, and blade flapping over the tail cone relative to the shaft. It can be seen from the typical time histories presented in Appendix C that no significant changes in rotor blade stresses occurred. This may be attributed to the fact that rotor blades are free to flap about their horizontal hinge, thereby reducing gust effects on the blades.

3.2.1 Shot Priscilla. Comparison of calculated data with flight-test data for Shot Priscilla is shown in Figure 3.1. For normal load factor, Channel 1, the peak calculated value corresponds well with the peak measured value but since rotor-blade inertia in independent flapping degrees of freedom was not considered in the calculations, the calculated peak-load factor leads the measured peak-load factor. Although the autopilot had no effect on the peak-load factor developed, it did restrict the reduction in load factor below 1.0 after the first second of time had elapsed. Comparison of calculated load factor with measured load factor after one second is good. It is noted that the high frequencies in the flight-test data attributed to local structural response have been eliminated in these load-factor plots. They did not possess the amplitude relative to the long-period mode and damped out much more rapidly than the high-frequency oscillations that occurred in the rolling, pitching, and yawing acceleration data.

In Channel 2 of Figure 3.1, the calculated rolling acceleration appears to be an average of the measured response. It is believed that the high-frequency oscillations measured by the accelerometer, which have not been faired out in this plot because of their high amplitude and low damping, were the results of local structural response combined with accelerometer response to the applied loads due to both overpressure and air mass velocity and are not generated by the main or tail rotors. Therefore, the calculated response did not predict their existence.

In Channel 3 of Figure 3.1, the calculated pitching acceleration appears to be a reasonable average of the measured response. The high frequencies in the measured response were again attributed to local structural response to the applied loads.

TABLE 3.1 SHOT DATA SUMMARY

Shot	Yield *	Date	Burst Height Above Terrain	Terrain Elevation, MSL
	kt		ft	ft
Boltzmann	11.5 ± 0.8	28 May 1957	500 Tower	4,235
Franklin	0.138 ± 0.006	2 June 1957	300 Tower	4,022
Wilson	10.0 ± 0.5	18 June 1957	500 Balloon	4,238
Priscilla	33.5 ± 1.0	24 June 1957	700 Balloon	3,080
Diablo	17.0 ± 0.85	15 July 1957	500 Tower	4,485
Kepler	10.0 ± 1.0	24 July 1957	500 Tower	4,320
Owens	9.2 ± 0.5	25 July 1957	500 Balloon	4,238
Stokes	18.9 ± 0.35	7 August 1957	1,500 Balloon	4,185

* Preliminary postshot.

TABLE 3.2 ACTUAL AIRCRAFT POSITIONS

Shot	MSL Altitude at Time Zero	Horizontal Range at Time Zero	Slant Range at Time Zero	MSL Altitude at Time of Shock Arrival	Horizontal Range at Time of Shock Arrival	Slant Range at Time of Shock Arrival
	ft	ft	ft	ft	ft	ft
Boltzmann	6,110	16,050	16,100	6,110	18,140	18,150
Franklin	8,000	7,411	8,260	8,000	8,487	9,240
Wilson	5,915	14,373	14,421	5,939	16,400	16,443
Priscilla	8,118	11,921	12,700	8,118	13,513	14,200
Diablo	10,998	10,422	12,560	10,992	11,991	13,405
Kepler	5,990	20,473	20,500	6,184	23,143	23,190
Owens	7,287	20,303	20,410	7,302	22,923	23,100
Stokes	8,430	33,240	33,400	8,276	33,180	33,220

TABLE 3.3 ATMOSPHERIC CONDITIONS

Shot	Pressure at Altitude at Time Zero	Pressure at Altitude at Shock Arrival	Temperature at Altitude at Time Zero	Temperature at Altitude at Shock Arrival	Wind at Altitude		Surface Visibility
					Direction	Velocity	
	psi	psi	F	F	degrees	knots	naut mi
Boltzmann	11.79	11.79	65.55	65.57	calm		Unrestricted
Franklin	11.04	11.04	65.66	65.66	calm		Unrestricted
Wilson	11.10	11.99	65.41	65.34	060	10	Unrestricted
Priscilla	11.04	11.04	69.06	69.06	230	8	Unrestricted
Diablo	9.94	9.94	51.80	51.84	170	6	Unrestricted
Kepler	11.84	12.25	70.88	70.56	060	6	Unrestricted
Owens	11.29	11.28	67.48	67.41	140	5	Unrestricted
Stokes	10.85	10.91	55.06	55.69	100	8	Unrestricted

TABLE 3.4 SUMMARY OF TIME ZERO DATA

Shot	Indirect Radiant Exposure *	Temperature Rise on Critical Surface (Main Rotor Blade)	Nuclear Radiation	
			Cockpit	Cabin
	cal/cm²	F	roentgens	
Boltzmann	0.0033	3	0	0
Franklin	0.0009	1	0.32	0.35
Wilson	0.0032	2	1.30	1.12
Priscilla	0.91	35	1.12 †	3.48 †
Diablo	0.054	17	0.06	0.11
Kepler	NMD ‡	1	NR §	NR §
Owens	0.004	3	0.07	0.07
Stokes	0.004	3	NR §	NR §

* Average of 3 calorimeters under tail pylon.
† Questionable data.
‡ No measurable deflection.
§ Not reduced.

TABLE 3.5 SUMMARY OF DATA AT TIME OF SHOCK ARRIVAL

Shot	Time of Shock Arrival		Peak Overpressure		Load Factor		Stationary-Star Load		Peak Differential Over-pressure	Incidence Angle of Blast Wave	Measured Stress Fuselage Station *	
	Predicted	Measured	Predicted	Measured	Predicted	Measured	Predicted	Measured			Stringer	Frame
	sec		psi		g		± pounds		psi	degrees	psi	
Reinforced:												
Boltzmann	14.73	14.25	0.395	0.47	1.10	1.11	70	75	0.47	4.0	−1,500 †	+800 ‡
Franklin	7.21	7.68	0.152	0.18	1.10	1.05	70	110	0.16	22.5	−1,350 †	+450 ‡
Wilson	13.03	12.54	0.426	0.57	1.15	1.15	170	150	0.50	4.1	−2,300 †	+650 ‡
Priscilla	10.65	10.12	0.916	1.07	1.78	1.80	350	325	0.80	17.8	−2,900 †	+900 ‡
Diablo	10.43	9.70	0.642	0.80	1.62	1.80	320	350	1.00	26.6	−4,100 †	+500 ‡
Unreinforced:												
Kepler	19.32	19.18	0.339	0.40	1.10	1.15	145	110	0.45	2.9	+4,200 §	+11,200 ¶
Owens	19.38	18.86	0.261	0.43	1.10	1.13	130	110	0.65	6.3	+3,300 §	+7,700 ¶
Stokes (side-on)	27.10	27.69	0.219	0.39	1.10	1.14	130	150	> 0.30 ††	4.8	+3,900 **	+7,300 ¶

* Total recorded stress, including flight loads, uncorrected for gage location. Refer to gage locations Table A.1 for fuselage station numbers.
† Gage B-30. ‡ Gage A-30. § Gage A-31. ¶ Gage B-29. ** Gage A-33. †† Trace undefined above 0.30 psi.

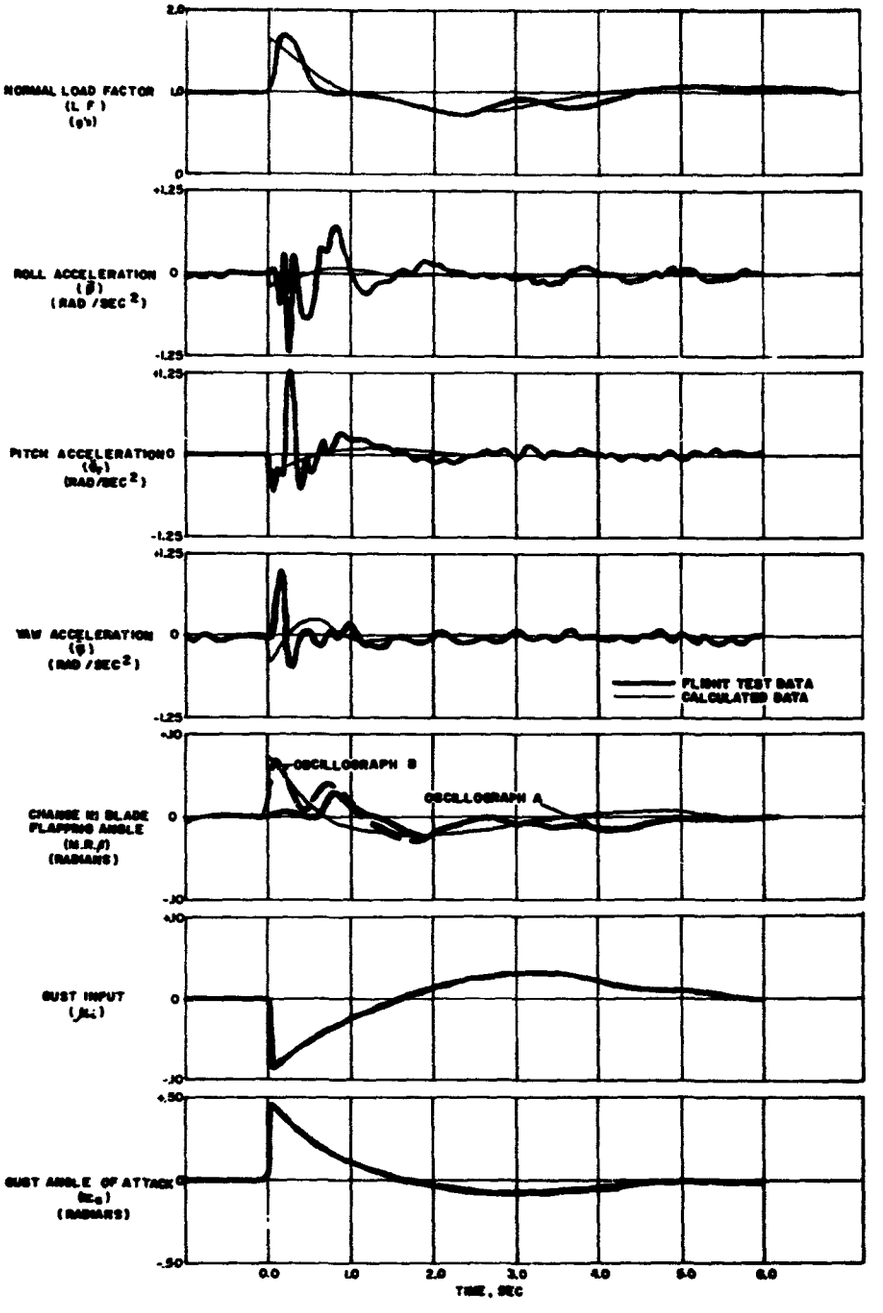

Figure 3.1 Correlation of calculated and test data for Shot Priscilla.

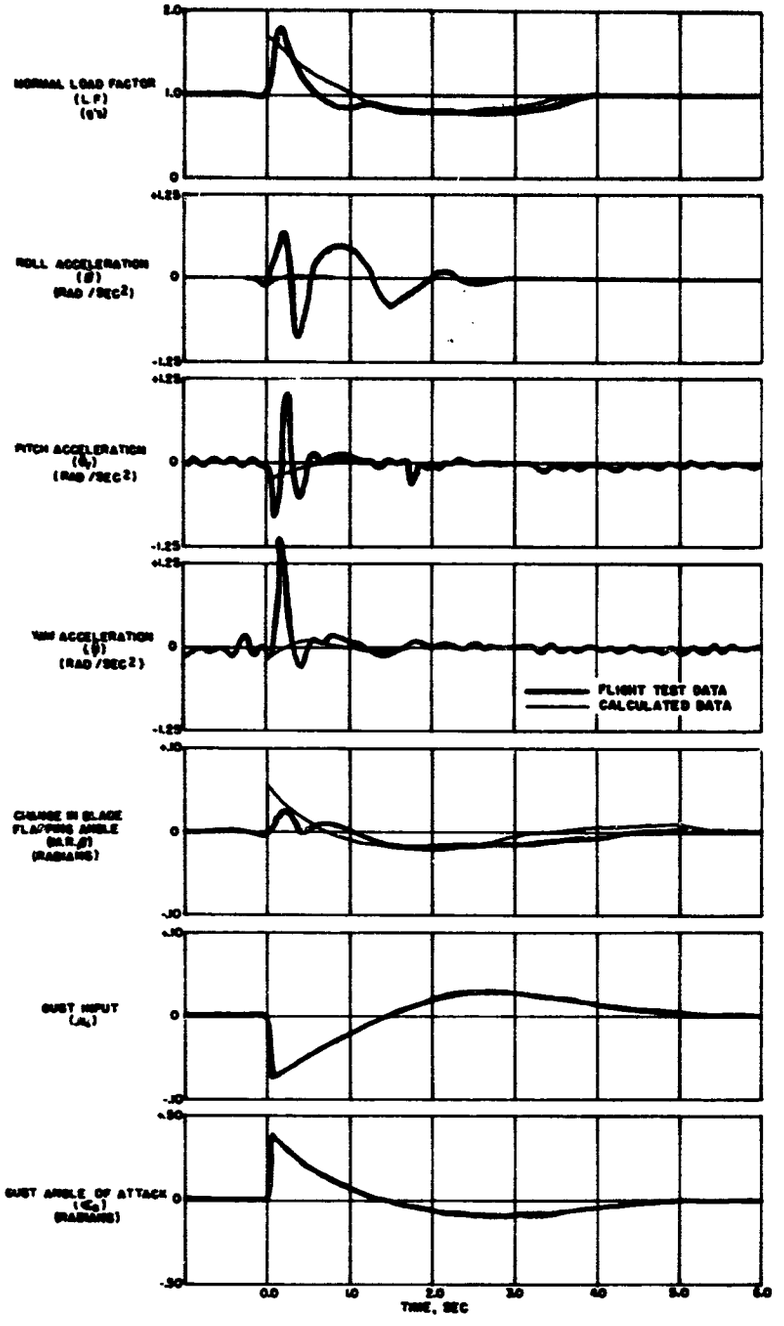

Figure 3.2 Correlation of calculated and test data for Shot Diablo.

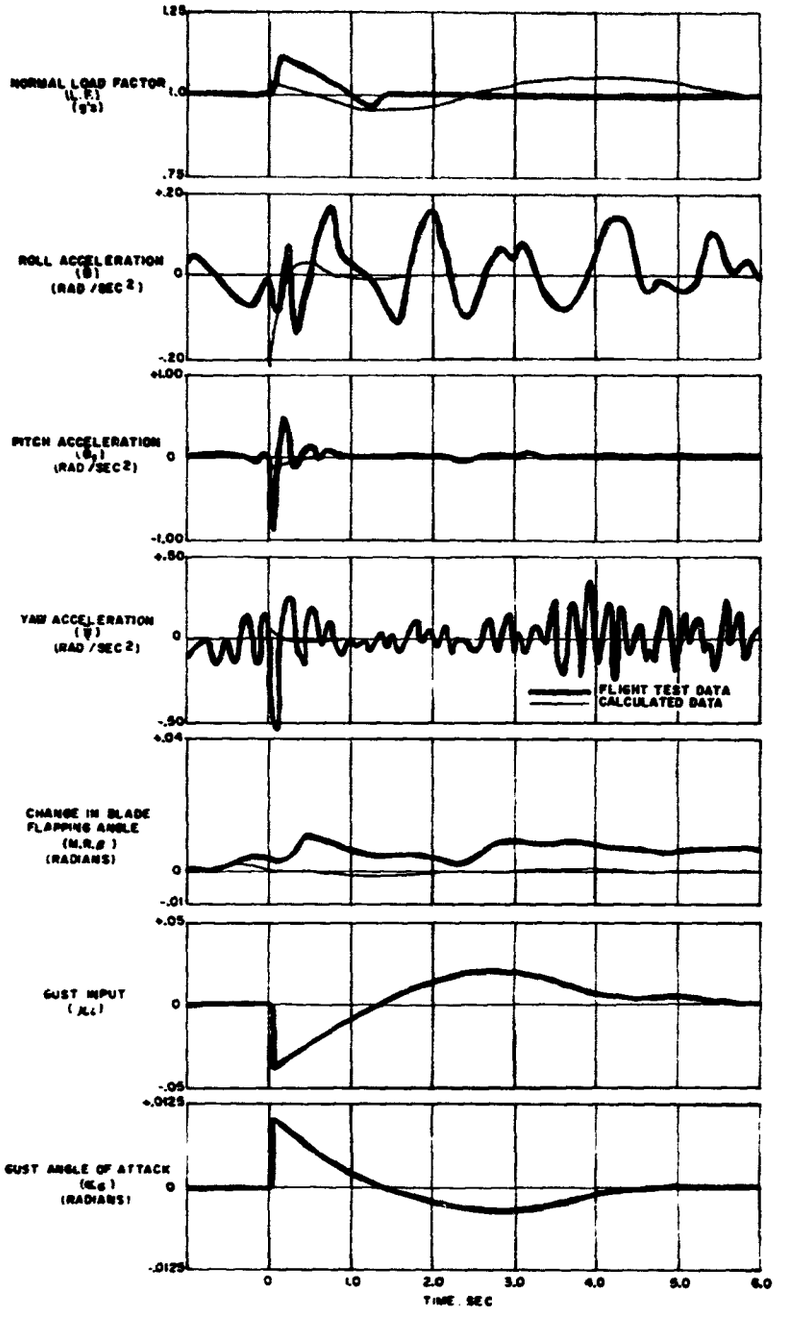

Figure 3.3 Correlation of calculated and test data for Shot Kepler.

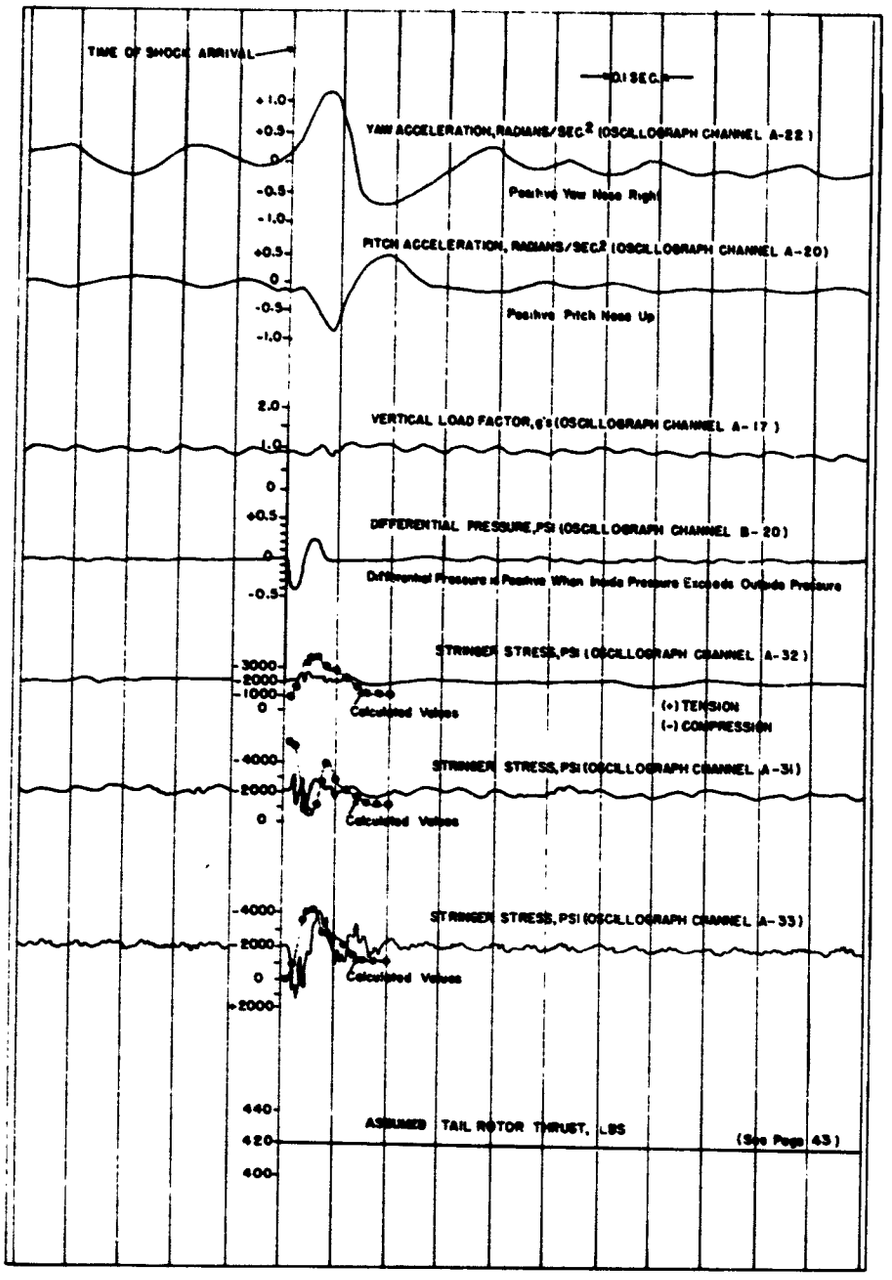

Figure 3.4 Time histories of fuselage stress measurements, Shot Owens.

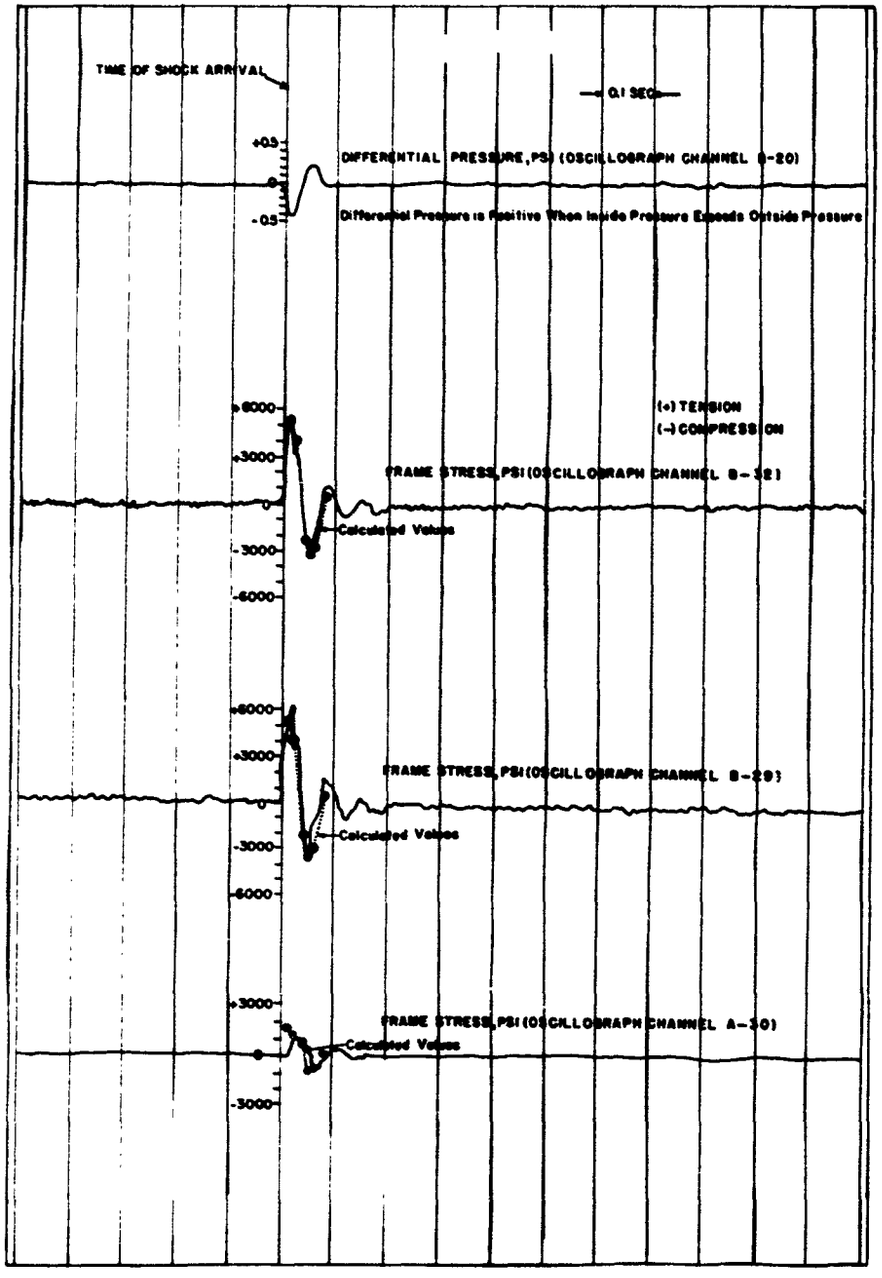

Figure 3.4 Continued.

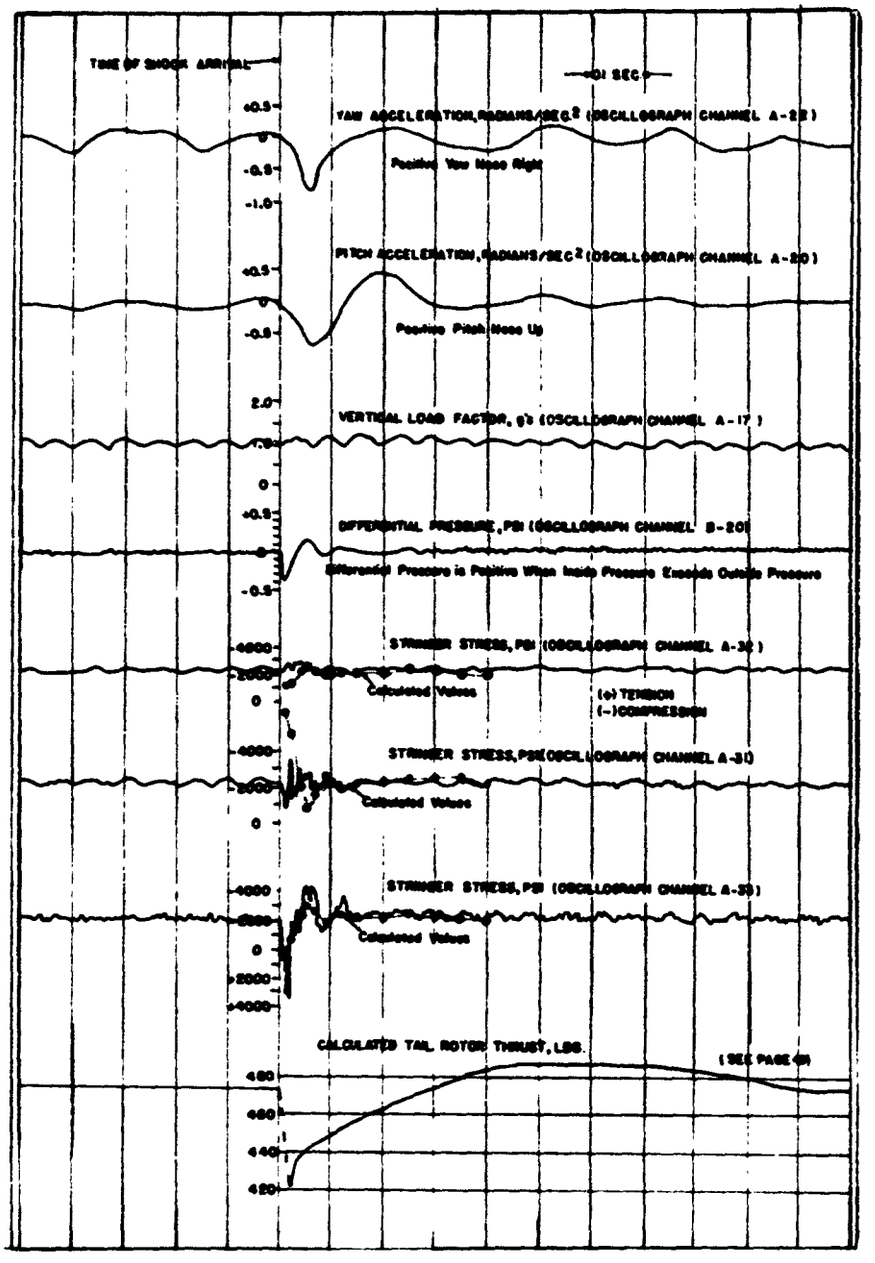

Figure 3.5 Time histories of fuselage stress measurements, Shot Kepler.

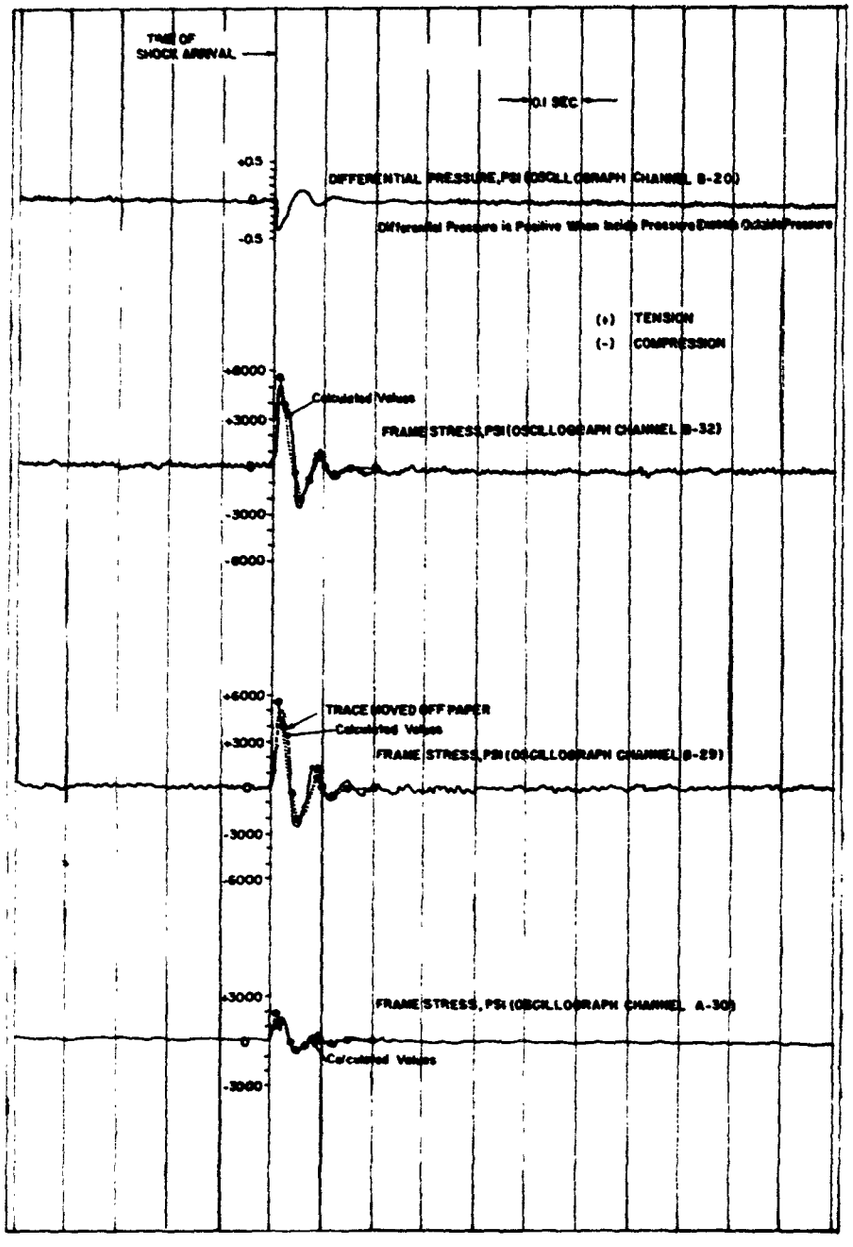

Figure 3.5 Continued.

For yawing acceleration (Channel 4 of Figure 3.1), comparison of the calculated response with the measured response is similar to the comparisons for rolling and pitching accelerations. The most severe acceleration sensed by the accelerometer was at the peak of a high frequency oscillation attributed to local structural response to the applied loads. The calculated response predicted an average value of these high frequency oscillations.

Comparison of the calculated change in rotor blade flapping over the tail cone relative to the shaft is shown in Channel 5 of Figure 3.1. For this blade-clearance parameter, the calculated peak flapping angle agreed closely with the measured value for the blade monitored by Oscillograph B, whereas poor correlation was established with the measured value for the blade monitored by Oscillograph A. The blade monitored by Oscillograph B was closer to the tail cone at

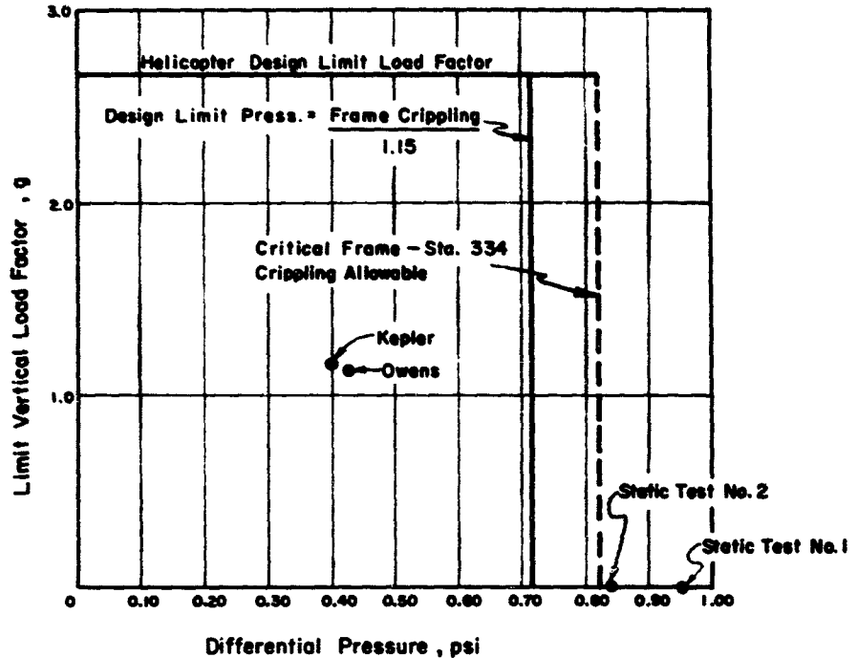

Figure 3.6 Helicopter structural limitation envelope.

the time of the blast and responded more nearly in the manner described by Equation 12 of Table

Flapping of neither blade exceeded the peak value calculated. The calculation did not predict the blade flapping oscillation occurring with a period of 0.8 second. This oscillation might be predicted when equations describing independent rotor-blade flapping degrees of freedom are introduced in the analysis.

For these correlation studies, the time histories, as shown in Channels 6 and 7 of Figure 3.1 of the gust input μ_i, and gust angle of attack, α_G, were calculated from the measured value of overpressure and orientation and were introduced directly into the analog computer. These disturbances have disappeared in 6 seconds or less; therefore, the calculation was terminated in 6 seconds.

3.2.2 Shots Diablo and Kepler. Comparisons of calculated data with flight test measured data is shown for Shot Diablo in Figure 3.2 and for Shot Kepler in Figure 3.3. Comparisons for these shots exhibit the same characteristics as those for Shot Priscilla. Prediction of the load-factor time history was satisfactory if the higher frequency oscillations with periods of the order of 0.2 second or less, excluded from these plots, are attributed to local structural

response to the applied loads. Only average values of the higher frequency oscillations were predicted for the rolling, pitching, and yawing accelerations. Blade flapping angle monitored by either oscillograph did not reach a value as high as the calculated value (only blade flapping from Oscillograph A is shown). The peak load factor comparison for Shot Kepler, Channel 1 of Figure 3.3, did not appear to be good; however, the difference between the calculated peak value and the measured peak value was only 0.06 g. This increment of load factor is believed to be of the order of the experimental error. This is also true of blade flapping where the total change in blade flapping measured in flight was not more than 1 degree.

3.3 FUSELAGE RESPONSE TO GUSTS, SHOTS OWENS AND KEPLER

The overpressure response data measured during the test operations consisted of overpressure, differential pressure between the inside and outside of the tail-cone skin at the critical area, and a number of fuselage frame and stringer stresses.

Comparisons of calculated frame and stringer stresses with flight-test data are presented in Figures 3.4 and 3.5 for Shots Owens and Kepler. These two shots were chosen,since all other participations were with reinforcements installed in the aircraft or were for a side-on orientation to the blast.

The method followed in predicting fuselage stresses resulting from blast effects is considered accurate for the frame stresses. The effectiveness of the method for predicting stringer stresses is still open to question since the data acquired during Operation Plumbbob did not prove or disprove the analysis. However, since the relative magnitudes of the predicted and actual stringer stresses were similar, it is felt that more generalized instrumentation might yield adequate correlation with stringer stresses as well. This instrumentation would be arranged to allow enough data to be gathered to properly evaluate dynamic effects as well as to verify critical transducers.

As can be seen by comparison with the analytically determined strength envelope presented in Figure 3.6, the evaluated test events for the unreinforced HSS-1 were well within design boundaries with considerable margin existing both in load factor and in pressure loading. The static test results for the frame under pressure alone fell slightly outside the theoretical pressure limit. This was within the calculation accuracy and is probably attributable to the failure actually beginning before any indication of such was recorded.

While the above limits are limits in the tactical sense, that is, precluding any structural damage whatsoever, it is considered pertinent to point out that failures of this nature may not necessarily involve flight safety. Since semimonocoque structures are multiply redundant, and, because a good deal of the structure is overstrength due to the limitations of minimum structural gages, a considerable amount of structural damage is tolerable before the aircraft becomes unsafe to fly.

Chapter 4
DISCUSSION

4.1 OVERPRESSURE AND TIME-OF-SHOCK-ARRIVAL CORRELATION

Comparison between the predicted and measured values of overpressure and time of shock arrival was made using the after-the-fact position of the aircraft, yield, and existing atmospheric conditions at shot time. The measured data were reduced to correspond to 1 kt burst at sea level by the scaling equation outlined in Section 1.3 and are plotted in Figure 4.1 with the basic curves for overpressure and time of shock arrival from Figure 1.2.

Measured values of overpressure were consistently higher than the values predicted by the method outlined in Section 1.3. Detailed explanation of this relatively poor correlation will not be attempted in this report. Overpressure instrumentation in the HSS-1 was checked several times during Operation Plumbbob, and no apparent discrepancies were discovered. Following completion of the field tests, a shock tube was used to dynamically calibrate the overpressure installation. The results of this test indicated no instrumentation discrepancies.

The time-of-shock-arrival correlation indicated good agreement between predicted and measured values.

4.2 ROTOR RESPONSE TO GUSTS

The six-degrees-of-freedom analysis of helicopter stability and control characteristics and maneuvering loads made possible a prediction of the helicopter flying qualities as well as applied aerodynamic loads during shock wave envelopment encountered during the tests. Discussion of structural-response data is reserved for another section of this report. Comparison of calculated data with flight-test data for Shots Priscilla, Diablo, and Kepler, indicate that the analysis will predict the rigid-body response time histories of normal load factor, rolling, pitching, and yawing accelerations with reasonable accuracy. It will also accurately predict maximum rotor-blade blapping for fuselage clearance considerations.

Calculated time histories of helicopter motion shown in Figure B.12 indicated that no flying-qualities problems developed for tail-on shots of the magnitude and orientation of either Shots Priscilla or Diablo. Presence of the autopilot and a gust input from the tail of the helicopter minimized both the flying qualities and loads conditions. Gust from the tail imparted a positive normal load factor and nose-down pitching moment at the first instant of time. The nose-down pitching moment was in a direction to relieve the normal load factor by causing a reduction of rotor angle of attack with time. In addition, the lift slope of the rotor was reduced by the reduction of helicopter air speed caused by the direction of the air-mass velocity.

In Channel 2 of Figure B.12c, the calculated time history of rotor-blade tip angle of attack for Shot Priscilla indicated that the retreating tip of the rotor blade did not attain a stalled condition. The stall condition is approached when the angle of attack of the retreating rotor blade, $\alpha_{(1.0)(270°)}$, reaches 10.6 degrees. Even if it did reach a value of 12 degrees or more, this local angle of attack rapidly reduces with time and could not cause any serious control-rod load problem with the blast from the tail unless the helicopter were already near stall for steady-state flight conditions.

In Channel 6 of Figure B.12a, the time history of rotor-blade flapping over the tail cone relative to the shaft indicated that initially the blades flap up and away from the tail cone and do not subsequently flap more than a degree closer to the tail cone than they were for the steady

flight preceding the bomb blast. It was apparent that rotor-blade flapping clearance was not a problem in the type of tail-on blast condition that existed in Shot Priscilla.

It is noted that in Channels 2, 3, and 4 of Figure 3.1, the autopilot helped to damp the longer period modes of rolling, pitching, and yawing accelerations rapidly. These oscillations would gradually build up with time if the autopilot were not used, provided that the pilot applied no corrective control. For this magnitude and character of disturbance, calculations show that even without the autopilot, several seconds could elapse without pilot control being applied without danger of loss of the helicopter.

According to Channel 2 of Figure B.12d, the autopilot did not introduce more than 0.028 radians of longitudinal cyclic pitch during Shot Priscilla. Since the autopilot has ± 0.044 radians of longitudinal cyclic pitch authority, it was adequate for stabilizing the helicopter following this tail-on blast.

It is emphasized that although no serious loads or flying-qualities problems arose in tail-on blasts of the severity of Shots Priscilla or Diablo, blasts from the side and particularly from the front could be quite severe. In the frontal blast, a nose-up applied pitching moment would accompany a positive normal load factor and the lift slope of the rotor would be increased by the increased air speed of the helicopter. The applied nose-up pitching moment would be in a direction to cause the helicopter to diverge in angle of attack and could lead to a flying-qualities problem as well as large normal-load-factor and angular accelerations.

4.3 STATIONARY-STAR LOAD CORRELATION

Correlation between predicted and measured values of stationary-star vibratory loads is presented in Tables 3.5 and 4.1 and is illustrated in Figure 1.3. Predicted values of the retreating-blade indicated tip speed were based on actual flight and atmospheric conditions at the time of shock arrival. All measured data were within the scatter of the experimental data from which the basic curve (Figure 1.3) was obtained. Due to this good correlation over a fairly wide range of conditions, it can be assumed that Figure 1.3 is valid for the range of operating conditions of the HSS-1.

4.4 STRUCTURAL CORRELATION

The method of structural analysis used to predict fuselage stresses resulting from blast effects was found to be accurate for predicting frame stresses. Although there were discrepancies between predicted and measured stringer stresses, this lack of correlation is believed to be due mainly to the inadequacy of the stringer instrumentation.

Strain-gage instrumentation of the critical structural area on the HSS-1 tail cone was originally intended for safety monitoring. As such, the number, orientation, and calibration of these gages, while perfectly adequate for their intended purpose, were marginal for an accurate representation of critical stress distributions. Coupled to this fact, Shots Owens and Kepler were both low-yield shots producing low accelerations, and stress-level changes were so small as to be practically indistinguishable from the normal noise and vibrations recorded.

An attempt to filter out some of these vibratory effects was made and was only partially successful. This method consisted of tracing off the vibratory trace recorded before the shot and determining whether it was cyclic or random by superimposing it on the same trace recorded after the shot effect. If the trace was cyclic and coincided, the tracing was aligned across the shot, matching time history before and after the shot. This tracing was then used as the zero baseline and disturbances were measured from it. This method yielded reasonable results for some of the accelerometer traces, but the stress traces were not periodic and had to be treated using the conventional method of means to filter out the high-frequency perturbations.

The tail-cone strain gages were calibrated with the aircraft on the ground. In order to check the base 1-g flight stress level, a calculation of loads incurred on the critical section was made both with the aircraft in 1-g steady flight and with it on the ground. By rationing the two sets

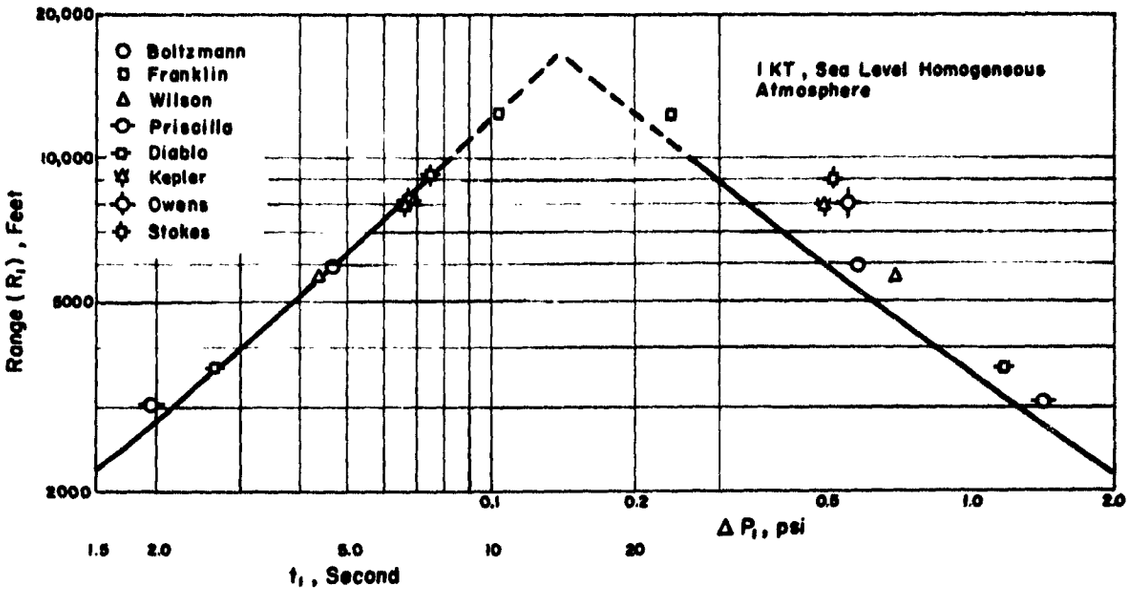

Figure 4.1 Correlation of calculated and measured effects parameters.

TABLE 4.1 STATIONARY-STAR LOAD CORRELATION

Shot	Density Altitude	Engine Speed	Average Indicated Tip Speed	Indicated Airspeed	Load Factor	Retreating-Blade Indicated Tip Speed *	Predicted Stationary-Star Load from Figure 1.4	Measured Stationary-Star Load
	feet	rpm	knots	knots	g	knots	± pounds	± pounds
Boltzmann	8,000	2,720	371	85	1.11	273	70	75
Franklin	10,200	2,660	350	73	1.05	270	70	110
Wilson	7,750	2,400	329	81	1.15	240	170	150
Priscilla	10,700	2,680	360	67	1.8	215	350	325
Diablo	12,950	2,800	362	69	1.80	218	320	350
Kepler	8,350	2,565	347	88	1.15	245	145	110
Owens	9,550	2,520	337	77	1.13	248	130	110
Stokes	10,000	2,545	336	67	1.14	251	130	150

* Retreating-Blade Indicated Tip Speed (knots) = Average Indicated Tip Speed (knots) − Airspeed (knots) ($\sqrt{\text{Load Factor}}$).

of loads, the base stress level was checked and in general, fair agreement was found with the calculations.

4.5 RADIANT EXPOSURE AND NUCLEAR RADIATION

All measured values of radiant exposure and nuclear radiation were too low in magnitude for accurate correlation. These effects were not critical for any HSS-1 positions. The measured values of these data are listed in Table 3.3.

Chapter 5
CONCLUSIONS

Comparisons of experimental data obtained during these HSS-1 tests (with predictions of helicopter response made possible by employing a six-degrees-of-freedom analysis of helicopter stability and control characteristics, and maneuvering loads) resulted in a high degree of confidence that these analytical methods may be employed to predict the helicopter flight behavior and aerodynamic loads caused by nuclear blast effects.

Comparisons of experimental fuselage stresses with analytical predictions confirm the accuracy of fuselage frame analysis but fail to prove or disprove the analysis of fuselage stringer stresses. Since it has been determined by analysis and substantiated by static tests that the tail-cone frames are more critical than the stringer, the confirmed frame-analysis methods permit establishment of the HSS-1 structural limitations due to the blast effects. These limitations were determined by analysis to be the helicopter design-limit load factor of 2.67 g and a limit overpressure of 0.71 psi.

From experimental data obtained during the HSS-1 participations it was found that the weapon-effects prediction methods employed permitted accurate prediction of time of shock arrival but resulted in unconservative prediction of peak overpressure behind the shock front.

The primary objective of the project was achieved to the extent that the critical blast limits of the HSS-1 helicopter were adequately defined for application to the problem of safe escape from underwater nuclear bursts. The determination of the delivery and escape capabilities of the helicopter for ASW nuclear weapons depends also upon the airblast and nuclear radiation characteristics associated with underwater explosions and the weapon fuzing characteristics. Treatment of these variables is considered beyond the scope of this project.

As may be anticipated from the employment of a manned helicopter during the tests of Project 5.1, few data were obtained which would be useful in substantiation of analytical lethal damage considerations. That part of the project's secondary objective related to experimental data for correlation in general problems of helicopter lethality for the Department of the Army was not satisfactorily met.

Appendix A
INSTRUMENTATION

A.1 RECORDING

Recording instrumentation installed in the HSS-1 consisted of two 36-channel Consolidated Electrodynamic Corporation Type 5-119 recording oscillographs, and a photopanel recorder. Photographic records were made of the normal flight instruments through the use of the photopanel recorder.

A.2 FUSELAGE STRESS MEASUREMENTS

Resistance strain gages were installed in the vicinity of the critical fuselage structure, as shown in Figure A.1, to measure the effect of overpressure on this structure. The fuselage strain gages were resistance-calibrated prior to and after each participation. Table A.1 is a summary of the fuselage strain gages.

A.3 OVERPRESSURE

A pressure transducer was installed on a special rack at the trailing edge of the tail pylon as shown in Item A-23 Figure A.2, to measure free-stream overpressure. Data obtained during the first shot participation was readable but, due to low frequency response of the static probe and low sensitivity of the galvanometer, a distorted time history of the overpressure pulse was obtained. Prior to participation in the second shot, this condition was corrected and satisfactory overpressure data were obtained for all following shots.

A differential pressure transducer was installed in the vicinity of the critical fuselage structure to record a time history of the outside/inside pressure in this area. The differential pressure transducer was located as shown in Item B-20, Figure A.2.

Both the overpressure and differential pressure transducers were calibrated in the Sikorsky instrument laboratory against a pressure standard. The manufacturer, type, and serial number are included in Table A.5.

A.4 GUST RESPONSE

Linear accelerometers were located at the center of gravity, oriented to record lateral, longitudinal, and vertical accelerations. Angular accelerometers were located at Station 236 to record pitch, roll, and yaw accelerations. Linear accelerometers were also located at the top of the tail pylon oriented to record vertical and lateral accelerations. All accelerometers were resistance calibrated prior to and immediately after each participation. An attitude gyro was calibrated prior to and after each participation by use of a precision 10-degree plane. Table A.2 is a summary of the gust response instrumentation.

A.5 MAIN ROTOR COMPONENT LOADS, STRESSES AND RELATIVE POSITIONS

Resistance strain gages were installed on the main rotor blades at 13 and 60 percent radius to record leading edge and normal bending stresses. Strain-gage bridges were also installed on the rotating and stationary star to record control loads. The rotating and stationary-star assemblies were statically calibrated at the Sikorsky test laboratory.

Baldwin thermometer element Type TB-14 gages were installed at 13 and 60 percent radius of the main rotor blades to record blade temperature rise and maximum temperature. All main rotor strain gages and thermometer elements were resistance-calibrated prior to and after each participation.

Potentiometer elements were installed to record main rotor blade, pitch, log, and flapping positions. Potentiometer elements were also installed to record main rotor control stick displacements. All potentiometer elements were calibrated by deflection of the control to its limits prior to and after each shot.

A magnetic pickup was located at the base of the main rotor shaft to indicate the azimuth position of the instrumented main rotor blades.

Table A.3 is a summary of the main rotor instrumentation, and Figure A.2 illustrates approximate locations of main rotor instrumentation.

A.6 TAIL ROTOR STRESSES AND RELATIVE POSITIONS

Resistance strain gages were installed on two tail rotor blades, to record tail rotor blade leading edge and normal bending stresses, as illustrated in Figure A.2.

Potentiometers were installed to measure tail rotor flapping and rudder pedal position. These potentiometers were calibrated by deflection of the tail rotor blades and rudder pedals to their limits prior to and after each shot.

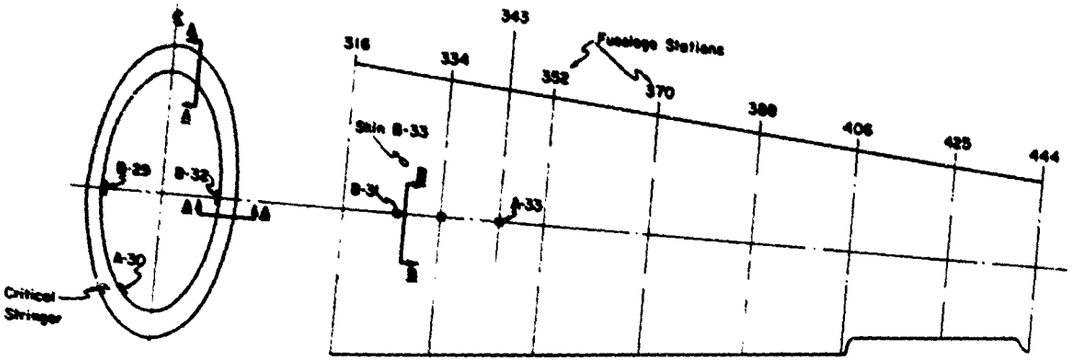

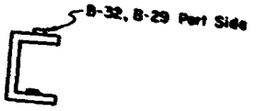

SECTION A-A

Location of Gages on Frame at F.S. 334

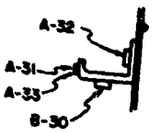

SECTION B-B

Location of Gages on Stringer at F.S. 334, 343

Figure A.1 Strain gage locations in aft fuselage, HSS-1 helicopter.

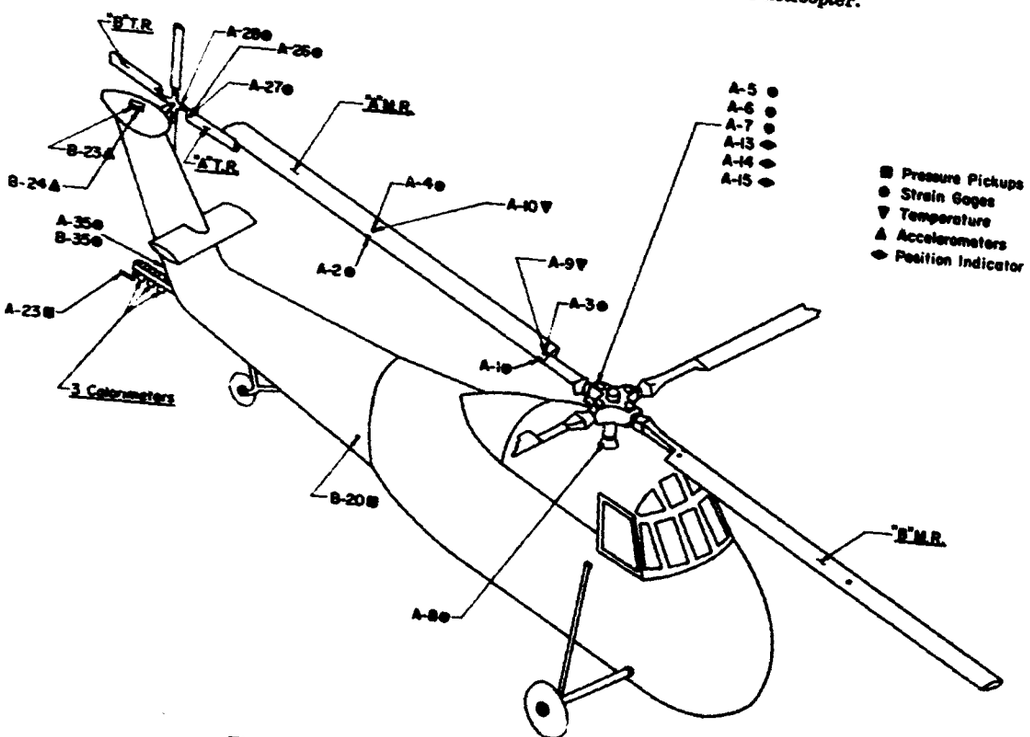

Figure A.2 Instrumentation locations, HSS-1 helicopter.

TABLE A.1 INSTRUMENTATION FOR FUSELAGE STRESS MEASUREMENTS

Instrument	Type	Measurement	Location	Type Galvanometer	Galvanometer Flat-Frequency Response	Recorder Channel
Strain Gage	A-13	Total Frame Stress	Station 334, Port Side	7-315	0-60	B-29
Strain Gage	A-13	Total Stringer Stress	Station 334, Starboard Side	7-315	0-60	B-30
Strain Gage	A-13	Total Stringer Stress	Station 326, Starboard Side	7-315	0-60	B-31
Strain Gage	A-13	Total Frame Stress	Station 334, Starboard Side	7-315	0-60	B-32
Strain Gage	A-13	Total Skin Stress	Station 326, Starboard Side	7-315	0-60	B-33
Strain Gage	A-13	Total Frame Stress	Station 334, Starboard Side	7-342	0-135	A-30
Strain Gage	A-?	Total Stringer Stress	Station 333, Starboard Side	7-342	0-135	A-31
Strain Gage	A-?	Total Stringer Stress	Station 333, Starboard Side	7-342	0-135	A-32
Strain Gage	A-?	Total Stringer Stress	Station 343, Starboard Side	7-342	0-135	A-33

TABLE A.2 ACCELERATION MEASUREMENTS

Manufacturer	Serial Number	Measurement	Location Fuselage Station	Type Galvanometer	Galvanometer Flat-Frequency Response	Recorder Channel
					cps	
Statham	228	Vertical Acceleration at Center of Gravity	137.6	325	0-11	A-17
Statham	227	Lateral Acceleration at Center of Gravity	137.6	325	0-11	A-18
Statham	1854	Longitudinal Acceleration at Center of Gravity	137.6	325	0-11	A-19
Statham	13	Pitch Acceleration (Angular)	236	325	0-11	A-20
Statham	16	Roll Acceleration (Angular)	236	325	0-11	A-21
Statham	14	Yaw Acceleration (Angular)	236	325	0-11	A-22
Statham	229	Vertical Acceleration at Center of Gravity	137.6	325	0-11	B-15
Statham	230	Lateral Acceleration at Center of Gravity	137.6	325	0-11	B-16
Statham	1191	Longitudinal Acceleration at Center of Gravity	137.6	325	0-11	B-17
Statham	1850	Vertical Acceleration Top of Tail Pylon	535	325	0-11	B-23
Statham	1853	Lateral Acceleration Top of Tail Pylon	535	325	0-11	B-24
Minneapolis-Honeywell	1736	Pitch Altitude Gyro	130	325	0-11	B-18
Minneapolis-Honeywell	1736	Roll Altitude Gyro	130	325	0-11	B-19

TABLE A.3 INSTRUMENTATION FOR MAIN ROTOR RESPONSES

Black and blue rotor blades are 180 degrees apart.

Instrument	Type	Measurement	Location	Type Galvanometer	Galvanometer Flat-Frequency Response	Recorder Channel
Strain gage	A-13	Leading-edge stress main rotor blade	13 pct radius (black blade)	7-315	0-60	B-1
Strain gage	A-13	Leading-edge stress main rotor blade	60 pct radius (black blade)	7-315	0-60	B-2
Strain gage	A-13	Normal bending stress main rotor blade	13 pct radius (black blade)	7-315	0-60	B-3
Strain gage	A-13	Normal bending stress main rotor blade	60 pct radius (black blade)	7-315	0-60	B-4
Strain gage	A-13	Push-rod load (black blade)		7-315	0-60	B-5
Strain gage	A-13	Longitudinal stationary-star load		7-315	0-60	B-6
Strain gage	A-13	Shaft bending stress main rotor		7-315	0-60	B-7
Strain gage	TB-14	Temperature main rotor blade	13 pct radius (black blade)	7-315	0-60	B-8
Strain gage	TB-14	Temperature main rotor blade	60 pct radius (black blade)	7-315	0-60	B-9
Potentiometer	400 Ω	Collective stick position		7-315	0-60	B-10
Potentiometer	400 Ω	Pitch angle θ main rotor blade	(black blade)	7-315	0-60	B-11
Potentiometer	400 Ω	Flapping angle β main rotor blade	(black blade)	7-315	0-60	B-12
Potentiometer	400 Ω	Lag angle γ main rotor blade	(black blade)	7-315	0-60	B-13
Coil		Position angle ψ main rotor blade	(black blade)	7-315	0-60	B-14
Strain gage	A-13	Leading-edge stress main rotor blade	13 pct radius (blue blade)	7-315	0-60	A-1
Strain gage	A-13	Leading-edge stress main rotor blade	60 pct radius (blue blade)	7-315	0-60	A-2
Strain gage	A-13	Normal bending stress main rotor blade	13 pct radius (blue blade)	7-315	0-60	A-3
Strain gage	A-13	Normal bending stress main rotor blade	60 pct radius (blue blade)	7-315	0-60	A-4
Strain gage	A-13	Push-rod load	(blue blade)	7-315	0-60	A-5
Strain gage	A-13	Right lateral stationary-star load		7-315	0-60	A-6
Strain gage	A-13	Left lateral stationary-star load		7-315	0-60	A-7
Strain gage	A-13	Shaft bending stress main rotor blade		7-315	0-60	A-8
Strain gage	TB-14	Temperature main rotor blade	13 pct radius (blue blade)	7-315	0-60	A-9
Strain gage	TB-14	Temperature main rotor blade	60 pct radius (blue blade)	7-315	0-60	A-10
Potentiometer	400 Ω	Lateral stick position		7-315	0-60	A-11
Potentiometer	400 Ω	Longitudinal stick position		7-315	0-60	A-12
Potentiometer	400 Ω	Pitch angle θ main rotor blade	(blue blade)	7-315	0-60	A-13
Potentiometer	400 Ω	Flapping angle β main rotor blade	(blue blade)	7-315	0-60	A-14
Potentiometer	400 Ω	Lag angle γ main rotor blade	(blue blade)	7-315	0-60	A-15
Coil	400 Ω	Position angle ψ main rotor blade	(blue blade)	7-315	0-60	A-16

TABLE A.4 INSTRUMENTATION FOR TAIL ROTOR

Black and red tail rotor blades 180 degrees apart.

Instrument	Type	Measurement	Location	Type Galvanometer	Galvanometer Flat-Frequency Response	Recorder Channel
Coil		Tail rotor position		?-342	0-135	B-22
Strain gage	A-13	Leading-edge stress tail rotor blade	(black blade)	?-342	0-135	B-25
Strain gage	A-13	Normal bending stress tail rotor blade	(black blade)	?-342	0-135	B-26
Potentiometer	400 Ω	Flapping angle β tail rotor blade	(black blade)	?-342	0-135	B-27
Potentiometer	400 Ω	Rudder pedal position		?-315	0-60	B-28
Strain gage	A-13	Leading-edge stress tail rotor blade	(red blade)	?-342	0-135	A-26
Strain gage	A-13	Normal bending stress tail rotor blade	(red blade)	?-342	0-135	A-27
Potentiometer	400 Ω	Flapping angle β tail rotor blade	(red blade)	?-342	0-135	A-28
Coil		Tail rotor position				A-29

TABLE A.5 MISCELLANEOUS INSTRUMENTATION

Manufacturer	Serial Number	Measurement	Location	Type Galvanometer	Galvanometer Flat-Frequency Response	Recorder Channel
Statham Type P.131	2272	Outside/inside pressure differential	Station 234, starboard side	?-342	0-135	B-20
Minneapolis-Honeywell	1	Calorimeter	Station 535	?-315	0-60	B-21
		Thermocouple	Station starboard side bottom tab	?-315	0-60	B-24
International Rectifier Corp.		Time "O" solar battery	Station 535	?-315	0-60	B-25
		Voltage Supply "B"	Station 136.7	?-315	0-60	B-26
		Camera synchronizer				Dynamic rotor.
Statham Type P36d-15A-350	2104	Overpressure	Station 535	?-350	0-30	A-23
NRDL	XX 21	Calorimeter	Station 535	?-315	0-60	A-24
Minneapolis-Honeywell	2	Calorimeter	Station 535	?-315	0-60	A-25
International Rectifier Corp.		Time "O" solar battery	Station 535	?-315	0-60	A-25
		Voltage Supply "A"	Station 136.7			A-26

Table A.4 is a summary of the tail rotor instrumentation.

A.7 MISCELLANEOUS

Calorimeters were installed on a special rack, attached to the trailing edge of the tail pylon, to measure indirect radiant exposure. Calorimeters were supplied and calibrated by the Naval Radiological Defense Laboratory (NRDL). A thermocouple was installed on the starboard side of the aircraft. This instrument was calibrated by NRDL personnel prior to and after each shot.

Solar batteries were installed, one of which was wired into each oscillograph, to indicate time of explosion. One channel on each oscillograph was used to monitor the instrumentation direct current voltage supply. The dynamic reference capability of each oscillograph was used to give indication on the oscillographs of each frame of photopanel data.

Table A.5 is a summary of the miscellaneous, overpressure, and differential pressure instrumentation.

Appendix B

EQUATIONS and METHODS of ANALYSIS for BLAST-WAVE RESPONSE of HSS-1 HELICOPTER

The purpose of the following sections is to present the equations and method of analysis of detailed motions of the HSS-1 helicopter in response to a nuclear blast wave. The basic helicopter relationships presented herein were modified or amplified in accordance with the discussion of Section 2.4.

B.1 WEAPON-EFFECTS PARAMETERS

In order to analyze the dynamic response of the helicopter to the blast wave from a nuclear detonation, it was necessary to predict the variation of significant blast-wave parameters with distance and time behind the shock front. Basic parameters such as particle velocity behind the shock front, density behind the shock front, dynamic pressure behind the shock front, and time of arrival of the shock front were predicted (using Figure 1.2) by the methods outlined in Section 1.3.

A schematic drawing of the orientation of the gust relative to the helicopter is shown in Figure B.1. This gust is resolved as shown in Figure B.2 into two simultaneous distrubances, an angle of attack disturbance, α_G, and a rotor tip-speed ratio disturbance, μ_i. By use of measured values of shock overpressure and the calculated gust velocity, useful graphical relationships of U' versus $\Delta p'$ as shown in Figure B.3 were obtained.

B.2 GUST RESPONSE EQUATIONS

B.2.1 List of Symbols.

a. Slope of curve of section lift coefficient against section angle of attack = 5.73/radian.

a', Longitudinal angle between the control axis and the rotor force resultant, radians.

a_i, Angle between the rotor-blade span axis and the tip-path plane, radians.

a_i, Longitudinal angle between a normal to the control axis and the tip-path plane, radians.

a_{i_s}, Longitudinal angle between a normal to the shaft axis and the tip-path plane, radians, ($a_{i_s} = a_i - B_{i_s}$).

A_{i_s}, Lateral angle between the control axis and shaft axis, radians.

b, Number of blades per rotor.

b', Lateral angle between the control axis and the rotor resultant force, radians.

b_i, Lateral angle between a normal to the control axis and the tip-path plane, radians.

b_{i_s}, Lateral angle between a normal to the shaft axis and the tip-path plane, ($b_{i_s} = b_i + A_{i_s}$).

B, Tip loss factor; blade elements outboard of BR are assumed to have profile drag but no lift.

B_{i_s}, Longitudinal angle between the control axis and the shaft axis, radians.

C, Rotor blade chord, feet.

C_{D_f}, Fuselage drag coefficient = $D/q\pi R^2$.

C_{L_f}, Fuselage lift coefficient = $L/q\pi R^2$.

C_{l_f}, Fuselage rolling moment coefficient = $L'_f/q\pi R^3$.

C_{l_h}, Rotor hub rolling moment coefficient = $L'_h/q\pi R^3$.

$C_{l_{ha}}$, Rotor hub rolling moment coefficient due to aerodynamic forces = $L'_{ha}/q\pi R^3$.

$C_{l_{hw}}$, Rotor hub rolling moment coefficient due to inertia forces = $L'_{hw}/q\pi R^3$.

C_{m_f}, Fuselage pitching moment coefficient = $M_f/q\pi R^3$.

C_{m_h}, Rotor hub pitching moment coefficient = $M_h/q\pi R^3$.

C_{n_f}, Fuselage yawing moment coefficient = $N_f/q\pi R^3$.

C_Q, Rotor shaft torque coefficient = $Q/\rho\pi R^2(\Omega R)^2 R$.

C_T, Main rotor thrust coefficient = $T/\rho\pi R^2(\Omega R)^2$.

C_{T_T}, Tail rotor thrust coefficient = $T_T/(\rho\pi R^2\Omega^2R^2)TR$.

C_Y, Rotor lateral force coefficient = $Y/\rho\pi R^2(\Omega R)^2$.

C_{Y_f}, Fuselage side force coefficient = $Y_f/q\pi R^2$.

D_f, Drag of fuselage (complete helicopter minus main rotor and tail rotor), lbs.

e, Rotor flapping hinge offset from center line of rotation, feet.

g, Acceleration due to gravity, ft/sec^2.

h, Vertical distance from main rotor hub to c.g. measured along vertical stability axis, feet.

$\bar{h}$, Longitudinal distances from main rotor hub to c.g. measured along a stability axis, feet.

$h_{TR,HT,VT}$, Vertical distance from center of rotation of tail, center of pressure of horizontal tail, or vertical tail to c.g. measured along a stability axis, feet.

H, Longitudinal component of rotor resultant force normal to the control axis, lbs.

i_s, Angle between a fuselage station line and the shaft axis, radians, positive for shaft tilted forward.

i_T, Angle of incidence of horizontal tail measured

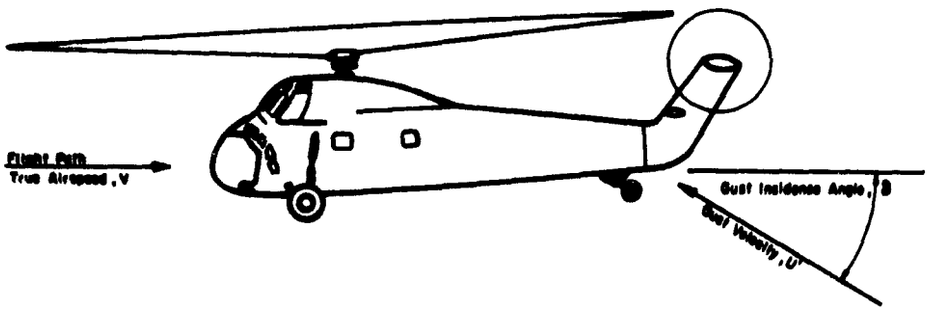

Figure B.1 Orientation of gust disturbance for the helicopter.

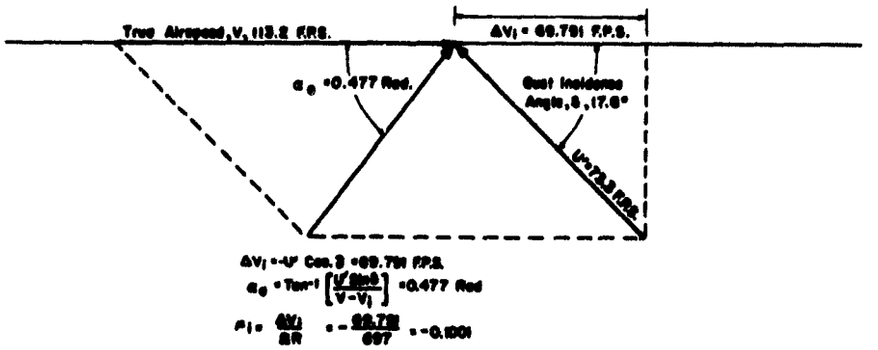

Figure B.2 Initial disturbance inputs for Shot Priscilla.

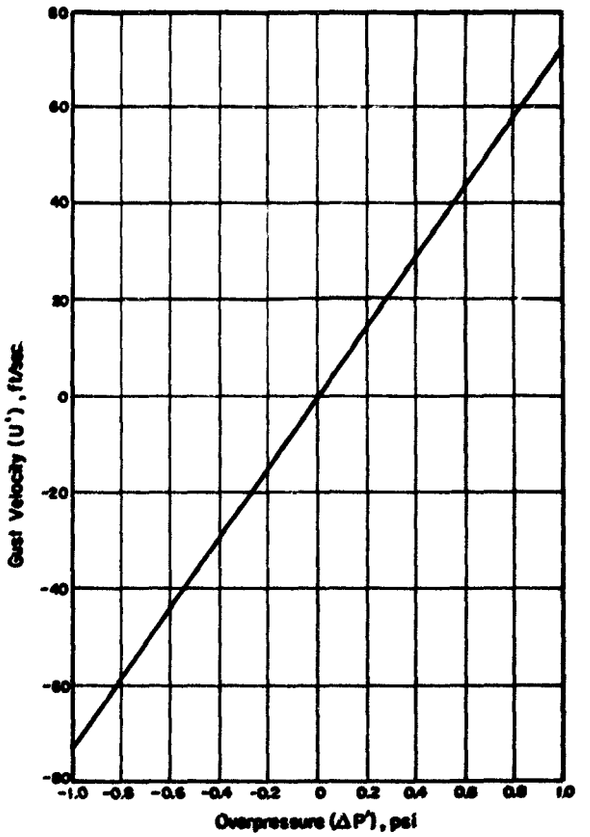

Figure B.3 Gust velocity as a function of overpressure.

from a fuselage waterline, radians, positive for leading edge up.

I_b, Moment of inertia of a rotor blade about the flapping hinge axis, slug-ft^2.

I_x, I_y, I_z, Moment of inertia of the helicopter about the longitudinal, lateral, and vertical axes, respectively, passing through the c.g., slug-ft^2.

K_i, Helicopter radius of gyration about the ith axis = $\sqrt{I_i g/w}$.

$l_{TR, HT, VT}$, Longitudinal distance from the center of rotation of the tail rotor, the center of pressure of the horizontal tail and vertical tail, respectively, from the c.g. measured along a stability axis, feet.

L, Rotor lift, lb.

L_f, Fuselage lift, lb.

L_h, Rotor hub rolling moment about a longitudinal axis through the rotor hub center, lb-ft.

L_{ha}, Rotor hub rolling moment due to aerodynamic forces, lb-ft.

L_{hw}, Rotor hub rolling moment due to inertia forces, lb-ft.

m, Mass parameter = $W/\rho bc\Omega R^2$.

m_b, Mass per unit span at the rotor blade, slugs/ft.

M_b, Mass moment of rotor blades about the flapping hinge = $\int_e^R m_b(r-e)dr$.

M_h, Rotor hub pitching moment about a lateral axis through the rotor hub center, lb-ft.

M_f, Fuselage aerodynamic pitching moment about a lateral axis passing through the c.g., lb-ft.

N, Yawing moment about the vertical axis, lb-ft.

N_f, Fuselage yawing moment about the vertical axis passing through the helicopter c.g., lb-ft.

q, Free stream dynamic pressure, lb/ft^2.

q_T, Dynamic pressure at the tail, lb/ft^2.

q_{Test}, Wind tunnel test dynamic pressure, lb/ft^2.

Q, Main rotor torque, lb-ft.

R, Rotor force resultant, lb; also rotor radius, ft.

S, Rotor disk area, πR^2, ft^2.

S.F., Scale factor of wind tunnel model.

t, Tabulated constant terms from Bailey's analysis, Reference 4.

T, Main rotor thrust, component of rotor resultant force taken along the control axis, lb.

T_T, Tail rotor thrust (acts along the axis of rotation), lb.

V, Velocity of the helicopter along the flight path, ft/sec.

V', Resultant wind velocity relative to the helicopter fuselage, ft/sec.

w, Weight parameter = $W/\rho bc\Omega^2R^3$.

W, Gross weight of the helicopter, lb.

Y, Lateral component of the rotor resultant force normal to the H force and the control axes, lb.

Y_f, Fuselage aerodynamic side force normal to the fuselage lift and drag forces, lb.

α, Rotor angle of attack, angle of attack of a normal to the control axis with respect to the flight path, radians.

α_f, Angle of attack of the fuselage with respect to the flight path.

$\alpha_{f_{local}}$, Angle of attack of the fuselage corrected for main rotor downwash.

α_s, Angle of attack of a normal to the shaft axis with respect to the flight path, radians.

α_l, Angle of attack of a normal to the control axis with respect to a lateral flight path, radians.

α_{l_s}, Angle of attack of a normal to the shaft axis with respect to a lateral flight path, radians.

β, Sideslip angle, angle between the longitudinal reference axis and the remote wind velocity, radians.

β_c, Angle between a normal to the control axis and the blade span axis, ($\beta_c = a_0 - a_1 \text{Cos}\psi - b_1 \text{ Sin } \psi$), radians.

β_s, Angle between a normal to the shaft axis and the blade span axis, radians.

γ, Mass constant of a rotor blade.

δ, Main rotor blade mean drag coefficient.

$\delta_0, \delta_1, \delta_2$, Constants in Bailey's quadratic equation for blade profile drag coefficient ($C_{d_0} = \delta_0 + \delta_1\alpha + \delta_2\alpha^2$).

ζ, Dimensionless rotor inertia force parameter, = (e M_b/I_b) + (e^2W_b/I_{bg}).

Θ_0, Rotor blade pitch angle measured at the cuff from a normal to the control axis, radians.

$\Theta_{.75}$, Rotor blade pitch angle measured at 75 percent blade radius from a normal to the control axis, radians.

Θ_T, Tail rotor blade pitch angle, radians.

Θ_F, Angle of inclination of the fuselage longitudinal axis from the horizon, ($\Theta_F = \alpha_F + \tau$), radians.

λ, Rotor blade tip inflow ratio = (V Sin$\alpha - \nu$)/ΩR.

μ, Rotor blade tip speed ratio = V/ΩR.

ν, Induced inflow velocity at rotor, ft/sec.

ρ, Density of air, slugs/ft^3.

σ, Rotor solidity ratio = bc/πR.

σ', Fuselage sidewash angle, radians.

τ, Longitudinal flight path angle, angle between longitudinal flight path and horizon, radians.

τ_l, Lateral flight path angle, angle between lateral flight path and horizon.

ϕ, Roll angle, the angle between the lateral reference axis and the horizon.

ψ, Angle of yaw - the angular displacement of the longitudinal axis before and after the disturbance, radians. (Also blade azimuth angle).

Ω, Rotor angular velocity, radians/sec.

ΩR, Rotor tip speed, ft/sec.

ϵ_w, Wing downwash angle, radians.

SUBSCRIPTS

f, W.B.T., Parameters of the wing body tail combination, the complete helicopter less the main and tail rotors.

M.F., Parameters pertaining to the main rotor. Unless otherwise specified, all rotor parameters

without a subscript are main rotor parameters.

t, TR, Parameters pertaining to the tail rotor.

V.T., Parameters pertaining to the vertical tail.

H.T., Parameters pertaining to the horizontal tail.

TEST, Wind tunnel test parameters.

S, A normal to the shaft axis is taken as the axis of reference.

B.2.2 System of Axes. The flight path stability axis system is used throughout. In hover, the flight path is coincident with the horizon. The x axis is positive forward and tangent to the flight path; the y axis is positive to the starboard and normal to the x axis; and the z axis is positive downward and normal to both the x and y axes. The positive direction of all angles are shown in Figures B.4, B.5, and B.6.

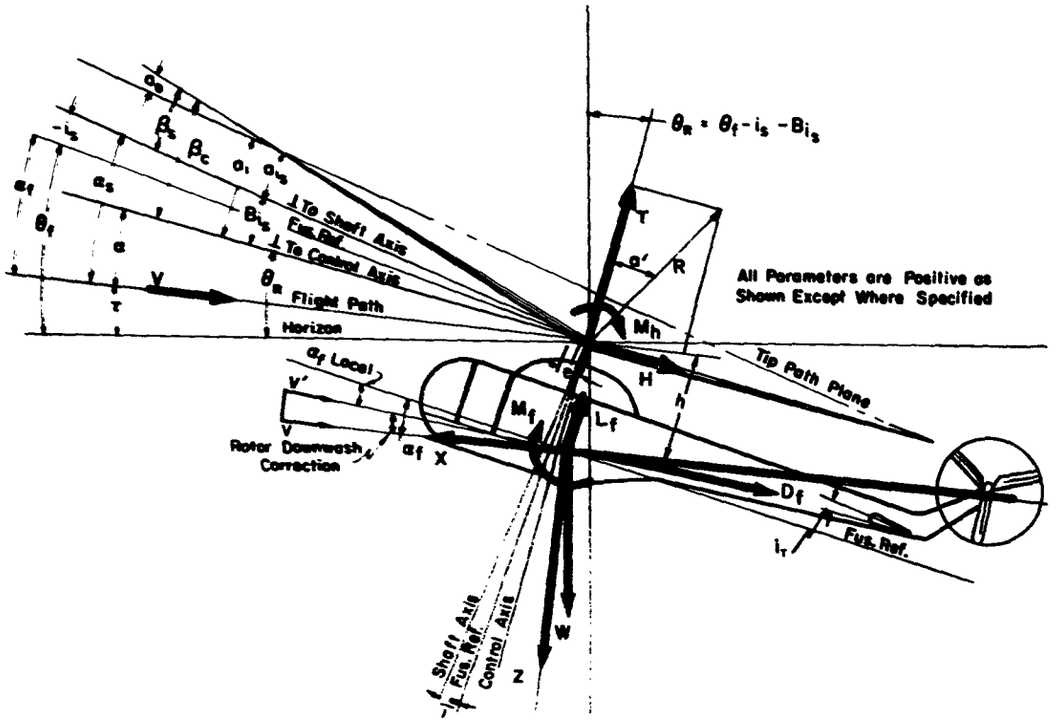

Figure B.4 Side view showing stability and control parameters.

B.2.3 Assumptions and Conditions. The linearized stability equations are subject to the following assumptions and conditions.

1. The helicopter is subjected to a disturbance which produces a motion of small oscillations.

2. Small control displacements occur for a short period of time during which only a small departure from the original steady-state flight path occurs.

3. The changes in forces and moments acting on or within the helicopter depend on displacements, velocities, and accelerations along and perpendicular to the flight-path axes in the case of forces, and about the helicopter center of gravity in the case of moments.

4. Since the deviation of each of the major variables from its equilibrium value is small, the differentials in the differential equations of motion are replaced with actual increments, and the partial derivatives of the helicopter forces and moments with respect to these variables and their first and second time derivatives are constant throughout the disturbed motion.

5. During the disturbance all of the major variables or their first and second derivatives with time are functions of time.

6. Rotor tip speed, ΩR, remains constant. (The tip speed ratio, μ, then varies only with the velocity along the flight path, V.)

7. Wind tunnel data and static trim data are available for the forward flight analysis.

8. Small angle assumptions are permissible:

$$\sin a = \tan a = a(\text{radians})$$
$$\cos a = 1$$

9. The second harmonic motion of the rotor blades

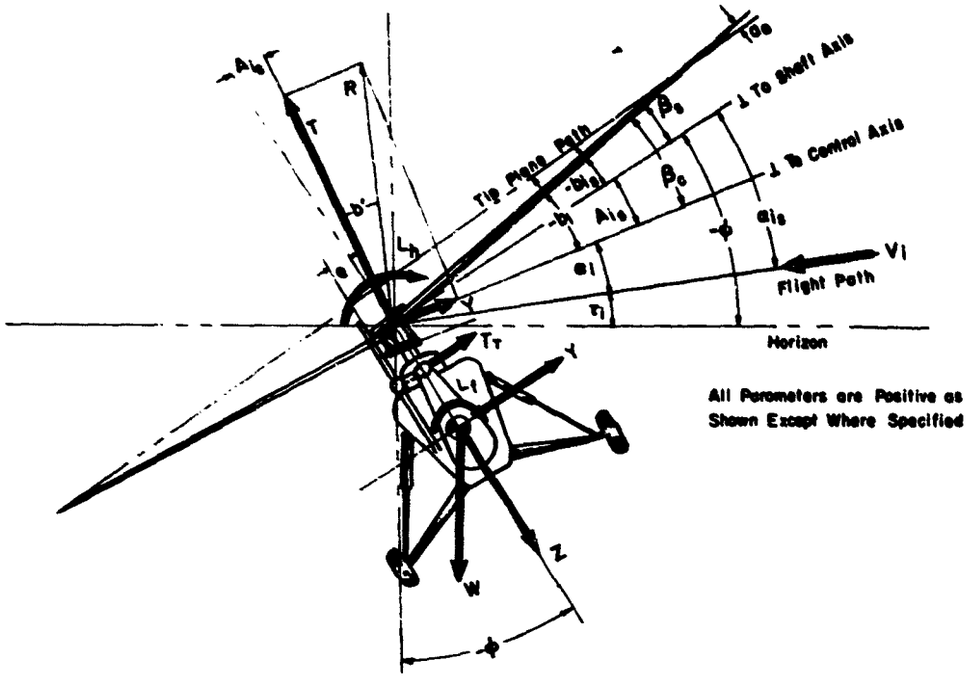

Figure B.5 Rear view showing stability and control parameters.

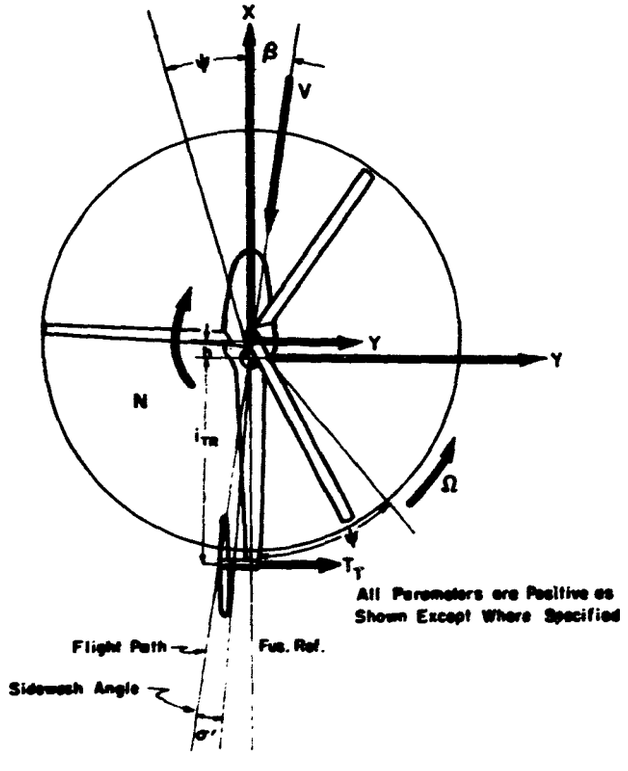

Figure B.6 Top view showing stability and control parameters.

and all higher harmonics are neglected.

10. Rotor blade motion about the lag hinge is neglected.

11. Compresaibility and stall effects are neglected.

12. The following helicopter physical quantities and parameters are taken as major variables:

α_f, Fuselage angle of attack relative to the flight path.

τ, Longitudinal flight path angle relative to the horizontal.

μ, μ_x, y, z, Rotor tip speed ratio.

β, Sideslip angle.

ϕ, Roll angle.

ψ, Yaw angle.

A_{1_S}, Lateral cyclic control.

B_{1_S}, Longitudinal cyclic control.

Θ_0, Main rotor collective control.

Θ_t, Tail rotor blade pitch angle control.

B.2.4 General Equations of Motion.

In The X Direction

$$-m\dot{u} - \frac{C_T}{\sigma}(\alpha'+\alpha) - \frac{\mu^2}{2\sigma}C_{L_f}\left(EK_f\frac{C_T}{2\mu^2}\right) + \frac{\mu^2}{2\sigma}C_{D_f} - \omega\tau = 0$$

In The Y Direction

$$-m\mu(\dot{\beta}+\dot{\psi}) + \left(\frac{C_T}{\sigma}\right)A_{1_S} + \frac{C_Y}{\sigma} + \omega\phi + \frac{C_{T_T}}{\sigma} + \frac{\mu^2}{2\sigma}C_{Y_f} = 0$$

In The Z Direction

$$m\mu\dot{\tau} + \frac{C_T}{\sigma}(\alpha'\alpha - 1) - \frac{\mu^2}{2\sigma}C_{L_f} + \frac{\mu^2}{2\sigma}C_{D_f}\left(EK_f\frac{C_T}{2\mu^2}\right) + \omega = 0$$

Rolling Moments

$$-(m\Omega)\left(\frac{K_x}{R}\right)^2\ddot{\phi} + \frac{C_T}{\sigma}\left(\frac{h}{R}\right)A_{1_S} + \frac{C_Y}{\sigma}\left(\frac{h}{R}\right) + \frac{C_{T_T}}{\sigma}\left(\frac{h_{T_R}}{R}\right) + \frac{\mu^2}{2\sigma}C_{l_n} + \frac{\mu^2}{2\sigma}C_{l_f} = 0$$

Pitching Moments

$$-\left(\frac{m}{\Omega}\right)\left(\frac{K_y}{R}\right)^2(\ddot{\alpha}_f + \ddot{\tau}) + \frac{C_T}{\sigma}\left[\frac{\bar{h}_s}{R}(1+\alpha'B_{1_S}) + \frac{h_s}{R}(\alpha' - \Theta_{1_S})\right] + \frac{\mu^2}{2\sigma}C_{m_n} + \frac{\mu^2}{2\sigma}C_{m_f} = 0$$

Yawing Moments

$$\frac{\partial}{\partial i_T}\left(\frac{\mu^2}{2\sigma}\right)C_{m_f}\left(\frac{\ell_{hT}}{V}\right)\left[\dot{\alpha}_f\left\{1 + \frac{EK_n\sigma}{2\mu^2}\left(\frac{\partial C_T}{\partial \alpha}\right) + \left(\frac{\partial f_{iw}}{\partial \alpha_f}\right)\left(\frac{\partial \alpha_f}{\partial \alpha}\right)\right\} + \dot{\tau}\right] = 0$$

$$-\left(\frac{m}{\Omega}\right)\left(\frac{K_z}{R}\right)^2\ddot{\psi} + \frac{C_T}{\sigma}\left(\frac{\bar{h}}{R}\right)A_{1_S} + \frac{C_Y}{\sigma}\left(\frac{\bar{h}}{R}\right) + \frac{C_Q}{\sigma} - \frac{C_T}{\sigma}\left(\frac{\ell_{T_R}}{R}\right) + \frac{\mu^2}{2\sigma}C_{n_f} = 0$$

WHERE: $\frac{C_T}{\sigma} = \frac{T}{\rho b c \Omega^2 R^3} = \frac{T}{\pi R^2 \rho (\Omega R)^2} \left(\frac{\pi R}{b c}\right)$

$\frac{C_Y}{\sigma} = \frac{Y}{\rho b c \Omega^2 R^3} = \frac{Y}{\pi R^2 \rho (\Omega R)^2} \left(\frac{\pi R}{b c}\right)$

$\frac{C_Q}{\sigma} = \frac{Q}{\rho b c \Omega^2 R^4} = \frac{Q}{\pi R^2 \rho (\Omega R)^2 R} \left(\frac{\pi R}{b c}\right)$

$\frac{C_{T_T}}{\sigma} = \frac{T_T}{(\rho b c \Omega^2 R^3)_{MR}}$

$w = \frac{W}{\rho b c \Omega^2 R^3}$

$m = \frac{W}{g \rho b c \Omega R^2}$

$\frac{\mu^2}{2\sigma} C_{Y_f} = \frac{Y_f}{\rho b c \Omega^2 R^3} = \frac{Y_f}{2\left[\frac{1}{2}\rho \pi R^2 (\mu \Omega R)^2\right]} \left(\frac{\pi R}{b c}\right) \mu^2$

$\frac{\mu^2}{2\sigma} C_{L_f} = \frac{L_f}{\rho b c \Omega^2 R^3}$

$\frac{\mu^2}{2\sigma} C_{D_f} = \frac{C_f}{\rho b c \Omega^2 R^3}$

$\frac{\mu^2}{2\sigma} C_{l_f} = \frac{L'_f}{\rho b c \Omega^2 R^4} = \frac{L_f}{2\left[\frac{1}{2}\rho \pi R^2 (\mu \Omega R^2) R\right]} \left(\frac{\pi R}{b c}\right) \mu^2$

$\frac{\mu^2}{2\sigma} C_{m_f} = \frac{M_f}{\rho b c \Omega^2 R^4}$

$\frac{\mu^2}{2\sigma} C_{H_f} = \frac{N_f}{\rho b c \Omega^2 R^4}$

$\frac{\mu^2}{2\sigma} C_{l_h} = \frac{L'_h}{\rho b c \Omega^2 R^4}$

$\frac{\mu^2}{2\sigma} C_{m_h} = \frac{M_h}{\rho b c \Omega^2 R^4}$

$K_x^2 = \frac{I_x g}{W}$

$K_Y^2 = \frac{I_Y g}{W}$

$$K_z^2 = \frac{I_z^2 g}{W^2}$$

$$\frac{C_Y}{\sigma} = -\frac{\alpha}{2}\Big[\frac{6\mu\beta}{2a} - \frac{3}{4}b_1\lambda + \frac{3}{2}a_0\mu\lambda - \frac{1}{4}a_1b_1\mu + \frac{1}{4}b_1^2\mu\beta + a_0a_1\mu^2 - a_0b_1\mu^2\beta - \frac{1}{6}a_0a_1 + \frac{1}{4}a_0^2\mu\beta + \theta_0\Big(\frac{3}{4}\mu a_0 - \frac{1}{3}b_1 - \frac{1}{2}a_1\mu^2\beta - \frac{1}{2}\lambda\mu\beta - \frac{1}{2}\mu^2b_1\Big) + \theta_1\Big[\frac{1}{2}a_0\mu - \frac{1}{4}b_1 - \frac{1}{4}a_1\mu^2\beta - \frac{1}{4}\lambda\mu\beta - \frac{1}{4}b_1\mu^2\Big)\Big]$$

$$\frac{\mu^2}{2\sigma}C_{l_a} = \frac{\rho a}{2\gamma}(b_1 + A_{15}) - \frac{\alpha\rho}{2\gamma}\Big\{\frac{1}{6}\Big[\frac{\dot{\theta}}{2\alpha} - a_1\Big]\Big[1 - \Big(\frac{\rho}{R}\Big)^3\Big] + \frac{1}{2}\Big[\theta_{1.5}(\lambda\gamma + \mu) + \frac{1}{2}a_0\mu\beta\Big]\Big[1 - \Big(\frac{\rho}{R}\Big)^2\Big] + \frac{1}{2}\Big[\alpha\lambda^2 + \frac{1}{4}\mu^2a_1 + \mu\lambda - \frac{\mu^2\beta b_1}{2} - \frac{1}{4}\mu A_{15}\lambda\Big]\Big[1 - \Big(\frac{\rho}{R}\Big)\Big]\Big\}$$

$$\frac{\mu^2}{2\sigma}C_{m_a} = \frac{\rho a}{2\gamma}(a_1 - B_{15}) - \frac{\alpha\rho}{2\gamma}\Big\{\frac{2}{5}\Big[b_1 + \frac{2\dot{\alpha}}{2\alpha} + \frac{\dot{\alpha}}{2\alpha}\Big]\Big[1 - \Big(\frac{\rho}{R}\Big)^5\Big] - \mu a_0\Big[1 - \Big(\frac{\rho}{R}\Big)^4\Big] + \frac{1}{2}\mu^2b_1\Big[1 - \Big(\frac{\rho}{R}\Big)\Big]\Big\}$$

$$a_0 = \frac{\gamma}{2}\Big[\frac{\theta_0}{4}(1+\mu^2) + \theta_1\Big(\frac{1}{3} + \frac{\mu^2}{4}\Big) + \frac{\lambda}{3}\Big] - \frac{M_{bg}}{I_0\Omega^2}$$

$$a_1 = \frac{4\Big[\frac{1}{3}a_0\mu\beta + \frac{1}{2}\lambda\mu + \frac{2}{3}\mu\theta_0 + \frac{1}{2}\mu\theta_1\Big]}{\Big(1 - \frac{\mu^2}{2}\Big)}$$

$$b_1 = \frac{4\Big[\frac{2}{3}\theta_0\mu\beta + \frac{1}{2}\theta_1\mu\beta + \frac{1}{2}\lambda\mu\beta - \frac{1}{3}\mu a_0\Big]}{\Big(1 + \frac{\mu^2}{2}\Big)}$$

B.2.5 Linearized Stability Equations.

$$F_{x\dot{\zeta}}\dot{\zeta} + F_{x\zeta}\zeta + F_{x\dot{\alpha}_c}\dot{\alpha}_c + F_{x\alpha_c}\alpha_c + F_{x\dot{\theta}}\dot{\theta} + F_{x\dot{\mu}}\dot{\mu} + F_{x\mu}\mu + F_{xB_{1s}}B_{1s} + F_{x\theta_0}\theta_0 = 0$$

$$F_{y\dot{\zeta}}\dot{\zeta} + F_{y\dot{\alpha}_c}\dot{\alpha}_c + F_{y\dot{\beta}}\dot{\beta} + F_{y\beta}\beta + F_{y\dot{\phi}}\dot{\phi} + F_{y\phi}\phi + F_{y\dot{\psi}}\dot{\psi} + F_{y\mu}\mu + F_{y\alpha_c}\alpha_c + F_{yA_{1s}}A_{1s} + F_{yB_{1s}}B_{1s} + F_{y\theta_0}\theta_0 + F_{y\theta_t}\theta_t = 0$$

$$F_{\dot{z}}\dot{\zeta}+F_{\dot{\alpha}_f}\dot{\alpha}_f+F_{\alpha_f}\alpha_f+F_{\mu}\mu+F_{B_{1s}}B_{1s}+F_{\dot{\phi}}\dot{\phi}+F_{\theta_o}\theta_o=0$$

$$L_{\dot{\zeta}}\dot{\zeta}+L_{\dot{\alpha}_f}\dot{\alpha}_f+L_{\alpha_f}\alpha_f+L_{\beta}\beta+L_{\ddot{\phi}}\ddot{\phi}+L_{\dot{\phi}}\dot{\phi}+L_{\dot{\psi}}\dot{\psi}+L_{\mu}\mu+L_{A_{1s}}A_{1s}+$$

$$L_{B_{1s}}B_{1s}+L_{\theta_o}\theta_o+L_{\theta_t}\theta_t=0$$

$$M_{\ddot{\zeta}}\ddot{\zeta}+M_{\dot{\zeta}}\dot{\zeta}+M_{\dot{\alpha}_f}\dot{\alpha}_f+M_{\alpha_f}\alpha_f+M_{\beta}\beta+M_{\dot{\phi}}\dot{\phi}+M_{\mu}\mu+$$

$$M_{B_{1s}}B_{1s}+M_{\theta_o}\theta_o=0$$

$$N_{\ddot{\zeta}}\ddot{\zeta}+N_{\dot{\alpha}}\dot{\alpha}+N_{\alpha_f}\alpha_f+N_{\beta}\beta+N_{\dot{\phi}}\dot{\phi}+N_{\ddot{\psi}}\ddot{\psi}+N_{\dot{\psi}}\dot{\psi}+N_{\mu}\mu+$$

$$N_{A_{1s}}A_{1s}+N_{B_{1s}}B_{1s}+N_{\theta_o}\theta_o+\theta_t N_{\theta_t}=0$$

B.2.6 Helicopter Derivatives.

1. $F_{x\dot{\gamma}} = -\frac{C_T}{\sigma}\left(\frac{\partial \alpha'}{\partial \dot{\gamma}}\right)$

2. $F_{x\gamma} = -\omega$

3. $F_{x\dot{\alpha}_f} = F_{x\dot{\gamma}}$

4. $F_{\alpha_f} = -\left[\alpha'+\alpha+\left(\frac{EK_y}{4}\right)C_{L_f}\right]\left(\frac{\partial C_T}{\partial \alpha}\right)-\frac{C_T}{\sigma}\left[1+\frac{\partial \alpha'}{\partial \alpha}+\frac{EK_y}{4}\left(\frac{\partial C_{L_f}}{\partial \alpha_f}\right)_{L_f=0}\left(\frac{\partial \alpha_f}{\partial \alpha}\right)\right]-\frac{\mu}{2\sigma}\left(\frac{\partial C_{L_f}}{\partial \alpha_f}\right)_{L_f=0}\left(\frac{\partial \alpha_f}{\partial \alpha}\right)$

5. $F_{x\dot{\phi}} = -\frac{1}{\Omega R}F_{x\theta_{1s}}$

6. $F_{x\dot{\mu}} = -m$

7. $F_{x\mu} = -\left[\alpha'+\alpha+\left(\frac{EK_y}{4}\right)C_{L_f}\right]\left(\frac{\partial C_T}{\partial \mu}\right)-\frac{C_T}{\sigma}\left(\frac{\partial \alpha'}{\partial \mu}\right)-\frac{\mu}{\sigma}C_{\alpha_f}$

8. $F_{x\theta_{1s}} = +\left[\alpha'+\alpha+\left(\frac{EK_y}{4}\right)C_{L_f}\right]\left(\frac{\partial C_T}{\partial \alpha}\right)+\frac{C_T}{\sigma}\left(\frac{\partial \alpha'}{\partial \theta_{1s}}\right)$

9. $F_{x\theta_o} = -\left[\alpha'+\alpha\right]\left(\frac{\partial C_T}{\partial \theta_o}\right)-\frac{C_T}{\sigma}\left(\frac{\partial \alpha'}{\partial \theta_o}\right)$

10. $F_{y\dot{\gamma}} = \frac{\sigma}{2}\left[a_o\left(\mu^2-\frac{1}{6}\right)-\frac{\mu}{4}b_1\right]\left(\frac{\partial a_1}{\partial \dot{\gamma}}\right)-\frac{C_T}{\sigma}\left(\frac{1}{\Omega R}\right)$

11. $F_{Y\dot{\alpha}_t} = F_{Y\dot{v}}$

12. $F_{Y\alpha_t} = A_{1S}\left(\frac{\partial C_T}{\partial \alpha}\right) + \left(\frac{\partial C_N}{\partial \alpha}\right)$

13. $F_{Y\dot{\phi}} = F_{Y\dot{\phi}_{M.R.}} + F_{Y\beta_{M.R.}}\left(\frac{\bar{h}}{V}\right) + F_{Y\beta_{T.R.}}\left(\frac{h_{TR}}{V}\right) + \left[\left(\frac{h_{VT}}{V}\right)_{\alpha_t=0}\right] F_{Y\beta_{V.T.}}$

14. $F_{Y\phi} = \omega$

15. $F_{Y\dot{\beta}} = -m\mu$

16. $F_{Y\beta} = F_{Y\beta_{M.R.}} + F_{Y\beta_{T.R.}}\left(1 - \frac{\partial \sigma'}{\partial \beta}\right) + F_{Y\beta_{W.B.T.}}$

17. $F_{Y\dot{v}} = -m\mu - F_{Y\beta_{T.R.}}\left(\frac{l_{TR}}{V}\right) - \left(\frac{l_{VT}}{V}\right)\frac{F_{Y\beta_{VT}}}{\left(1 - \frac{\partial \sigma'}{\partial \beta}\right)}$

18. $F_{Y\mu} = \frac{\partial C_Y}{\partial \mu} + \frac{\partial \frac{C_{T_T}}{\sigma}}{\partial \mu} + \frac{\partial \frac{C_T}{\sigma}}{\partial \mu} A_{1S}$

19. $F_{Y\alpha_t} = \frac{C_T}{\sigma}$

20. $F_{Y\theta_{1S}} = -F_{Y\alpha_t}$

21. $F_{Y\theta_c} = A_{1S}\left(\frac{\partial \frac{C_T}{\sigma}}{\partial \theta_c}\right) + \frac{\partial \frac{C_T}{\sigma}}{\partial \theta_c}$

22. $F_{Y\theta_c} = \frac{\partial}{\partial \theta_c}\left(\frac{C_T}{\sigma}\right)_{T.R.}\left(\frac{\sigma_{TR}}{\sigma}\right)\left(\frac{\alpha_{TR}}{\alpha}\right)^2\left(\frac{R_{TR}}{R}\right)^4$

23. $F_{Z\dot{\gamma}} = m\mu + \left(\frac{C_T}{\sigma}\right)\left(\frac{\partial \alpha'}{\partial \gamma}\right)\alpha$

24. $F_{Z\dot{\alpha}_t} = \left(\frac{C_T}{\sigma}\right)\left(\frac{\partial \alpha'}{\partial \alpha}\right)\alpha$

25. $F_{Z\alpha_t} = \left[\alpha'\alpha + \left(\frac{EK_f}{4}\right)C_{D_f} - 1\right]\left(\frac{\partial \frac{C_T}{\sigma}}{\partial \alpha}\right) + \frac{C_T}{\sigma}\left[\alpha' + \left(\frac{\partial \alpha'}{\partial \gamma}\right)\alpha + \frac{EK_f}{4}\left(\frac{\partial C_{D_f}}{\partial \alpha_f}\right)_{\alpha=0}\left(\frac{\partial \alpha_f}{\partial \alpha}\right)\right] - \frac{\mu^2}{2\sigma}\left(\frac{\partial C_{L_f}}{\partial \alpha_f}\right)_{\alpha=0}\left(\frac{\partial \alpha_f}{\partial \alpha}\right)$

26. $F_{Z\dot{\theta}} = -\left(\frac{1}{2\mu}\right)F_{Z\theta_{1S}}$

27. $F_{Z\mu} = \left[\alpha'\alpha + \left(\frac{EK_f}{4}\right)C_{D_f} - 1\right]\left(\frac{\partial \frac{C_T}{\sigma}}{\partial \mu}\right) + \frac{C_T}{\sigma}\left(\frac{\partial \alpha'}{\partial \mu}\right)\alpha - \frac{C_{L_f}}{\sigma}\mu$

28. $F_{Z\theta_{1S}} = -\left[\alpha'\alpha + \left(\frac{EK_f}{4}\right)C_{D_f} - 1\right]\left(\frac{\partial \frac{C_T}{\sigma}}{\partial \alpha}\right) - \frac{C_T}{\sigma}\left(\alpha' + \frac{\partial \alpha'}{\partial \alpha}\alpha\right)$

29. $F_{Z\theta_0} = (a'_{ik}-1)\left(\frac{h_{TR}}{R}\right) + \left(\frac{h_{TR}}{R}\right)\left(\frac{\partial C_{mac}}{\partial \alpha_f}\right)\alpha$

30. $L\dot{\gamma} = -\frac{\rho V S b}{2g}\left(\frac{1}{I}\right) - \frac{\rho V^2}{2I}\left[-\frac{1}{2}\left(\frac{\rho V S b}{2I}\right)\left[1-\left(\frac{h_{TR}}{R}\right)^2\right] + \frac{\mu^2}{\sigma}\left(\frac{\rho V S b}{2I}\right)\left[1-\left(\frac{h_{TR}}{R}\right)\right] + \left(\frac{h_{TR}}{R}\right) F_{Y\gamma}\right]$

31. $L\dot{\alpha}_f = L\dot{\gamma}$

32. $L\alpha_f = \frac{\rho V S b}{2I}\left(\frac{\partial b_1}{\partial \alpha}\right) + \frac{\partial C_{mac}}{\partial \alpha} + \left(\frac{h_{TR}}{R}\right) F_{Y\alpha_f}$

33. $L\ddot{\phi} = -\left(\frac{m}{\Omega}\right)\left(\frac{K_x}{R}\right)^2$

34. $L\dot{\phi} = F_{Y\dot{\phi}_{mac}}\left(\frac{h_{TR}}{R}\right) + \frac{\partial C_{mac}}{\partial \phi} + F_{Y\beta_{mac}}\left(\frac{h_{mac}}{VR}\right) + \left(\frac{h_{VT}}{R}\right)\left[\left(\frac{h_{VT}}{V}\right) - \left(\frac{h_{VT}}{V}\right)_{\alpha_f=0}\right] F_{Y\beta_{VT}}$

35. $L\dot{\psi} = -F_{Y\dot{\beta}_{mac}}\left(\frac{h_{mac}}{R}\right)\left(\frac{h_{TR}}{V}\right) - \frac{F_{Y\beta_{VT}}}{\left(1-\frac{\partial \sigma'}{\partial \beta}\right)}\left(\frac{h_{VT}}{R}\right)\left(\frac{h_{VT}}{V}\right)$

36. $L\beta = L\beta_{mac} + F_{Y\dot{\beta}_{mac}}\left(\frac{h}{R}\right) + F_{Y\beta_{VT}}\left(\frac{h_{VT}}{R}\right) + F_{Y\beta_{T.R.}}\left(\frac{h_{T.R.}}{R}\right)$

37. $L\mu = \frac{\rho V S b}{2I}\left(\frac{\partial b_1}{\partial \mu}\right) + \frac{\partial}{\partial \mu}\left(\frac{\partial C_{mac}}{\partial \alpha}\right) + \left(\frac{h_{TR}}{R}\right)\left[\frac{\partial C_{Y_T}}{\partial \mu} + A_{1s}\left(\frac{\partial C_{Y_T}}{\partial \mu}\right)\right] + \left(\frac{h_{TR}}{R}\right)\frac{\partial C_{Y_T}}{\partial \mu}$

38. $L A_{1s} = \frac{C_T}{\sigma}\left(\frac{h}{R}\right) + \frac{\rho a}{2\gamma}$

39. $L B_{1s} = -L\alpha_f$

40. $L\theta_0 = F_{Y\theta_0}\left(\frac{h}{R}\right) + \frac{\rho a_0}{2\gamma}\left(\frac{\partial b_1}{\partial \theta_0}\right) + \frac{\partial C_{L_{max}}}{\partial \theta_0}$

41. $L\theta_t = F_{Y\theta_t}\left(\frac{h_{TR}}{R}\right)$

42. $M\ddot{\gamma} = -\left(\frac{m}{\Omega}\right)\left(\frac{K_y}{R}\right)^2$

43. $M\dot{\gamma} = \left(\frac{C_T}{\sigma}\right)\left(\frac{\partial \alpha'}{\partial \tau}\right)\left(\frac{h_s}{R} + \frac{h_s}{R} B_{1s}\right) + \frac{\rho a}{2\gamma}\left(\frac{\partial \alpha}{\partial \tau}\right) - \frac{a c}{\pi \Omega R}\left[1-\left(\frac{e}{R}\right)^2\right]$
$+ \frac{\mu\omega^2}{2\sigma}\left(\frac{\rho_{SL} I}{\nu}\right)\left(\frac{\partial C_{mof}}{\partial i_T}\right)_{\mu=0}$

44. $M\ddot{\alpha}_f = M\ddot{\gamma}$

45. $M\dot{\alpha}_f = M\dot{\gamma} + \frac{\mu^2}{2\sigma}\left(\frac{\rho_{SL} I}{\nu}\right)\left(\frac{\partial C_{mof}}{\partial i_T}\right)_{\mu=0}\left[\left(\frac{\partial \epsilon_{tw}}{\partial \alpha_f}\right)_{\mu=0}\left(\frac{\partial \alpha_f}{\partial \alpha}\right) + \frac{E k_y \sigma}{2\mu^2}\left(\frac{\partial \frac{C_T}{\sigma}}{\partial \alpha}\right)\right]$

46. $$M_{\alpha_f} = \frac{\partial C_T}{\partial \alpha}\left[\frac{\bar{h}_s}{R} - \frac{h_s}{R}B_{1s} + \alpha'\left(\frac{h_s}{R} + \frac{\bar{h}_s}{R}B_{1s}\right)\right] + \frac{C_T}{\sigma}\left(\frac{\partial \alpha'}{\partial \alpha}\right)\left(\frac{h_s}{R} + \frac{\bar{h}_s}{R}B_{1s}\right)$$
$$+ \frac{\gamma_a}{2\gamma}\left(\frac{\partial a_1}{\partial \alpha}\right) + \frac{1}{\rho b c \Omega^2 R^4}\left(\frac{\partial M_f}{\partial \alpha_f}\right)_{\alpha_c}\left(\frac{\partial \alpha_f}{\partial \alpha}\right)$$

47. $$M_{\dot{\phi}} = -\left(\frac{1}{\Omega}\right) M_{B_{1s}}$$

48. $$M_\beta = + \frac{\gamma_a}{2\gamma}\left(\frac{\partial a_1}{\partial \beta}\right)$$

49. $$M_\mu = \frac{\partial C_T}{\partial \mu}\left[\frac{\bar{h}_s}{R} - \frac{h_s}{R}B_{1s} + \alpha'\left(\frac{h_s}{R} + \frac{\bar{h}_s}{R}B_{1s}\right)\right] + \frac{C_T}{\sigma}\left(\frac{\partial \alpha'}{\partial \mu}\right)\left(\frac{h_s}{R} + \frac{\bar{h}_s}{R}B_{1s}\right) + \frac{\gamma_a}{2\gamma}\left(\frac{\partial a_1}{\partial \mu}\right) + \frac{\mu}{\sigma}C_{m_f}$$

50. $$M_{B_{1s}} = -\frac{C_T}{\sigma}\left(\frac{h_s}{R} - \alpha'\frac{\bar{h}_s}{R}\right) - \frac{\gamma_a}{2\gamma}\left(1 + \frac{\partial a_1}{\partial \alpha'}\right) + \frac{\partial C_T}{\partial \alpha}\left[\frac{h_s}{R}B_{1s} - \frac{\bar{h}_s}{R} - \alpha'\left(\frac{h_s}{R} + \frac{\bar{h}_s}{R}B_{1s}\right)\right]$$
$$- \frac{C_T}{\sigma}\left(\frac{\partial \alpha'}{\partial \alpha}\right)\left(\frac{h_s}{R} + \frac{\bar{h}_s}{R}B_{1s}\right)$$

51. $$M_{\theta_0} = \frac{\partial C_T}{\partial \theta_0}\left[\frac{\bar{h}_s}{R} - \frac{h_s}{R}B_{1s} + \alpha'\left(\frac{h_s}{R} + \frac{\bar{h}_s}{R}B_{1s}\right)\right] + \frac{C_T}{\sigma}\left(\frac{\partial \alpha'}{\partial \theta_0}\right)\left(\frac{h_s}{R} + \frac{\bar{h}_s}{R}B_{1s}\right) + \frac{\partial}{\partial \theta_0}\left(\frac{\mu^2}{2\sigma}C_{m_n}\right)$$

52. $$N_{\dot{\gamma}} = \left(\frac{\bar{h}}{R}\right) F_{y\dot{\gamma}}$$

53. $$N_{\dot{\alpha}_f} = N_{\dot{\gamma}}$$

54. $$N_{\alpha_f} = \left(\frac{\bar{h}}{R}\right)F_{y\alpha_f} + \mu\left(\frac{\partial C_T}{\partial \alpha}\right)\left[\frac{P}{L} + \frac{C_T}{\sigma}\left(\frac{\partial \frac{P}{L}}{\partial \frac{C_T}{\sigma}}\right)_\mu\right]$$

55. $$N_{\dot{\phi}} = F_{y\dot{\phi}_{TR}}\left(\frac{\bar{h}}{R}\right) - F_{y\beta_{TR}}\left(\frac{l_{TR}}{V}\right)\left(\frac{h_{TR}}{R}\right) - \left(\frac{l_{VT}}{R}\right)\left[\left(\frac{h_{VT}}{V}\right) - \left(\frac{h_{VT}}{V}\right)_{\lambda_{TPP}=0}\right] F_{y\beta_{VT}}$$

56. $$N_\beta = F_{y\beta_{TR}}\left(\frac{\bar{h}}{R}\right) - F_{y\beta_{TR}}\left(\frac{l_{TR}}{R}\right) + N_{\beta_{WBT}}$$

57. $$N_{\dot{\psi}} = -\left(\frac{m}{\Omega}\right)\left(\frac{K_z}{R}\right)^2$$

58. $$N_{\dot{\psi}} = F_{y\beta_{TR}}\left(\frac{l_{T.R.}}{V}\right)\left(\frac{l_{TR}}{R}\right) + \frac{F_{y\beta_{VT}}}{\left(1 - \frac{\partial \sigma}{\partial \rho}\right)}\left(\frac{l_{VT}}{R}\right)\left(\frac{l_{VT}}{V}\right)$$

59. $N_{\mu} = \left(\frac{\bar{h}}{R}\right)\left[\left(\frac{\partial C_X}{\partial \mu}\right) + A_{13}\left(\frac{\partial C_T}{\partial \mu}\right)\right] + \left(\frac{l_{TR}}{R}\right)\frac{\partial C_{T_R}}{\partial \mu} + \frac{P}{L}\left(\frac{C_T}{\sigma}\right) +$

$\mu\left(\frac{C_T}{\sigma}\right)\left[\left(\frac{\partial P}{\partial \mu}\right)_{C_T} + \left(\frac{\partial P}{\partial \frac{C_T}{\sigma}}\right)_{\mu}\left(\frac{\partial \frac{C_T}{\sigma}}{\partial \mu}\right)\right] + \mu\left(\frac{P}{L}\right)\left(\frac{\partial C_T}{\partial \mu}\right)$

60. $N_{A_{13}} = \frac{C_T}{\sigma}\left(\frac{\bar{h}}{R}\right)$

61. $N_{B_{13}} = N_{\alpha_f}$

62. $N_{\theta_0} = F_{y\theta_0}\left(\frac{\bar{h}}{R}\right) + \frac{\partial C_m}{\partial \theta_0}$

63. $N_{\theta_1} = -F_{y\theta_1}\left(\frac{l_{TR}}{R}\right)$

B.2.7 Rotor Derivatives.

1. $\frac{\partial \alpha'}{\partial \hat{\alpha}} = \frac{\partial \alpha'}{\partial \hat{\tau}} = \frac{-16/\gamma^4}{\gamma\Omega\left(1 - \frac{\mu^2}{2\Omega^2}\right)}\left[\frac{3}{2}\left(1 - \frac{.29\,\theta_{.75}}{C_T/\sigma}\right)\right]$

2. $\frac{\partial \frac{C_T}{\sigma}}{\partial \alpha} = \frac{t_{\alpha_1}\mu}{\cos^2\alpha\left(\frac{2}{a} + \frac{t_{\alpha_1}}{2\mu}\sigma\hat{C}\right)}$

3. $\left(\frac{\partial \alpha'}{\partial \frac{C_T}{\sigma}}\right)_{\mu}$ = Evaluated From Fig. 3, Ref. 2

4. $\frac{\partial \alpha'}{\partial \alpha} = \left(\frac{\partial \alpha'}{\partial \frac{C_T}{\sigma}}\right)_{\mu}\left(\frac{\partial \frac{C_T}{\sigma}}{\partial \alpha}\right)$

5. $\left(\frac{\partial \frac{C_T}{\sigma}}{\partial \mu}\right)_{\frac{\bar{h}}{R}} = \left\{\frac{a}{2}\left[\lambda\frac{\partial t_{\alpha_1}}{\partial \mu} + \theta_{.75}\frac{\partial t_{\alpha_1}}{\partial \mu}\right] + \left[\frac{t_{\alpha_1}\mu}{\frac{2}{a} + \frac{t_{\alpha_1}}{2\mu}\sigma\hat{C}}\right]\left[\frac{\lambda}{\mu^2} + \frac{C_T}{3\mu^3\sqrt{1+\left(\frac{\lambda}{\mu}\right)^2}} + \frac{C_T}{2\mu^3\left[\sqrt{1+\left(\frac{\lambda}{\mu}\right)^2}\right]^{3/2}}\right]\right\}_{\frac{\bar{h}}{R}}$

6. $\left(\frac{\partial \alpha'}{\partial \mu}\right)_{\frac{C_T}{\sigma}}$ = Evaluated From Fig 3, Ref. 2

7. $$\frac{\partial \alpha'}{\partial \mu} = \left(\frac{\partial \alpha'}{\partial \mu}\right)_{\frac{C_T}{\sigma}} + \left(\frac{\partial \alpha'}{\partial \frac{C_T}{\sigma}}\right)\left(\frac{\partial \frac{C_T}{\sigma}}{\partial \mu}\right)$$

8. $$\frac{\partial \frac{C_T}{\sigma}}{\partial \theta_0} = \left[\frac{t_{3,2}}{\frac{2}{a} + \frac{t_{3,1}}{2\mu}\sigma\bar{c}'}\right]$$

9. $$\left(\frac{\partial \alpha'}{\partial \theta_0}\right)_{\frac{C_T}{\sigma}} = \text{Evaluated From Fig 3, Ref 2}$$

10. $$\frac{\partial \alpha'}{\partial \theta_0} = \left(\frac{\partial \alpha'}{\partial \theta_0}\right)_{\frac{C_T}{\sigma}} + \left(\frac{\partial \alpha'}{\partial \frac{C_T}{\sigma}}\right)_{\mu}\left(\frac{\partial \frac{C_T}{\sigma}}{\partial \theta_0}\right)$$

11. $$\frac{\partial a_1}{\partial \dot{\alpha}} = \frac{\partial a_1}{\partial \dot{\tau}} = \frac{-16/B^4}{\gamma\Omega\left(1 - \frac{\mu^2}{2B^2}\right)}$$

12. $$\frac{\partial \lambda}{\partial \alpha} = \frac{1}{\frac{1}{\mu} + \frac{\sigma}{2\mu^2}\left(\frac{a}{2} t_{3,1}\right)}$$

13. $$\frac{\partial a_0}{\partial \alpha} = \gamma t_{1,1}\left(\frac{\partial \lambda}{\partial \alpha}\right)$$

14. $$\frac{\partial a_1}{\partial \alpha} = t_{1,4}\left(\frac{\partial \lambda}{\partial \alpha}\right)$$

15. $$\frac{\partial b_1}{\partial \alpha} = \gamma t_{1,7}\left(\frac{\partial \lambda}{\partial \alpha}\right)$$

16. $$\frac{\partial C_T}{\partial \alpha} = -\frac{a}{2}\left\{a_0\left[\frac{3}{4}\mu\left(\frac{\partial a_0}{\partial \alpha}\right) - \left(\frac{1}{3} + \frac{\mu^2}{2}\right)\frac{\partial b_1}{\partial \alpha}\right] + \theta_0\left[\frac{\mu}{2}\left(\frac{\partial a_0}{\partial \alpha}\right) - \frac{1}{4}\left(\frac{\partial b_1}{\partial \alpha}\right)(4\mu^2)\right]\right.$$
$$+\left[\frac{3}{2}\lambda\mu + a_1\left(\mu^2 - \frac{1}{6}\right)\right]\left(\frac{\partial a_0}{\partial \alpha}\right) + \left[\left(\mu^2 - \frac{1}{6}\right)a_0 - \frac{1}{4}\mu b_1\right]\left(\frac{\partial a_1}{\partial \alpha}\right)$$
$$\left.-\left[\frac{3}{4}\lambda + \frac{1}{4}\mu a_1\right]\left(\frac{\partial b_1}{\partial \alpha}\right) + \left[\frac{3}{2}\mu a_0 - \frac{3}{4}b_1\right]\left(\frac{\partial \lambda}{\partial \alpha}\right)\right\}$$

17. $$\frac{\partial b_1}{\partial \theta} = \frac{-16/B^4}{\gamma\Omega\left(1 + \frac{\mu^2}{2B^2}\right)}$$

18. $F_{Y\dot{\phi}_{NR}} = \left(\frac{C_T}{\sigma}\right)\left(\frac{\partial b_1}{\partial \phi}\right)\left(\frac{3}{2}\right)\left(1 - \frac{.29\,\theta_{.75}}{C_T/\sigma}\right)$

19. $\frac{\partial a_1}{\partial \beta} = \frac{4\mu a_0}{3\left(1 - \frac{\mu^2}{2}\right)}$

20. $\frac{\partial b_1}{\partial \beta} = \frac{-4\mu\left(\frac{1}{2} + \frac{2}{3}\theta_0 + \frac{1}{2}\theta_1\right)}{\left(1 + \frac{\mu^2}{2}\right)}$

21. $F_{Y\beta_{NR}} = -\frac{\sigma}{2}\Big\{\frac{\delta\mu}{2a} - a_2 b_1\mu^2 + \frac{1}{4}\mu a_0^2 + \frac{1}{4}\mu b_1^2 - \theta_0\left[\frac{1}{2}a_1\mu^2 + \frac{1}{2}\lambda\mu\right]$
$- \theta_1\left(\frac{1}{4}a_1\mu^2 + \frac{1}{4}\lambda\mu\right) + \left[a_1\left(\mu^2 - \frac{1}{2}\right) - \frac{1}{4}\mu b_1\right]\left(\frac{\partial a_1}{\partial \beta}\right)$
$- \left[\left(\frac{1}{3} + \frac{1}{2}\mu^2\right)\theta_0 + \left(1 + \mu^2\right)\frac{\theta_1}{4} + \frac{3}{4}\lambda + \frac{1}{4}a_1\mu\right]\left(\frac{\partial b_1}{\partial \beta}\right)$

22. $\frac{\partial}{\partial \alpha}\left(\frac{C_T}{\sigma}\right)_{TR} = \left[\frac{\mu^2 a\left(t_{3,1} - \frac{1}{4}\mu^2\right)}{2\mu + \frac{\sigma a}{2}\left(t_{3,1} - \frac{1}{4}\mu^2\right)}\right]_{TR}$

23. $F_{Y\beta_{TR}} = -\frac{\partial}{\partial x}\left(\frac{C_T}{\sigma}\right)_{TR}\left(\frac{\sigma_{TR}}{\sigma}\right)\left(\frac{\Omega_{TR}}{\Omega}\right)^2\left(\frac{R_{TR}}{R}\right)^4\left(1 - \frac{\partial \sigma'}{\partial \beta}\right)$

24. $\frac{\partial \lambda}{\partial \mu} = \alpha - \frac{\sigma}{2\mu^2}\left[\mu\left(\frac{\partial C_T}{\partial \mu}\right) - C_T\right]$

25. $\frac{\partial \alpha_0}{\partial \mu} = \gamma\left[t_{1,1}\left(\frac{\partial \lambda}{\partial \mu}\right) + \left(\frac{\partial t_{1,1}}{\partial \mu}\right) + \theta_0\left(\frac{\partial t_{1,2}}{\partial \mu}\right) + \theta_1\left(\frac{\partial t_{1,3}}{\partial \mu}\right)\right]$

26. $\frac{\partial a_1}{\partial \mu} = t_{1,4}\left(\frac{\partial \lambda}{\partial \mu}\right) + \lambda\left(\frac{\partial t_{1,4}}{\partial \mu}\right) + \theta_0\left(\frac{\partial t_{1,5}}{\partial \mu}\right) + \theta_1\left(\frac{\partial t_{1,6}}{\partial \mu}\right)$

27. $\frac{\partial b_1}{\partial \mu} = \gamma\left[t_{1,7}\left(\frac{\partial \lambda}{\partial \mu}\right) + \lambda\left(\frac{\partial t_{1,7}}{\partial \mu}\right) + \theta_0\left(\frac{\partial t_{1,8}}{\partial \mu}\right) + \theta_1\left(\frac{\partial t_{1,9}}{\partial \mu}\right)\right]$

28. $\frac{\partial C_X}{\partial \mu} = -\frac{\sigma}{2}\Big\{\theta_0\left[\frac{3}{4}a_0 + \frac{3}{4}\mu\left(\frac{\partial a_0}{\partial \mu}\right) - \mu b_1 - \left(\frac{1}{3} + \frac{1}{2}\mu^2\right)\left(\frac{\partial b_1}{\partial \mu}\right)\right]$
$+ \theta_1\left[\frac{1}{2}a_0 + \frac{1}{2}\mu\left(\frac{\partial a_0}{\partial \mu}\right) - \frac{1}{2}\mu b_1 - \frac{1}{4}\left(1 + \mu^2\right)\left(\frac{\partial b_1}{\partial \mu}\right)\right] + \left[\frac{3}{2}\lambda\mu\right.$
$\left. + \left(\mu^2 - \frac{1}{6}\right)a_1\right]\left(\frac{\partial a_0}{\partial \mu}\right) + \left[-\frac{1}{4}b_1\mu + a_0\left(\mu^2 - \frac{1}{6}\right)\right]\left(\frac{\partial a_1}{\partial \mu}\right) + \left[-\frac{3}{4}\lambda - \frac{1}{4}\mu a_0\right]\left(\frac{\partial a_1}{\partial \mu}\right)$
$+ \left[\frac{3}{2}\mu a_0 - \frac{3}{4}b_1\right]\frac{\partial \lambda}{\partial \mu} + \left[\frac{3}{2}\lambda + \mu a_1\right]a_0 + \left[\mu a_0 - \frac{1}{4}b_1\right]a_1\Big\}$

29. $\frac{\partial}{\partial \mu}\left(\frac{C_T}{\sigma a}\right) = \left[\frac{\partial}{\partial \mu}\left(\frac{\mu}{6}\right)\right]_{TR}\left(\frac{\sigma_{TR}}{\sigma}\right)\left(\frac{a_{TR}}{a}\right)^2\left(\frac{R_{TR}}{R}\right)^4\left(\frac{\mu_{TR}}{\mu}\right)$

30. $\frac{\partial \lambda}{\partial \theta_0} = -\frac{\alpha}{2\mu}\left(\frac{\partial \mu}{\partial \theta_0}\right)$

31. $\frac{\partial \theta_1}{\partial \theta_0} = \gamma\left[t_{1,1}\left(\frac{\partial \lambda}{\partial \theta_0}\right) + t_{1,2}\right]$

32. $\frac{\partial \theta_2}{\partial \theta_0} = t_{1,4}\left(\frac{\partial \lambda}{\partial \theta_0}\right) + t_{1,5}$

33. $\frac{\partial \theta_3}{\partial \theta_0} = \gamma\left[t_{1,7}\left(\frac{\partial \lambda}{\partial \theta_0}\right) + t_{1,8}\right]$

34. $\frac{\partial C_{ST}}{\partial \theta_0} = -\frac{\alpha}{2}\left\{\frac{3}{4}\mu a_0 - \left(\frac{1}{3} + \frac{\mu^2}{12}\right)b_1 + \theta_0\left[\frac{3}{4}\mu\left(\frac{\partial a_0}{\partial \theta_0}\right) - \left(\frac{1}{3} + \frac{\mu^2}{12}\right)\left(\frac{\partial b_1}{\partial \theta_0}\right)\right]\right.$
$+\theta_1\left[\frac{3}{4}\left(\frac{\partial a_0}{\partial \theta_0}\right) - \frac{1}{4}(1-\mu^2)\left(\frac{\partial b_1}{\partial \theta_0}\right)\right] + \left[\frac{3}{4}a_0\mu - \frac{3}{4}b_1\right]\left(\frac{\partial \lambda}{\partial \theta_0}\right)$
$+\left[\frac{3}{4}\mu\lambda + a_1\left(\mu^2 - \frac{1}{6}\right)\right]\left(\frac{\partial \mu}{\partial \theta_0}\right) + \left[a_0\left(\mu^2 - \frac{1}{6}\right) - \frac{1}{4}\mu b_1\right]\left(\frac{\partial \mu}{\partial \theta_0}\right)$
$\left.+\left[-\frac{3}{4}\lambda - \frac{1}{4}a_1\mu\right]\left(\frac{\partial b_1}{\partial \theta_0}\right)\right\}$

35. $\frac{\partial}{\partial \theta_0}\left(\frac{C_T}{\sigma}\right)_{\theta_0} = \left[\frac{\frac{\partial C_{LA}}{\partial \theta_0} - \frac{C_{LA}}{\sigma}\left(\frac{\partial \sigma}{\partial \theta_0}\right)}{\sigma\left(\frac{\partial C_{LA}}{\partial \alpha} + \frac{\partial C_{DA}}{\partial \alpha} - \frac{C_{DA}}{\sigma}\right)}\right]_{\theta_0, \alpha}$

36. $\frac{\partial C_{LA}}{\partial \alpha} = -\frac{\sigma\alpha}{2\alpha}\left\{-\frac{1}{6}\left(\frac{\partial a_0}{\partial \alpha}\right)\left[1-\left(\frac{\alpha}{\alpha_s}\right)^3\right] + \frac{1}{2}\theta_{0.75}\left[\lambda + \alpha\left(\frac{\partial \lambda}{\partial \alpha}\right)\right]\left[1-\left(\frac{\alpha}{\alpha_s}\right)^2\right]\right.$
$\left.+\frac{1}{2}\left[2\lambda\alpha\left(\frac{\partial \lambda}{\partial \alpha}\right) + \lambda^2 + \frac{1}{4}\mu^2\left(\frac{\partial a_0}{\partial \alpha}\right) + \mu\left(\frac{\partial \mu}{\partial \alpha}\right)\right]\left[1-\left(\frac{\alpha}{\alpha_s}\right)\right]\right\}$

37. $\frac{\partial C_{LA}}{\partial \phi} = \frac{\sigma a_0}{2\alpha}\left[\frac{\partial b_1}{\partial \phi} + \frac{\partial b_1}{\partial \beta}\left(\frac{h}{r}\right)\right] - \frac{\sigma a_0}{2\alpha}\left\{\frac{1}{8}\mu^2\left(\frac{\partial a_0}{\partial \beta}\right)\left(\frac{h}{r}\right)\left[1-\left(\frac{\alpha}{\alpha_s}\right)\right]\right.$
$\left.-\frac{1}{6}\left(\frac{\partial a_0}{\partial \beta}\right)\left(\frac{h}{r}\right)\left[1-\left(\frac{\alpha}{\alpha_s}\right)^3\right] + \frac{1}{2}\mu\left(\frac{h}{r}\right)\left[1-\left(\frac{\alpha}{\alpha_s}\right)^2\right]\right\}$

38. $L/R_{HUB} = \frac{\sigma a_0}{2\alpha}\left(\frac{\partial b_1}{\partial \beta}\right) - \frac{\sigma a_0}{2\alpha}\left\{\frac{1}{8}\mu^2\left(\frac{\partial a_0}{\partial \beta}\right)\left[1-\left(\frac{\alpha}{\alpha_s}\right)\right] - \frac{1}{6}\left(\frac{\partial a_0}{\partial \beta}\right)\left[1-\left(\frac{\alpha}{\alpha_s}\right)^3\right]\right\}$

39. $\frac{\partial C_{LA}}{\partial \mu} = -\frac{\sigma a_0}{2\alpha}\left\{-\frac{1}{6}\left(\frac{\partial a_0}{\partial \mu}\right)\left[1-\left(\frac{\alpha}{\alpha_s}\right)^3\right] + \frac{\sigma\alpha_s}{2}\left[1+\alpha\left(\frac{\partial \lambda}{\partial \mu}\right)\right]\left[1-\left(\frac{\alpha}{\alpha_s}\right)^2\right]\right.$
$\left.+\frac{1}{2}\left[2\lambda\alpha\left(\frac{\partial \lambda}{\partial \mu}\right) + \frac{1}{2}a_1\mu + \frac{1}{4}\mu^2\left(\frac{\partial a_0}{\partial \mu}\right) + \mu\left(\frac{\partial \lambda}{\partial \mu}\right) + \lambda\right]\left[1-\left(\frac{\alpha}{\alpha_s}\right)\right]\right\}$

40. $\frac{\partial C_{LA}}{\partial \theta_0} = \frac{\sigma a_0}{2\alpha}\left\{-\frac{1}{6}\left(\frac{\partial a_0}{\partial \theta_0}\right)\left[1-\left(\frac{\alpha}{\alpha_s}\right)^3\right] + \frac{1}{2}\left[\lambda\alpha + \mu + \theta_{0.75}\alpha\left(\frac{\partial \lambda}{\partial \theta_0}\right)\right]\left[1-\left(\frac{\alpha}{\alpha_s}\right)^2\right]\right.$
$\left.+\frac{1}{2}\left[2\lambda\alpha\left(\frac{\partial \lambda}{\partial \theta_0}\right) + \frac{1}{4}\mu^2\left(\frac{\partial a_0}{\partial \theta_0}\right) + \mu\left(\frac{\partial \mu}{\partial \theta_0}\right)\right]\left[1-\left(\frac{\alpha}{\alpha_s}\right)\right]\right\}$

41. $\left\{\frac{\partial(\xi)}{\partial\left(\frac{\alpha}{\alpha_s}\right)}\right\}_{\mu}$ = EVALUATED FROM FIG. 3 OF REF. 2

42. $\left\{\frac{\partial(\xi)}{\partial \mu}\right\}_{\frac{\alpha}{\alpha_s}}$ = EVALUATED FROM FIG. 3 OF REF. 2

43. $\frac{\partial C_{QP}}{\partial \theta_0} = \frac{1}{2}\left\{\left(\frac{\partial \lambda}{\partial \theta_0}\right)\left[-\alpha\left(2t_{4,1}\lambda + t_{4,2}\theta_0 + t_{4,3}\theta_1\right) + \delta_1 t_{5,2}\right.\right.$
$\left.+\delta_2\left(2t_{5,5}\lambda + t_{5,6}\theta_0 + t_{5,7}\theta_1\right)\right] - \alpha\left(t_{4,2}\lambda + 2t_{4,4}\theta_0\right.$
$\left.\left.+t_{4,5}\theta_1\right) + \delta_1\left(t_{5,3}\right) + \delta_2\left(t_{5,6}\lambda + 2t_{5,8}\theta_0 + t_{5,9}\theta_1\right)\right\}$

$$11.\ \frac{\partial}{\partial\alpha_s}\left(\frac{M^2}{\rho\Omega^2}C_{M_s}\right) = \frac{\rho_0}{2\sigma}\frac{\partial a_0}{\partial\alpha_s} - \frac{a_0}{8R}\left\{\frac{3}{2}\left(\frac{\partial a_1}{\partial\alpha_s}\right)\left[1-\left(\frac{r_c}{R}\right)^4\right] - \mu\left(\frac{\partial a_2}{\partial\alpha_s}\right)\left[1-\left(\frac{r_c}{R}\right)^3\right] + \frac{1}{2}\mu^2\left(\frac{\partial a_1}{\partial\alpha_s}\right)\left[1-\left(\frac{r_c}{R}\right)\right]\right\}$$

B.2.8 Fuselage Aerodynamic Derivatives.

$$1.\ \frac{\partial\alpha_f}{\partial\alpha} = \left(1 - \frac{EK_f\sigma}{2\mu^2}\frac{\partial C_{L_f}}{\partial\alpha}\right)$$

$$2.\ \alpha_{f_{\substack{LOCAL\\(DES)}}} = \alpha_{f_{TRIM}} - EK_{FUS.}\,i_{HR.} = \alpha_{f_{TRIM}} - 0.5\left(\frac{W - L_{f_{TRIM}}}{q_\infty \pi R^2}\right)57.3$$

$$3.\ i_{T_{LOCAL}} = i_{T_{FIXED}} - (EK_{TAIL} - EK_{FUS.})\,i_{HR} = i_{T_{FIXED}} - (1.8 - 0.5)\,i_{HR}$$

$$4.\ \frac{\partial C_{L_f}}{\partial\alpha_{f_{LOC.}}} = \left(\frac{\partial L_f}{\partial\alpha_f}\right)_{\substack{MODEL\\ \alpha_{f_{LOC.}},\, i_{T_{LOC.}}}} \times \left(\frac{1}{S.F.}\right)^2 \times \left(\frac{q}{q_{TEST}}\right) \times \frac{57.3}{\frac{\rho}{2}(\pi R^2)(\mu\Omega R)^2}$$

$$5.\ \frac{\partial C_{D_f}}{\partial\alpha_{f_{LOC.}}} = \left(\frac{\partial D_f}{\partial\alpha_f}\right)_{\substack{MODEL\\ \alpha_{f_{LOC}},\, i_{T_{LOC}}}} \times \left(\frac{1}{S.F.}\right)^2 \left(\frac{q}{q_{TEST}}\right) \times \frac{57.3}{\frac{\rho}{2}(\pi R^2)(\mu\Omega R)^2}$$

$$6.\ \frac{\partial M_f}{\partial\alpha_{f_{LOC}}} = \left(\frac{\partial M_f}{\partial\alpha_f}\right)_{\substack{MODEL\\ \alpha_{f_{LOC}},\, i_{T_{LOC}}}} \times \left(\frac{1}{S.F.}\right)^3 \times \left(\frac{q}{q_{TEST}}\right) \times 57.3$$

$$7.\ \frac{\partial C_{M_f}}{\partial\, i_{T_{LOC.}}} = \left(\frac{\partial M_f}{\partial\, i_T}\right)_{\substack{MODEL\\ \alpha_{f_{LOC}},\, i_{T_{LOC}}}} \times \left(\frac{1}{S.F.}\right)^3 \times \left(\frac{q}{q_{TEST}}\right) \times \frac{57.3}{\frac{\rho}{2}(\pi R^2)(\mu\Omega R)^2 R}$$

$$8.\ \frac{\partial M_f}{\partial\mu} = \frac{2}{\mu}(M_f)_{\substack{MODEL\\ \alpha_{f_{LOC}},\, i_{T_{LOC}}}} \left(\frac{1}{S.F.}\right)^3 \times \left(\frac{q}{q_{TEST}}\right)$$

$$9.\ C_{L_f} = \left[(L_f)_{\substack{MODEL\\ \alpha_{f_{LOC}},\, i_{T_{LOC}}}} \times \left(\frac{1}{S.F.}\right)^2 \times \left(\frac{q}{q_{TEST}}\right)\right] \Big/ \left[\frac{\rho}{2}(\pi R^2)(\mu\Omega R)^2\right]$$

$$10.\ C_{D_f} = \left\{\left[\frac{(D_f)_{\substack{MODEL\\ \alpha_{f_{LOC}},\, i_{T_{LOC}}}}}{(S.F.)^2\, q_{TEST}} + \text{PAR. DRAG CORR.}\right] q_\infty\right\} \Big/ \left[\frac{\rho}{2}(\pi R^2)(\mu\Omega R)^2\right]$$

$$11.\ C_{M_f} = \left[(M_f)_{\substack{MODEL\\ \alpha_{f_{LOC}},\, i_{T_{LOC}}}} \times \left(\frac{1}{S.F.}\right)^3 \times \left(\frac{q}{q_{TEST}}\right)\right] \Big/ \left[\frac{\rho}{2}(\pi R^2)(\mu\Omega R)^2 R\right]$$

12. $F_{Y\beta_{M.R.}} = \left[\left(\frac{\partial Y}{\partial \beta}\right)_{\substack{\text{TAIL ON} \\ \alpha_{f\,LOC} \\ \beta=0}} - \left(\frac{\partial Y}{\partial \beta}\right)_{\substack{\text{TAIL OFF} \\ \alpha_{f\,LOC} \\ \beta=0}}\right] \times \left(\frac{1}{S.F.}\right)^2 \left(\frac{q}{q_{TEST}}\right) \left(\frac{57.3}{\rho b C \Omega^2 R^3}\right)$

13. $F_{Y\beta_{WBT}} = \left(\frac{\partial Y}{\partial \beta}\right)_{\substack{\text{MODEL} \\ \alpha_{f\,LOC};\ \beta=0}} \times \left(\frac{1}{S.F.}\right)^2 \left(\frac{q}{q_{TEST}}\right) \left(\frac{57.3}{\rho b C \Omega^2 R^3}\right)$

14. $N_{\beta_{WBT}} = \left(\frac{\partial N}{\partial \beta}\right)_{\substack{\text{MODEL} \\ \alpha_{f\,LOC};\ \beta=0}} \times \left(\frac{1}{S.F.}\right)^3 \left(\frac{q}{q_{TEST}}\right) \times \frac{57.3}{\rho b C \Omega^2 R^4}$

15. $\frac{\partial \epsilon_w}{\partial \alpha_f} = 0$ (AVERAGE VALUE FOR HSS-1)

16. $\frac{\partial \sigma'}{\partial \beta} = 0$ (AVERAGE VALUE FOR HSS-1)

B.2.9 Parameters and Constants.

1. $\mu = V/\Omega R$

2. $\mu_{T.R.} = \mu_{M.R.} \frac{(\Omega R)}{(\Omega R)_{T.R.}} \times \sqrt{\frac{q_T}{q}}$

3. $[\sigma]_{\substack{M.R. \\ T.R.}} = \left[\frac{bc}{\pi R}\right]_{\substack{M.R. \\ T.R.}}$

4. $[\gamma]_{\substack{M.R. \\ T.R.}} = \left[\frac{\rho a_0 c R^4}{I_b}\right]_{\substack{M.R. \\ T.R.}}$

5. $[\zeta]_{M.R.} = \left[\frac{e M_b}{I_b} + \frac{e^2 W_b}{I_b q}\right]_{M.R.}$

6.–13. B_{1S}; θ_0; λ; α_f; α_s; $\left(\frac{p}{L}\right)_i$; $\left(\frac{p}{L}\right)_0$; $\left(\frac{p}{L}\right)$

CALCULATED BY THE METHOD OF REFERENCE 4.

14. $\frac{C_{\ell\beta}}{\sigma} = \mu\left(\frac{p}{L}\right)\left(\frac{C_x}{\sigma}\right)$

15. $\alpha' = 57.3\left[\left(\frac{p}{L}\right)_0 - \left(\frac{p}{L}\right) - \left(\frac{\lambda}{\mu}\right)\right]$

16. $\left(\frac{C_T}{\sigma}\right)_{\substack{\text{trim} \\ \theta=0}} = -\frac{\sigma a}{2}\left\{\theta_0\left[\frac{2}{3}\mu a_0 - \left(\frac{1}{3}+\frac{1}{2}\mu^2\right)b_1\right] + \theta\left[\frac{1}{2}\mu a_0 - \frac{1}{4}\mu(1+\mu^2)\right] + \frac{2}{3}\lambda(2\mu a_0 - b_1) + a_0\right.$

17. $\left(\frac{M'}{\sigma}C_{\ell_{trim}}\right)_{trim} = -\frac{\sigma a}{2R}\left\{-\frac{1}{6}a_0\left[1-\left(\frac{r_R}{R}\right)^3\right] + \frac{\theta_{0.75}}{2}\left[\lambda^2+\mu^2\right]\left[1-\left(\frac{r_R}{R}\right)^2\right]\right.$
$\left. + \frac{1}{2}\left[\lambda^2\alpha + \frac{1}{4}a_1\mu^2 + \lambda\mu\right]\left[1-\left(\frac{r_R}{R}\right)\right]\right\}$

18. $$\frac{C_{T_T}}{\sigma^*} = \frac{C_a}{\sigma \left(\frac{F.S._{TR} - F.S._{M.R.}}{12R}\right)}$$

19. $$A_{1S} = \frac{\frac{\gamma_a}{2\gamma} b_1 - \frac{\mu^2}{2\sigma} C_{1m} - \frac{C_Y}{\sigma}\left(\frac{h}{R}\right) - \frac{C_{T_T}}{\sigma^*}\left(\frac{h_{TR}}{R}\right)}{\frac{\gamma_a}{2\gamma} + \frac{C_T}{\sigma}\left(\frac{h}{R}\right)}$$

20. $$\phi = - \frac{\frac{C_T}{\sigma} A_{1S} + \frac{C_Y}{\sigma} + \frac{C_{T_T}}{\sigma^*}}{\omega}$$

21. $t_{1,1}$; $t_{1,2}$; $t_{i,j}$ etc.

22. $\frac{\partial t_{1,1}}{\partial \mu}$; $\frac{\partial t_{1,2}}{\partial \mu}$; $\frac{\partial t_{i,j}}{\partial \mu}$; etc.

23. a_0; a_1; b_1;

} OBTAINED FROM REFERENCE 1

24. $$C' = \frac{1 + \frac{1}{\frac{2\mu^2}{C_T}\left[1+\left(\frac{\alpha}{\beta\omega}\right)^2\right]^{\frac{1}{2}}} - 1}{\sqrt{1+\left(\frac{\alpha}{\beta\omega}\right)^2}}$$

25. $$b' = \frac{C_Y/\sigma}{C_T/\sigma}$$

26. $$\lambda_{T.R.} = -\left(\frac{C_{T_T}}{\sigma^*}\right)\left(\sigma_{M.R.}\right)\left(\frac{\Omega}{\Omega_{TR}}\right)^2\left(\frac{R}{R_{TR}}\right)\frac{4}{2\mu_{TR}}$$

27. $$\theta_{.75_{TR}} = \left[\frac{\frac{2}{a_{TR}}\left(\frac{C_{T_T}}{\sigma^*}\right)\left(\frac{\sigma_{M.R.}}{\sigma_{TR}}\right)\left(\frac{\Omega}{\Omega_{TR}}\right)^2\left(\frac{R}{R_{TR}}\right)^4 - (t_{3,1})_{T.R.}(\lambda)_{TR}}{(t_{3,2})_{TR}}\right]$$

28. $$(h_{V.T.})_{\alpha,\phi=0} = \frac{W.L._{V.T.} - W.L._{C.G.}}{12}$$

29. $h = \left(\frac{W.L._{MR} - W.L._{CG}}{12}\right)\cos\alpha_f + \left(\frac{F.S._{CG} - F.S._{MR}}{12}\right)\sin\alpha_f$

30. $\bar{h} = \left(\frac{F.S._{CG} - F.S._{MR}}{12}\right)\cos\alpha_f - \left(\frac{W.L._{MR} - W.L._{CG}}{12}\right)\sin\alpha_f$

31. $h_{TR} = \left(\frac{W.L._{TR} - W.L._{CG}}{12}\right)\cos\alpha_f - \left(\frac{F.S._{TR} - F.S._{CG}}{12}\right)\sin\alpha_f$

32. $l_{TR} = \left(\frac{FS_{TR} - FS_{CG}}{12}\right)\cos\alpha_f + \left(\frac{WL_{TR} - WL_{CG}}{12}\right)\sin\alpha_f$

33. $h_{VT} = \left(\frac{WL_{VT} - WL_{CG}}{12}\right)\cos\alpha_f - \left(\frac{F.S._{VT} - F.S._{CG}}{12}\right)\sin\alpha_f$

34. $l_{VT} = \left(\frac{F.S._{VT} - FS_{CG}}{12}\right)\cos\alpha_f + \left(\frac{W.L._{VT} - WL_{CG}}{12}\right)\sin\alpha_f$

35. $h_{HT} = \left(\frac{WL_{HT} - WL_{CG}}{12}\right)\cos\alpha_f - \left(\frac{FS_{HT} - F.S_{CG}}{12}\right)\sin\alpha_f$

36. $l_{H.T} = \left(\frac{F.S._{HT} - F.S_{CG}}{12}\right)\cos\alpha_f + \left(\frac{W.L_{HT} - WL_{CG}}{12}\right)\sin\alpha_f$

37. $h_s = \left(\frac{W.L._{MR} - W.L._{CG}}{12}\right)\cos i_s + \left(\frac{F.S._{CG} - F.S._{MR}}{12}\right)\sin i_s$

38. $\bar{h}_s = \left(\frac{F.S._{CG} - F.S._{M.R.}}{12}\right)\cos i_s - \left(\frac{W.L._{M.R.} - W.L._{CG}}{12}\right)\sin i_s$

39. EK_f = ratio of the downwash velocity at the helicopter center of gravity to the downwash velocity at the plane of the rotor.

40. EK_T = ratio of the downwash velocity at the horizontal tail to the downwash velocity at the plane of the rotor.

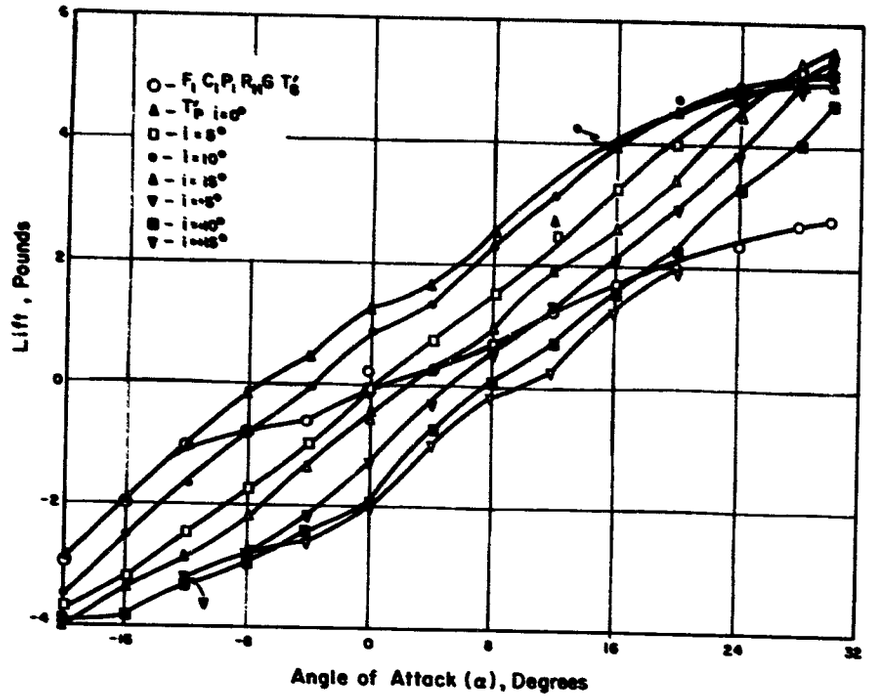

Figure B.7 Lift versus angle of attack.

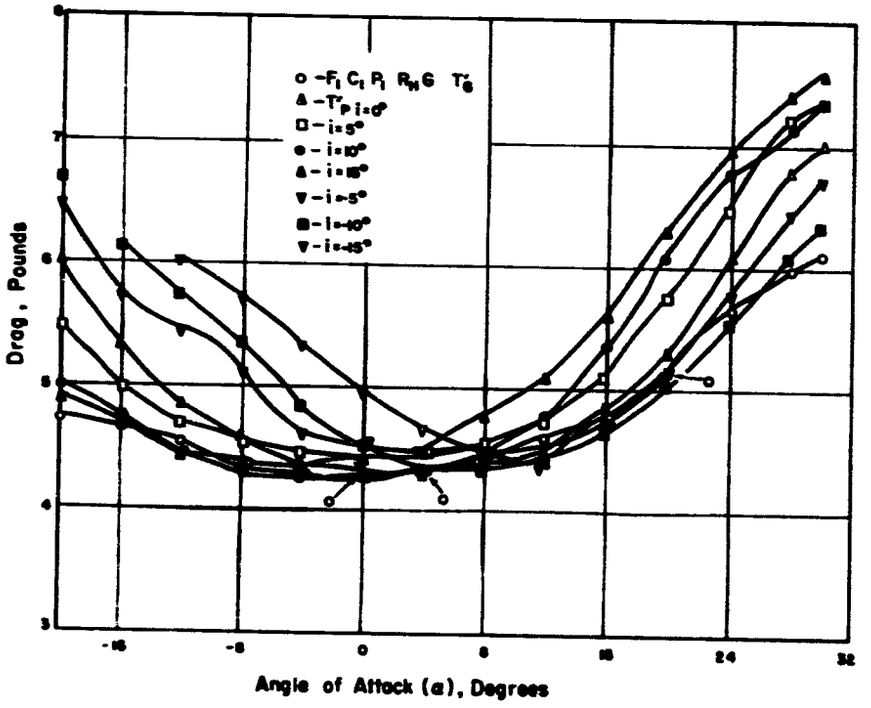

Figure B.8 Drag versus angle of attack.

B.3 DISCUSSION

In order to facilitate the calculation of helicopter aerodynamic parameters for a forward flight condition in which the helicopter was in static equilibrium, a program which satisfied the force and moment conditions represented by Equations 1 through 6 of Section B.2.6 was set up on an IBM 704 Electronic Data Processing Machine. The complete program incorporated a static trim program to calculate initial trim conditions and an algebraic dynamic stability derivative program in the digital computer part. Such helicopter design data as listed in Table B.1 and wind tunnel data from Figures B.7 through B.11 for fuselage lift, drag, pitching moment, yawing moment, and side force, respectively, constituted the input data. Table B.1 illustrates the numerical values for parameters required to calculate HSS-1 helicopter static trim and stability derivatives with the aid of the IBM 704. The stability derivatives were then taken to an EASE Analog Computer and set up in the equations of motion represented in Section B.2.5. The analog computer performed a rapid solution of the equations of motion and plotted the results in engineering units on six-channel graph paper as illustrated in Figure B.12. The effect of any arbitrary helicopter control input, gust, or angle-of-attack input could be studied.

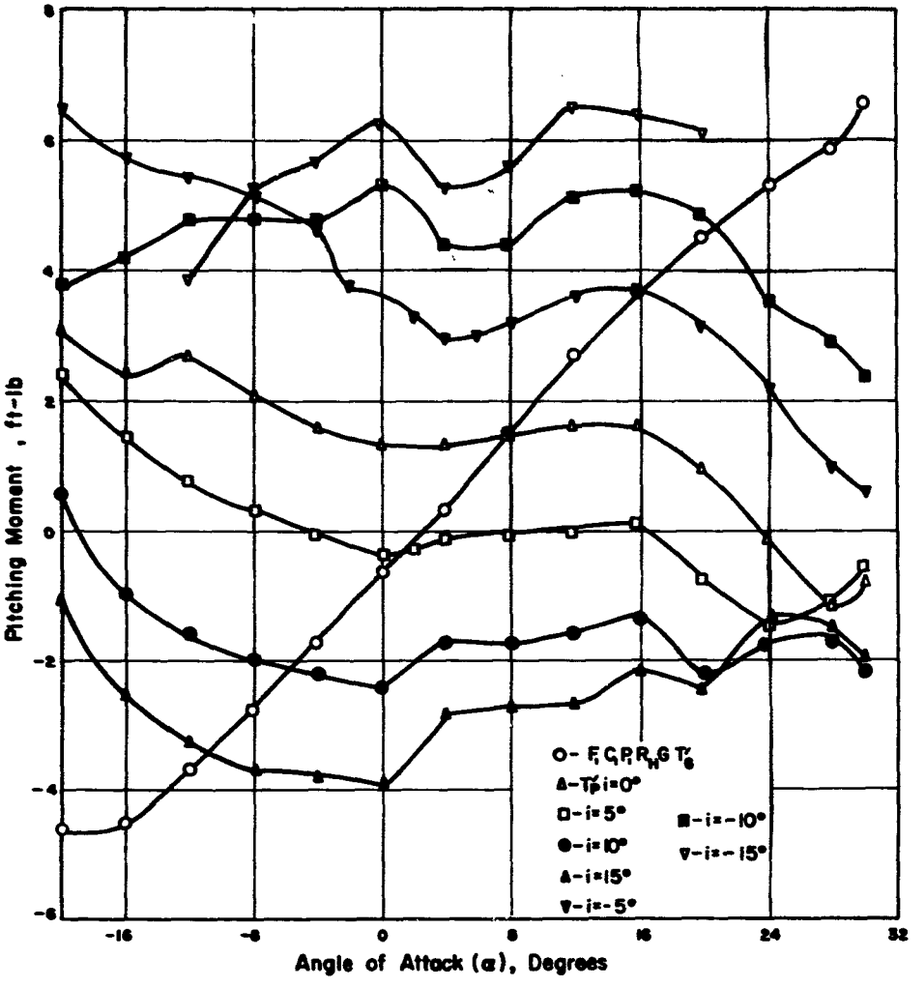

Figure B.9 Pitching moment versus angle of attack.

The results shown in Figure B.12 were obtained by solution of the Equations shown in Table B.2 with derivatives evaluated for the specific test event, Shot Priscilla. The incremental notation for derivatives in these equations has been discussed in Section

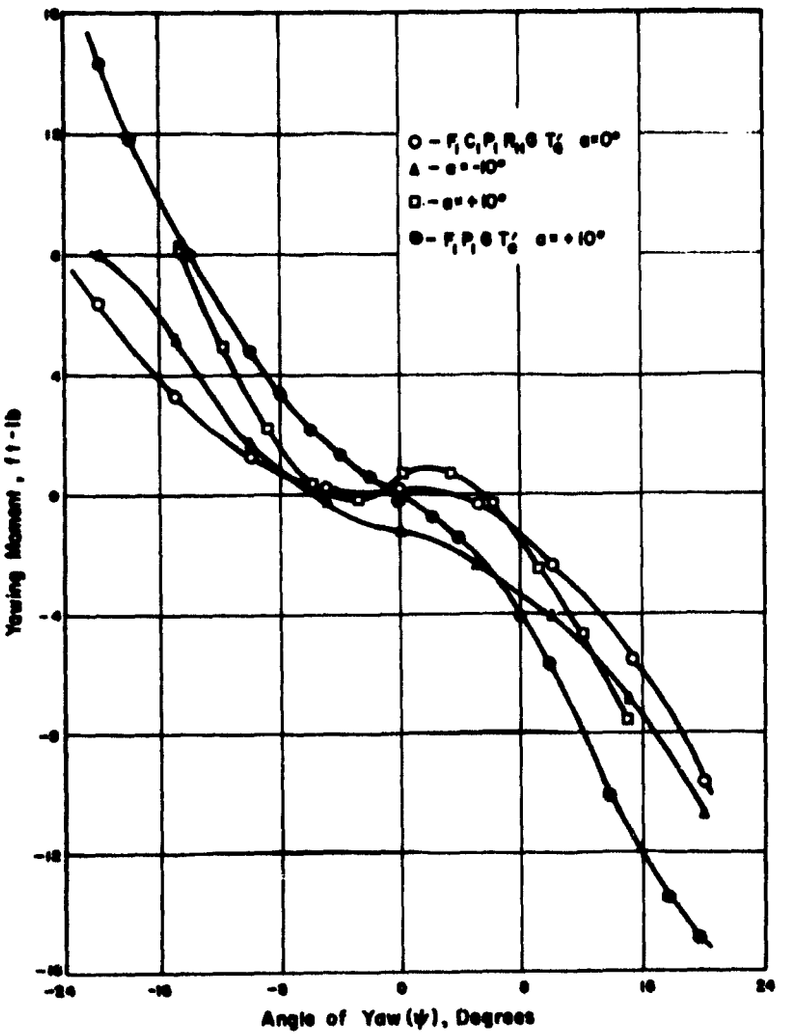

Figure B.10 Yawing moment versus angle of yaw.

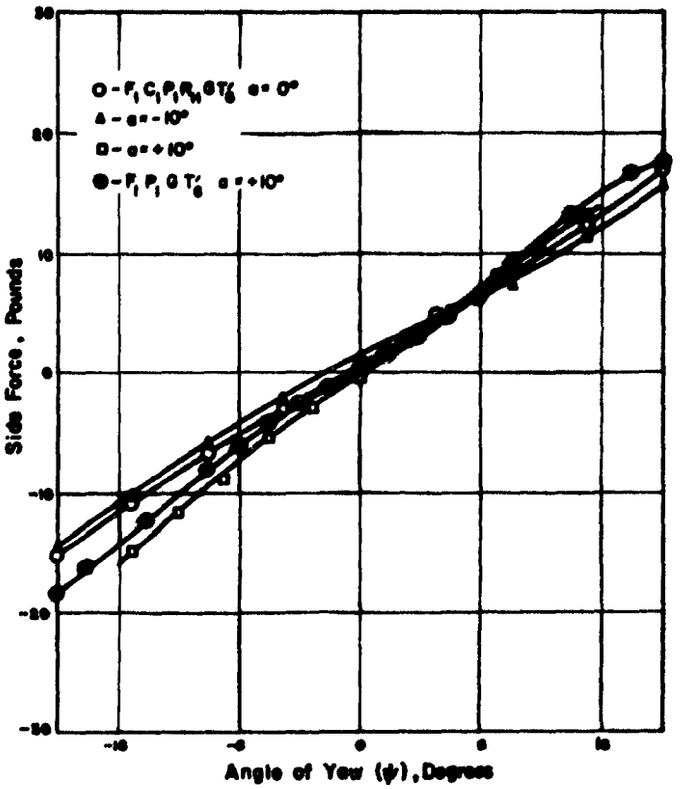

Figure B.11 Side force versus angle of yaw.

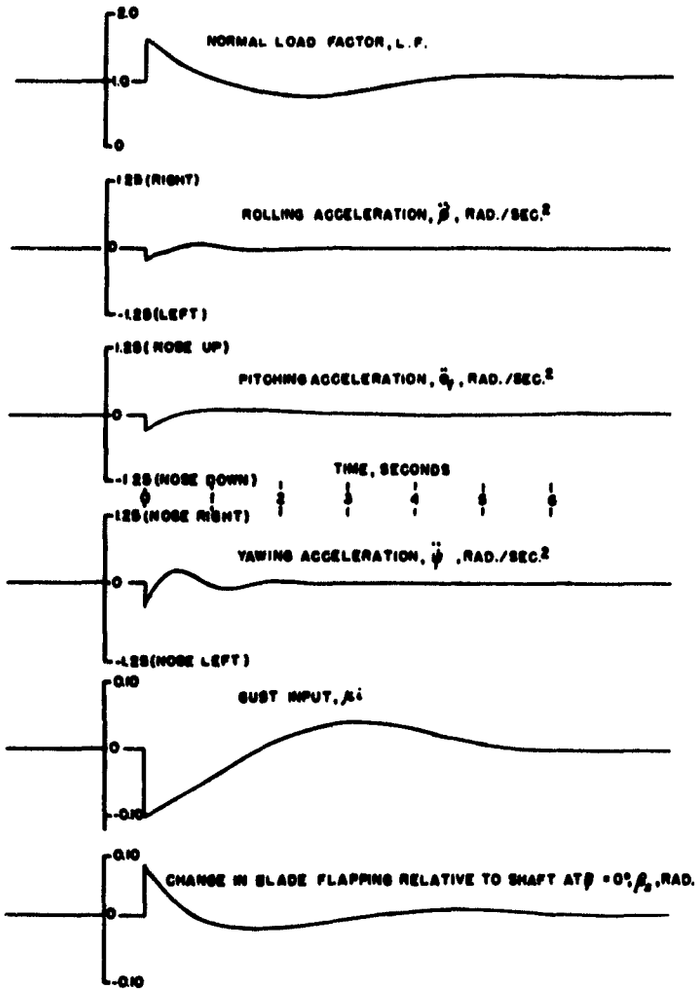

Figure B.12a Calculated response for Shot Priscilla.

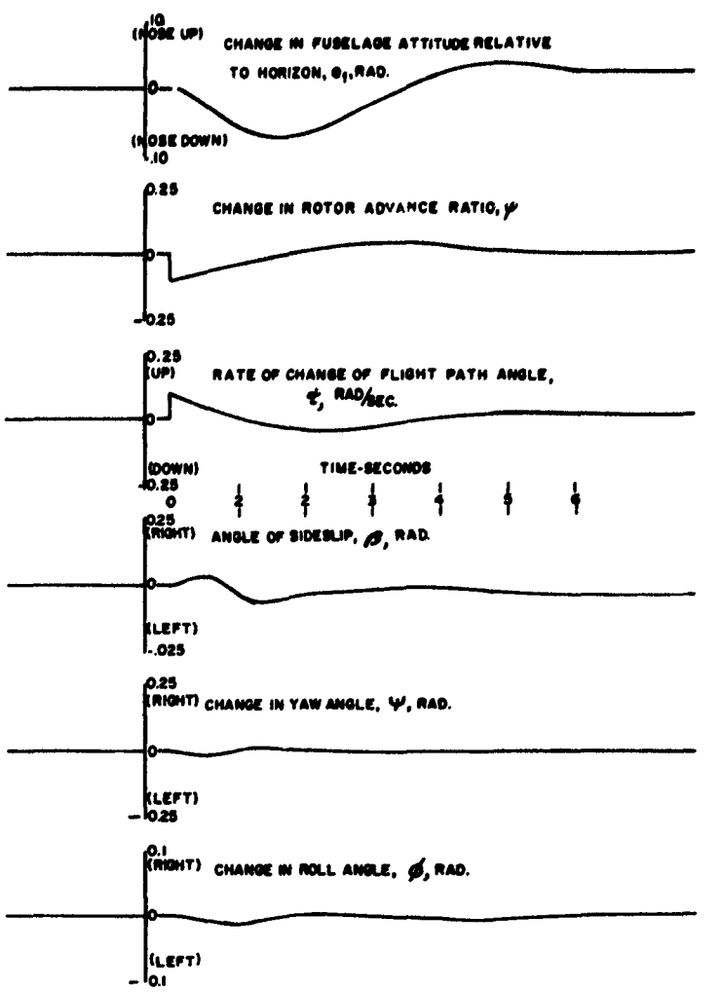

Figure B.12b Calculated response for Shot Priscilla.

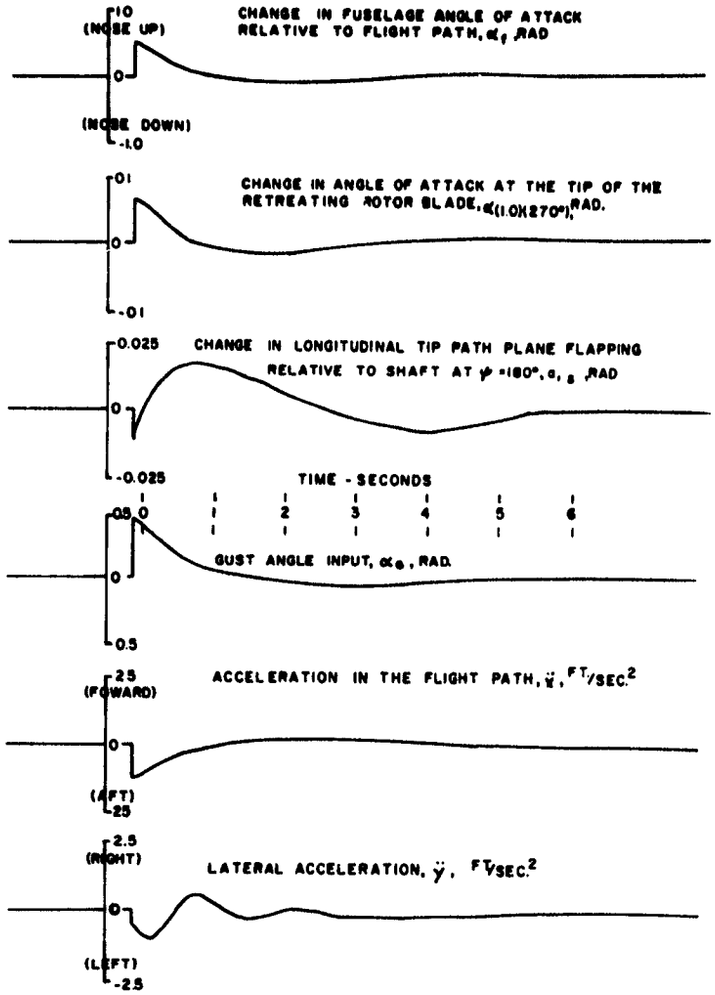

Figure B.12c Calculated response for Shot Priscilla.

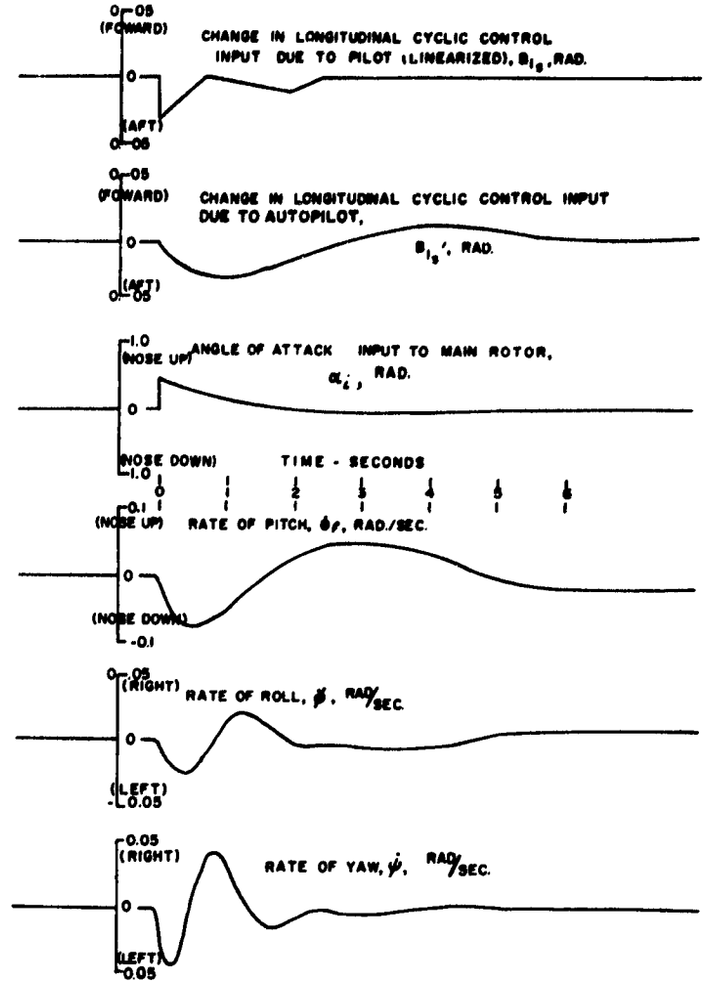

Figure B.12d Calculated response for Shot Priscilla.

TABLE B.1 HSS-1 HELICOPTER PARAMETERS FOR SHOT PRISCILLA

Density of air, ρ	0.001718 slug/ft^3	Fuselage station, tail rotor head, FS_{tr}	535 in
Main rotor rotation speed, Ω	24.82 rad/sec	Fuselage station, vertical tail center of pressure FS_{vt}	513 in
No. of main rotor blades, bmr	4	Fuselage station, center of gravity, FS_{cg}	146 in
Main rotor radius, R	28 ft	No. of tail rotor blades, b_{tr}	4
Main rotor blade chord, C_m	1.367 ft	Tail rotor radius, R_{tr}	4.67 ft
Main rotor blade aerodynamic twist, θ_1	−8 deg	Tail rotor blade chord, C_{tr}	0.612 ft
Main rotor blade weight, W_b	160.4 lbs	Tail rotor rotation speed, Ω TR,	149.3 rad/sec
Main rotor blade first mass moment about flapping hinge, M_b	63 slug-ft^2	Tail rotor blade aerodynamic twist, Θ_{tr}	0 deg
Main rotor blade second mass moment about flapping hinge, I_b	1,144.5 slug-ft^2	Tail rotor blade moment of inertia about flapping hinge I_{btr}	0.8 slug-ft^2
Main rotor blade lift slope, $a_{m.r.}$,	5.73/Radian	Tail rotor blade lift slope, a_{tr}	5.73/radian
Main rotor blade flapping hinge offset, e,	1 ft	Rotor blade tip loss factor, B	0.97
Helicopter gross weight, G.W.	10,700 lbs	Main rotor shaft tilt, i_s	+3 deg (forward)
Helicopter moment of inertia about pitch axis, I_y	25,485 slug-ft^2	Horizontal tail incidence, i_t	0
Helicopter moment of inertia about roll axis, I_x	5,190 slug-ft^2	Horizontal tail area, S_t	12.4 ft^2
Helicopter moment of inertia about yaw axis, I_z	21,587 slug-ft^2	Rotor blade profile drag coefficients	
Waterline wind tunnel data force resolution point WL_{mp}	21.6	$(C_{do} = \delta_0 + \delta_1 \alpha\, r + \delta_2 \alpha\, r^2)$ δ_0	0.0087
Waterline, main rotor head, WL_{mr}	128.4	δ_1	−0.0216
Waterline, horizontal tail center of pressure WL_{ht}	59.0	δ_2	1.00
Waterline, tail rotor head, WL_{tr}	107.2	Parasite area correction to wind tunnel measured values	21.29 ft^2
Waterline vertical tail center of pressure, WL_{vt}	60.5	Wind tunnel model scale	1/10
Waterline, center of gravity, WL_{cg}	36 in.	Wind tunnel test dynamic pressure, Q_{test}	25.6 lbs/ft^2
Fuselage station, wind tunnel data force resolution point, FS_{mp}	137.5 in.	Rotor downwash correction at fuselage, EK_{fus},	0.5
Fuselage station, main rotor head, FS_{mr}	137.7 in	Rotor downwash correction at horizontal tail, EK_{tail}	1.8
Fuselage station, horizontal tail center of pressure, FS_{ht}	477.2 in		

TABLE B.2 EQUATIONS OF MOTION FOR SHOT PRISCILLA

1 $.00600\dot{\tau} - .08374\tau + .006900\dot{\alpha}_f - .07991\alpha_f - .003249\phi - 1.813\dot{\mu} - .06699\mu + .080638_{1s} + .002260\theta_o = 0$

2 $-.006615\dot{\tau} - .006615\dot{\alpha}_f - .00369\alpha_f - .3911\dot{\beta} - .03379\beta - .007319 + .08374\phi - .2894\psi + .012587\mu + .08432 A_{1s} + .00369 B_{1s} - .00587\theta_o + .038160_t = 0$

3. $.3911\dot{\tau} + .0006368\dot{\alpha}_f + (-.1789 + \Delta F_{2\alpha_f})\alpha_f - .00706\dot{\phi} + (-.05261 + \Delta F_{2\mu})\mu + .1752 B_{1s} - .7305\theta_o = 0$

4. $-.004482\dot{\tau} - .004482\dot{\alpha}_f + (-.000345 + \Delta L_{\alpha_f})\alpha_f - .005364\beta - .001455\dot{\phi} - .004879\phi + .0005361\psi + .004870\mu + .04680 A_{1s} + .000345 B_{1s} + .0012842\theta_o + .00638\theta_t = 0$

5. $-.007144\ddot{\tau} + .000072\dot{\tau} - .007144\ddot{\alpha}_f - .005754\dot{\alpha}_f + (.002319 + \Delta M_{\alpha_f})\alpha_f + .0003802\beta + .001988\dot{\phi} + .02205\mu - .04935 B_{1s} + .01936\theta_o = 0$

6. $-.000093\ddot{\tau} - .000093\ddot{\alpha}_f - .00382\alpha_f + .01018\beta + .0004254\dot{\phi} - .006051\ddot{\psi} - .005569\dot{\psi} - .016688\mu + .0011893 A_{1s} + .00382 B_{1s} + .04101\theta_o - .04446\theta_t = 0$

$$L.F. = 1 - 11.8597 \frac{(-.1789 + \Delta F_{2\alpha_f})}{\cos^2 \alpha_i} \alpha_f$$

1. $A'_{1s} = -.1200\dot{\phi} - .1200\phi$
2. $B'_{1s} = .2040(\dot{\alpha}_f + \dot{\tau}) + .2700(\alpha_f + \tau)$
3. $\theta'_t = .2925\dot{\psi} + .2500\psi$

NOTE: α_i AND μ_i ARE TREATED AS α_f AND μ INPUTS RESPECTIVELY

$$\alpha_{(4.0)(270°)} = .1253 + \theta_o + 1.195\left[-.10219(\dot{\alpha}_f + \dot{\tau}) + (.12874 - .0447)\alpha_f + (-.0038 + .3301)\mu - (.1287 + .0447)B_{1s}\right]$$

$$\beta_{3(90°)} = .100 + .1417\alpha_f + .03587\mu - .1417 B_{1s} + .669\theta_o - \left[-.10219(\dot{\alpha}_f + \dot{\tau}) + .0447\alpha_f + .3301\mu + .4047\theta_o\right] + (1 + .0447)B_{1s}$$

CONFIDENTIAL

2.3.2. The calculations were performed for six seconds so that sufficient time is allowed to determine what flying qualities and loads occur for the full duration of the blast. Time histories of all three translating accelerations as well as rolling, pitching, and yawing accelerations for the purpose of loads calculated are shown in Figure B.12. In addition, time histories are shown of fuselage attitude, roll, pitch, and yaw rates, angle of attack at the tip of the retreating rotor blade and rotor-blade flapping angle relative to the shaft when the blade is over the tail cone. For these last two parameters, equations presented in Section 2.4.2 were evaluated and serve to indicate development of stall in the rotor and rotor blade clearance over the tail cone, respectively.

Appendix C
TYPICAL TIME HISTORIES

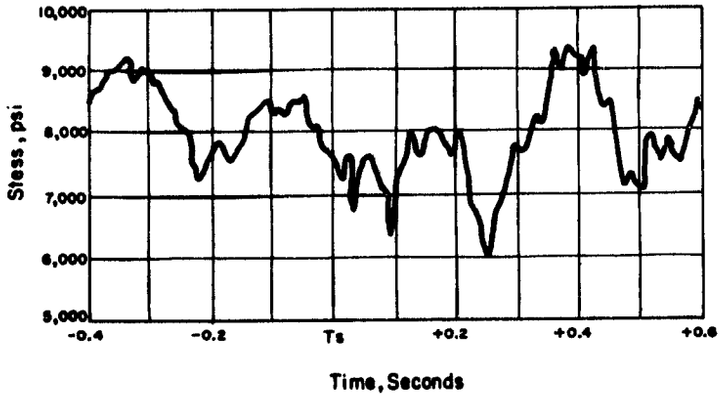

Figure C.1 Main rotor blade edgewise stress versus time.

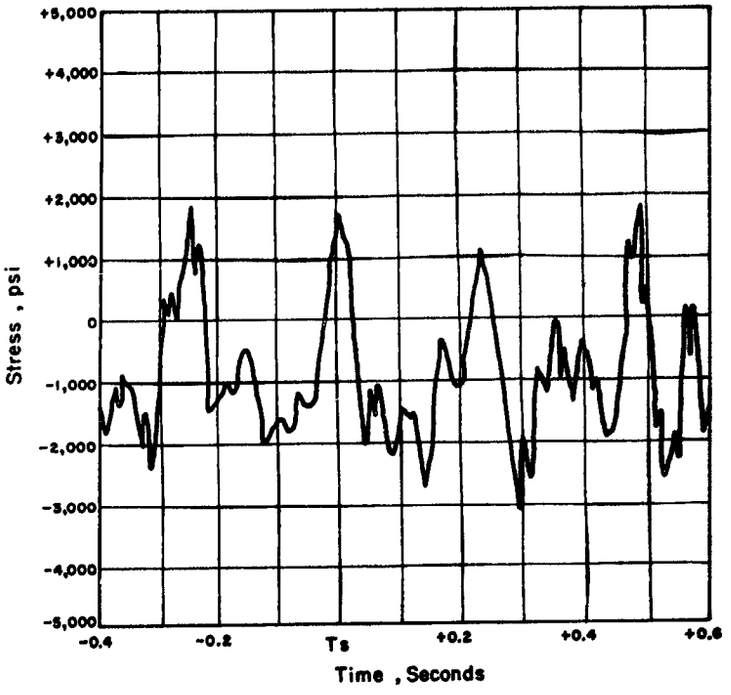

Figure C.2 Main rotor blade flatwise stress versus time.

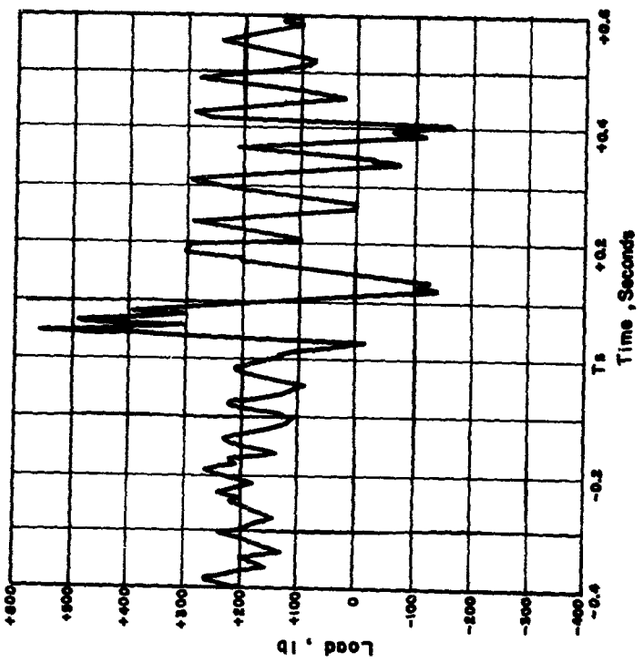

Figure C.4 Right lateral star load versus time.

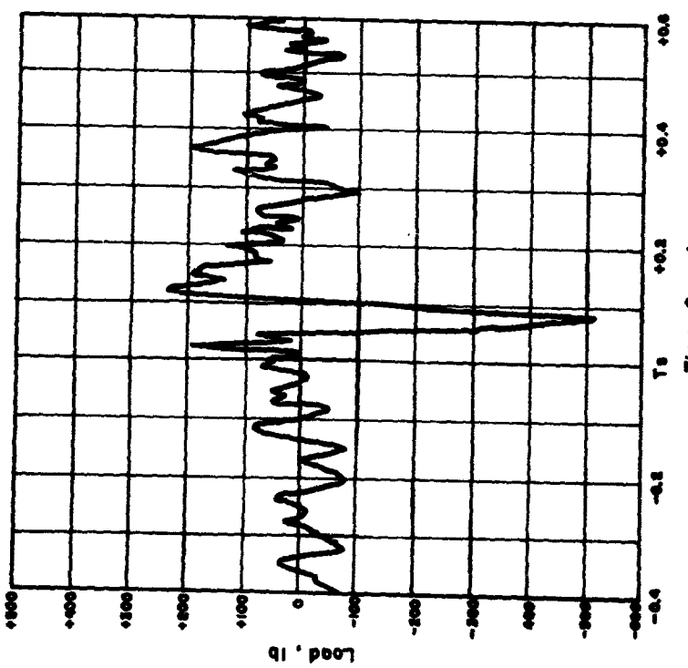

Figure C.3 Longitudinal star load versus time.

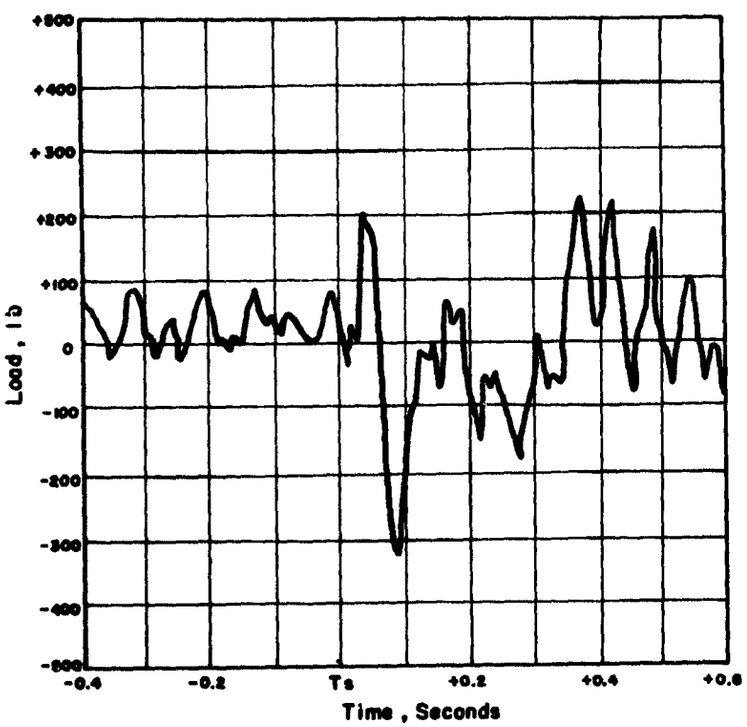

Figure C.5 Left lateral star load versus time.

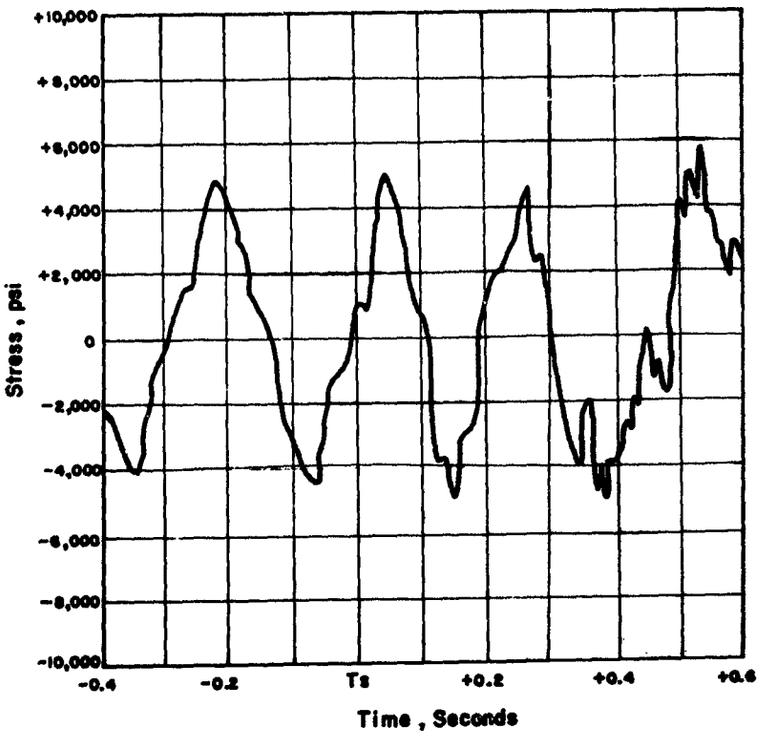

Figure C.6 Main rotor shaft bending stress versus time.

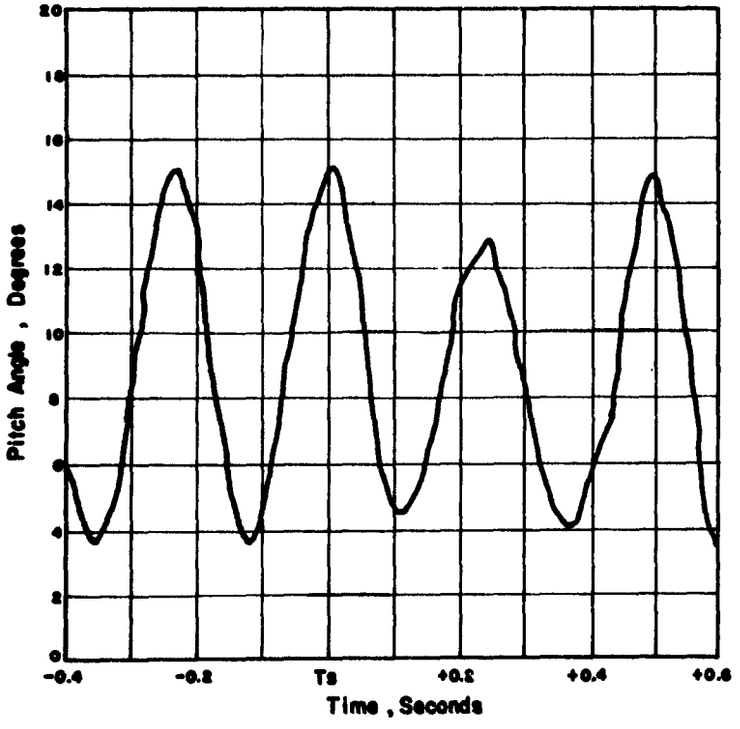

Figure C.7 Main rotor blade pitch angle versus time.

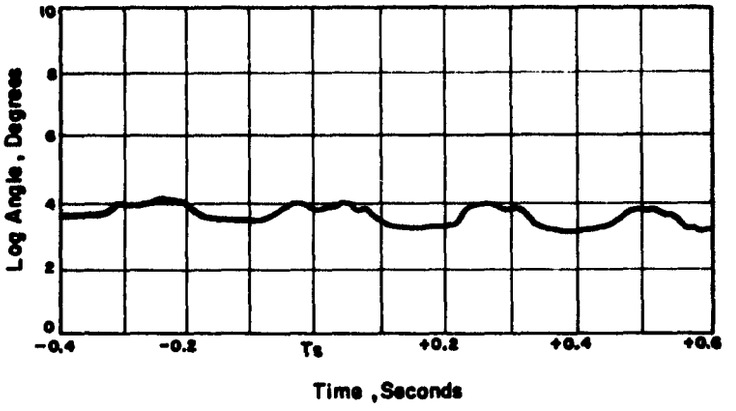

Figure C.8 Main rotor blade lag angle versus time.

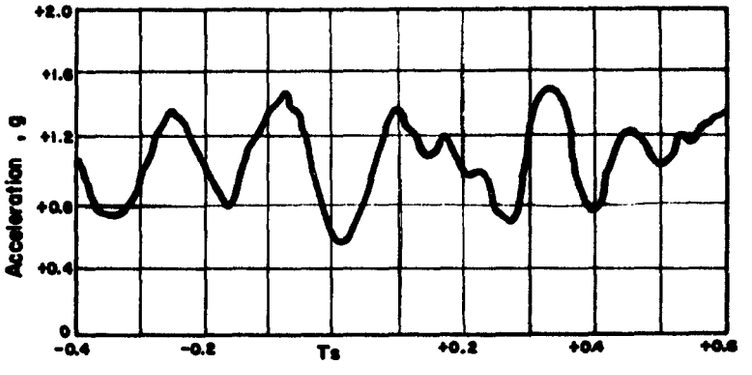

Figure C.9 Vertical acceleration at tail pylon versus time.

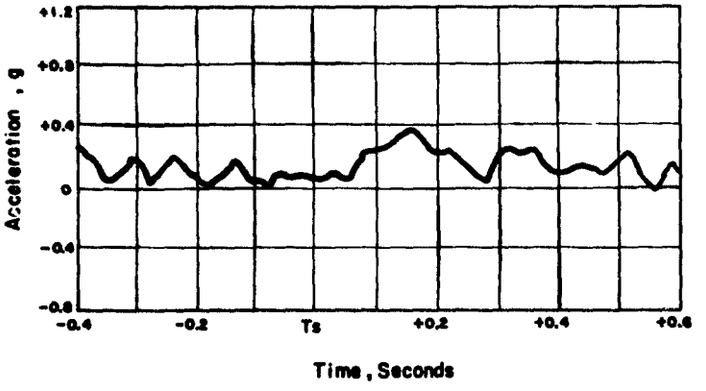

Figure C.10 Lateral acceleration at tail pylon versus time.

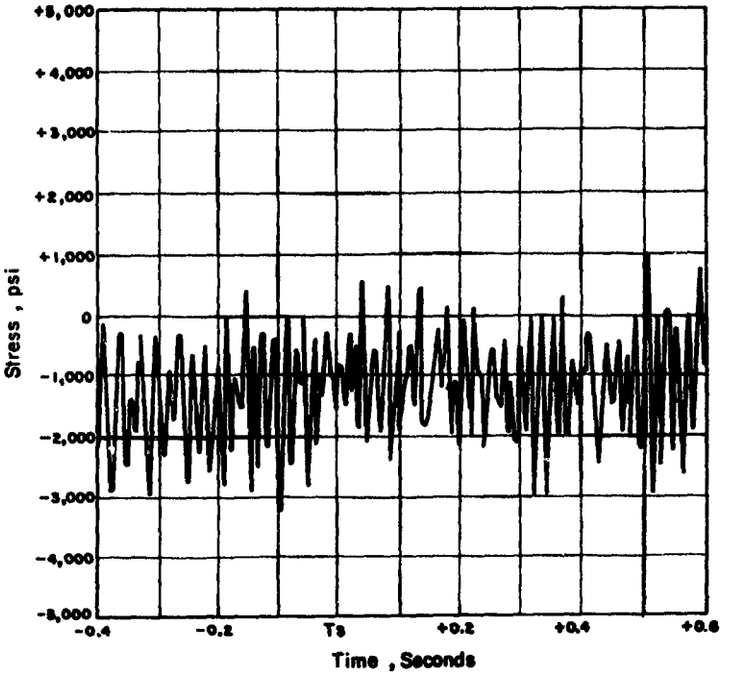

Figure C.11 Tail rotor blade edgewise stress versus time.

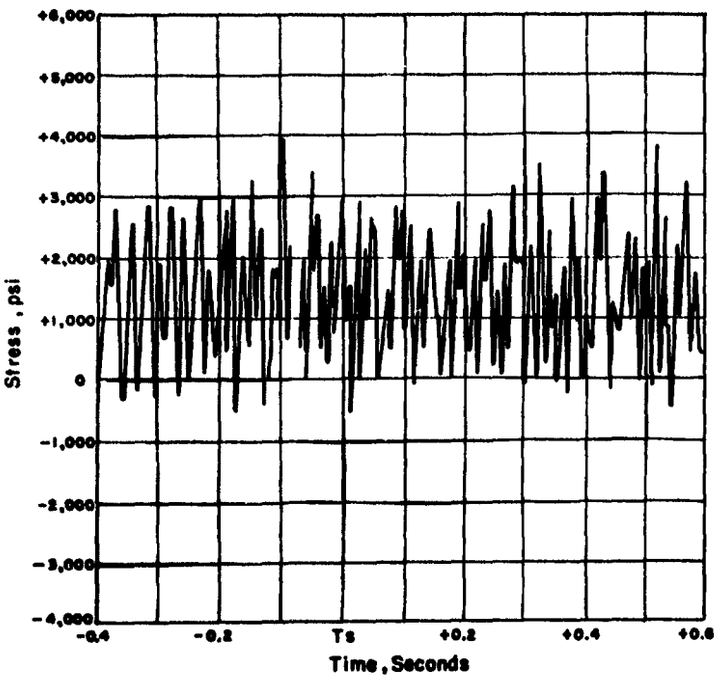

Figure C.12 Tail rotor blade flatwise stress versus time.

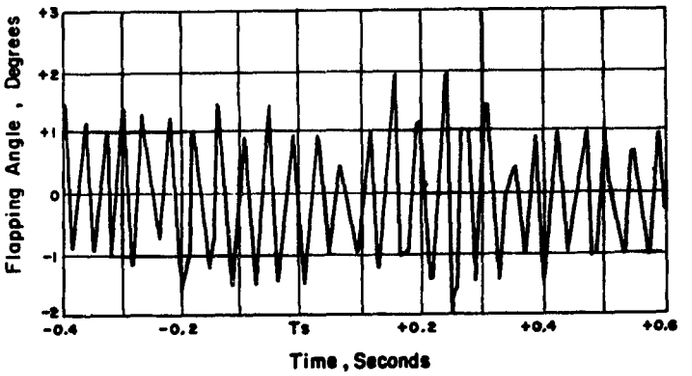

Figure C.13 Tail rotor blade flapping angle versus time.

REFERENCES

1. "A Simplified Theoretical Method of Determining the Characteristics of a Lifting Rotor in Forward Flight"; NACA TR716, 1941; Unclassified.

2. "Charts for Estimation of Longitudinal Stability Derivatives for a Helicopter Rotor in Forward Flight"; NACA TN2309, March 1951; Unclassified.

3. "Capabilities of Atomic Weapons"; TM 23-200, Revised Edition November 1957; Armed Forces Special Weapons Project, Washington, D. C.; Confidential.

4. "Analysis of the Static Longitudinal Trim Characteristics of the HSS-1 Helicopter"; Sikorsky Aircraft, August 1953; Unclassified.

DISTRIBUTION

Military Distribution Categories 52 and 54

ARMY ACTIVITIES

1 Deputy Chief of Staff for Military Operations, D/A, Washington 25, D.C. ATTN: Dir. of SW&R
2 Chief of Research and Development, D/A, Washington 25, D.C. ATTN: Atomic Div.
3 Assistant Chief of Staff, Intelligence, D/A, Washington 25, D.C.
4 Chief of Engineers, D/A, Washington 25, D.C. ATTN: ENGTB
5- 6 Office, Chief of Ordnance, D/A, Washington 25, D.C. ATTN: ORDTN
7 Chief of Transportation, D/A, Office of Planning and Int., Washington 25, D.C.
8- 10 Commanding General, U.S. Continental Army Command, Ft. Monroe, Va.
11 Director of Special Weapons Development Office, Headquarters CONARC, Ft. Bliss, Tex. ATTN: Capt. Chester I. Peterson
12 President, U.S. Army Artillery Board, Ft. Sill, Okla.
13 President, U.S. Army Air Defense Board, Ft. Bliss, Tex.
14 President, U.S. Army Aviation Board, Ft. Rucker, Ala. ATTN: ATBG-DG
15 Commandant, U.S. Army Command & General Staff College, Ft. Leavenworth, Kansas. ATTN: ARCHIVES
16 Commandant, U.S. Army Air Defense School, Ft. Bliss, Tex. ATTN: Command & Staff Dept.
17 Commandant, U.S. Army Artillery and Missile School, Ft. Sill, Okla. ATTN: Combat Development Department
18 Commandant, U.S. Army Aviation School, Ft. Rucker, Ala.
19 Commandant, U.S. Army Ordnance School, Aberdeen Proving Ground, Md.
20 Commandant, U.S. Army Ordnance and Guided Missile School, Redstone Arsenal, Ala.
21 Commanding General, U.S. Army Chemical Corps, Research and Development Comd., Washington 25, D.C.
22- 23 Commanding Officer, Chemical Warfare Lab., Army Chemical Center, Md. ATTN: Tech. Library
24 Commanding Officer, Diamond Ord. Fuze Labs., Washington 25, D.C. ATTN: Chief, Nuclear Vulnerability Br. (230)
25- 26 Commanding General, Aberdeen Proving Grounds, Md. ATTN: Director, Ballistics Research Laboratory
27- 28 Commanding General, U.S. Army Ord. Missile Command, Redstone Arsenal, Ala.
29 Commander, Army Rocket and Guided Missile Agency, Redstone Arsenal, Ala. ATTN: Tech Library
30 Commanding General, White Sands Proving Ground, Las Cruces, N. Mex. ATTN: ORDBS-OM
31 Commander, Army Ballistic Missile Agency, Redstone Arsenal, Ala. ATTN: ORDAB-HT
32 Commanding General, Ordnance Ammunition Command, Joliet, Ill.
33 Commanding General, USA Combat Surveillance Agency, 1124 N. Highland St., Arlington, Va.
34 Commanding Officer, USA Transportation Research Command, Ft. Eustis, Va. ATTN: Chief, Tech. Info. Div.
35 Commanding Officer, USA Transportation Combat Development Group, Ft. Eustis, Va.
36 Director, Operations Research Office, Johns Hopkins University, 6935 Arlington Rd., Bethesda 14, Md.
37 Commander-in-Chief, U.S. Army Europe, APO 403, New York, N.Y. ATTN: Opot. Div., Weapons Br.

NAVY ACTIVITIES

38 Chief of Naval Operations, D/N, Washington 25, D.C. ATTN: OP-03EG
39 Chief of Naval Operations, D/N, Washington 25, D.C. ATTN: OP-75
40 Chief of Naval Operations, D/N, Washington 25, D.C. ATTN: OP-922G1
41- 42 Chief of Naval Research, D/N, Washington 25, D.C. ATTN: Code 811
43- 44 Chief, Bureau of Aeronautics, D/N, Washington 25, D.C.
45- 49 Chief, Bureau of Aeronautics, D/N, Washington 25, D.C. ATTN: AER-AD-41/20
50- 51 Chief, Bureau of Ordnance, D/N, Washington 25, D.C.
52 Chief, Bureau of Ordnance, D/N, Washington 25, D.C. ATTN: S.P.
53 Director, U.S. Naval Research Laboratory, Washington 25, D.C. ATTN: Mrs. Katherine H. Cass
54- 55 Commander, U.S. Naval Ordnance Laboratory, White Oak, Silver Spring 19, Md.
56 Director, Material Lab. (Code 900), New York Naval Shipyard, Brooklyn 1, N.Y.
57 Commanding Officer, U.S. Naval Mine Defense Lab., Panama City, Fla.
58- 59 Commanding Officer, U.S. Naval Radiological Defense Laboratory, San Francisco, Calif. ATTN: Tech. Info. Div.
60 Commanding Officer, U.S. Naval Schools Command, U.S. Naval Station, Treasure Island, San Francisco, Calif.
61 Superintendent, U.S. Naval Postgraduate School, Monterey, Calif.
62 Commanding Officer, Nuclear Weapons Training Center, Atlantic, U.S. Naval Base, Norfolk 11, Va. ATTN: Nuclear Warfare Dept.
63 Commanding Officer, Nuclear Weapons Training Center, Pacific, Naval Station, San Diego, Calif.
64 Commanding Officer, U.S. Naval Damage Control Tng. Center, Naval Base, Philadelphia 12, Pa. ATTN: ABC Defense Course
65 Commanding Officer, Air Development Squadron 5, VX-5, China Lake, Calif.
66 Commanding Officer, Naval Air Material Center, U.S. Naval Base, Philadelphia 12, Pa. ATTN: Technical Data Br.
67 Commander, Officer U.S. Naval Air Development Center, Johnsville, Pa. ATTN: NAS, Librarian
68 Commanding Officer, Naval Air Sp. Wpns. Facility, Kirtland AFB, Albuquerque, N. Mex.
69 Commander, U.S. Naval Ordnance Test Station, China Lake, Calif.
70 Commandant, U.S. Marine Corps, Washington 25, D.C. ATTN: Code AO3H
71 Director, Marine Corps Landing Force, Development Center, MCS, Quantico, Va.
72 Commanding Officer, U.S. Naval CIC School, U.S. Naval Air Station, Glynco, Brunswick, Ga.
73- 81 Chief, Bureau of Naval Weapons, Navy Department, Washington 25, D.C. ATTN: RR12

AIR FORCE ACTIVITIES

82 Assistant for Atomic Energy, HQ, USAF, Washington 25, D.C. ATTN: DCS/O
83 Hq. USAF, ATTN: Operations Analysis Office, Office, Vice Chief of Staff, Washington 25, D. C.
84- 85 Air Force Intelligence Center, HQ. USAF, ACS/I (AFCIN-3V1) Washington 25, D.C.
86 Director of Research and Development, DCS/D, HQ. USAF, Washington 25, D.C. ATTN: Guidance and Weapons Div.
87 The Surgeon General, HQ. USAF, Washington 25, D.C. ATTN: Bio.-Def. Pre. Med. Division
88 Commander, Tactical Air Command, Langley AFB, Va. ATTN: Doc. Security Branch
89 Commander, Air Defense Command, Ent AFB, Colorado. ATTN: Assistant for Atomic Energy, ADLDC-A

90 Commander, Hq. Air Research and Development Command, Andrews AFB, Washington 25, D.C. ATTN: RDRWA
91 Commander, Air Force Ballistic Missile Div. HQ. ARDC, Air Force Unit Post Office, Los Angeles 45, Calif. ATTN: WDSOT
92- 93 Commander, AF Cambridge Research Center, L. G. Hanscom Field, Bedford, Mass. ATTN: CRQST-2
94- 98 Commander, Air Force Special Weapons Center, Kirtland AFB, Albuquerque, N. Mex. ATTN: Tech. Info. & Intel. Div.
99-100 Director, Air University Library, Maxwell AFB, Ala.
101 Commander, Lowry Technical Training Center (TW), Lowry AFB, Denver, Colorado.
102 Commandant, School of Aviation Medicine, Brooks Air Force Base, Texas
103 Commander, 1009th Sp. Wpns. Squadron, HQ. USAF, Washington 25, D.C.
104-106 Commander, Wright Air Development Center, Wright-Patterson AFB, Dayton, Ohio. ATTN: WCACT (For WCOSI)
107-108 Director, USAF Project RAND, VIA: USAF Liaison Office, The RAND Corp., 1700 Main St., Santa Monica, Calif.
109 Commander, Air Defense Systems Integration Div., L. G. Hanscom Field, Bedford, Mass. ATTN: SIDE-S
110 Chief, Ballistic Missile Early Warning Project Office, 220 Church St., New York 13, N.Y. ATTN: Col. Leo V. Skinner, USAF
111 Commander, Air Technical Intelligence Center, USAF, Wright-Patterson AFB, Ohio. ATTN: AFCIN-4Bla, Library
112 Headquarters, 1st Missile Div., USAF, Vandenburg AFB, Calif ATTN: Operations Analysis Office
113 Assistant Chief of Staff, Intelligence, HQ. USAFE, APO 633. New York, N.Y. ATTN: Directorate of Air Targets
114 Commander-in-Chief, Pacific Air Forces, APO 953, San Francisco, Calif. ATTN: PFCIE-MB, Base Recovery

OTHER DEPARTMENT OF DEFENSE ACTIVITIES

115 Director of Defense Research and Engineering, Washington 25, D.C. ATTN: Tech. Library
116 Chairman, Armed Services Explosives Safety Board, DOD, Building T-7, Gravelly Point, Washington 25, D.C.
117 Director, Weapons Systems Evaluation Group, Room 1E880, The Pentagon, Washington 25, D.C.
118-121 Chief, Defense Atomic Support Agency, Washington 25, D.C. ATTN: Document Library
122 Commander, Field Command, DASA, Sandia Base, Albuquerque, N. Mex.
123 Commander, Field Command, DASA, Sandia Base, Albuquerque, N. Mex. ATTN: FCTG
124-128 Commander, Field Command, DASA, Sandia Base, Albuquerque, N. Mex. ATTN: FCWT
129 Administrator, National Aeronautics and Space Administration, 1520 "H" St., N.W., Washington 25, D.C. ATTN: Mr. R. V. Rhode
130 Commander-in-Chief, Strategic Air Command, Offutt AFB, Neb. ATTN: OAMS
131 U.S. Documents Officer, Office of the United States National Military Representative - SHAPE, APO 55, New York, N.Y.

ATOMIC ENERGY COMMISSION ACTIVITIES

132-134 U.S. Atomic Energy Commission, Technical Library, Washington 25, D.C. ATTN: For DMA
135-136 Los Alamos Scientific Laboratory, Report Library, P.O. Box 1663, Los Alamos, N. Mex. ATTN: Helen Redman
137-141 Sandia Corporation, Classified Document Division, Sandia Base, Albuquerque, N. Mex. ATTN: H. J. Smyth, Jr.
142 University of California Lawrence Radiation Laboratory, P.O. Box 808, Livermore, Calif. ATTN: Clovis G. Craig
143 Weapon Data Section, Technical Information Service Extension, Oak Ridge, Tenn.
144-175 Technical Information Service Extension, Oak Ridge, Tenn. (Surplus)